Methodologies for low excess noise measurement in wide bandgap materials

Liang Qiao

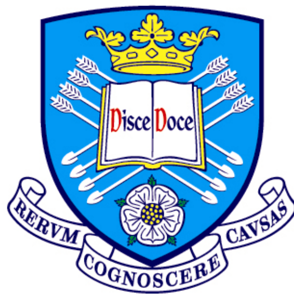

A thesis submitted for the degree of Doctor of Philosophy
Department of Electronic and Electrical Engineering
The University of Sheffield

December 2017

Acknowledgements

I would like to express my deepest gratitude to my supervisor Dr. James Green and Prof. John David for giving me the opportunity to pursue my PhD in UK and for providing me the invaluable guidance during my PhD study. I really appreciate for their constant support, particularly in the beginning of my research. I am also grateful to Prof. Chee Hing Tan and Prof. Jo Shien Ng for their suggestions on my work.

Special thanks go to Dr. Simon Dimler who offered me their expertise and valuable suggestions on circuit design and test. I would like to thank Dr. Jeng Shiuh Cheong for his patience in showing the experiment setup and procedures during the first year of my PhD.

I also wish to thank my colleagues in the group, past and presents, Dr. Ian Sandall, Dr. Shiyu Xie, Dr. Xinxin Zhou, Dr. Xiao Meng, Dr. Akeel Auckloo, Dr. Benjamin White, Aina Baharuddin, Zhize Zhou, Faezah Harun and Xin Yi.

Finally, I am especially grateful to my parents and my wife for their constant support and encouragement throughout my PhD studies.

Abstract

This work aims at investigating the avalanche excess noise characteristics of the $Al_xGa_{1-x}InP$ (x from 0 to 1) avalanche photodiode (APDs) for practical applications such as underwater detection, oil well logging and space exploration. Normally, Si APDs are used to operate in the visible part of the spectrum, however this has a broad spectral response and requires optical band-pass filters to avoid the detection of extraneous light sources at other wavelengths, which adds cost and complexity to the system.

To enable these measurements to be undertaken, a high sensitivity system for measuring multiplication and the excess noise is described. The system is capable of measuring the multiplication and excess noise power of devices, even when the photocurrent is low (approximately 10 nA). The signal to noise ratio (SNR) of the system is more than two orders of magnitude better than previously reported systems. The ability to characterise APD performance with such low photocurrents enables the use of low power light sources such as light emitting diode (LED) rather than lasers to investigate their noise performance.

Multiplication and avalanche excess noise measurements have been undertaken on a series of AlInP homo-junction PIN and NIP diodes with *i* region widths ranging from 0.04 µm to 1 µm, using 442 nm (laser) and 460 nm (LED) wavelength light. Low dark currents of < 170 nA cm^{-2} at 95% of breakdown voltage were obtained in all the devices because of its wide bandgap and there was no tunneling dark current present even at high-fields > 1000 kV/cm. For a given multiplication factor, the excess noise decreased as the avalanche width decreased due to the 'dead-space' effect. Avalanche excess noise measurements were also performed on a separate absorption multiplication avalanche photodiode (SAM-APD) with a nominal multiplication region width of 0.2 µm at 460 nm wavelength and it had an effective k (hole to electron ionization coefficient ratio) of approximately 0.3.

There is also a requirement for photodetectors capable of high temperature operation. A high temperature measurement system is described. The system can measure temperature dependence of the noise characteristics in AlInP devices. AlInP devices are found to be suitable for operating in high temperature environments. Avalanche multiplication and excess noise from 298 K to 475 K have been measured on AlInP diodes under 460 nm LED illumination. These devices have *i* region widths ranging from 0.04 µm to 1 µm. The impact ionization

coefficients have been extracted as the function of the temperature. The experiment results show the excess noises of the AlInP diodes are very similar at different temperatures and vary only with the avalanche width and the value of multiplication.

List of publication

Journal Publication

1. **L. Qiao**, J. S. Cheong, J. S. L. Ong, J. S. Ng, A. B. Krysa, J. E. Green, and J. P. R. David, "Avalanche Noise in $Al_{0.52}In_{0.48}P$ Diodes," *Photonics Technology Letters, IEEE,* vol. 28, pp. 481, 2016.
2. M. Hossain, S. Ray, J. Cheong, **L. Qiao**, A. Baharuddin, M. Hella, J. David, and M. Hayat, "Low-Noise Speed-Optimized Large Area CMOS Avalanche Photodetector for Visible Light Communication," *J. Lightwave Technol*, vol. 35, pp. 2315-2324, 2017.
3. **L. Qiao**, S. J. Dimler, A. N. Baharuddin, J. E. Green, and J. P. R. David, "An excess noise measurement system for weak responsivity avalanche photodiodes," *IOP Measurement Science and Technology*, vol. 29, 2018.
4. **L. Qiao**, J. S. Cheong, A. N. Baharuddin, J. S. Ng, A. B. Krysa, J. E. Green, and J. P. R. David, "Avalanche multiplication and excess noise in $Al_{0.52}In_{0.48}P$ Diodes from 298 K to 475 K," (In preparation)

Conference Publication

1. **L. Qiao**, J. S. Cheong, J. S. L. Ong, J. S. Ng, A. B. Krysa, J. E. Green, and J. P. R. David, "Noise performance of $Al_{0.52}In_{0.48}P$ avalanche photodiodes," Semiconductor and Integrated Optoelectronics, Cardiff, 2015.
2. J. S. Cheong, **L. Qiao**, A. N. Baharuddin, J. S. Ng, A. B. Krysa, and J. P. R. David, " $Al_{0.52}In_{0.48}P$ photodetector for underwater communication systems," Asia Communications and Photonics Conference, Hong Kong, 2015.
3. A. N. Baharuddin, J. S. Cheong, **L. Qiao**, A. B. Krysa, J. S. Ng, and J. P. R. David, "High temperature performance of $(Al_xGa_{1-x})_{0.52}In_{0.48}P$ visible photodiode," Semiconductor and Integrated Optoelectronics, Cardiff, 2017.

Contents

Acknowledgements I

Abstract II

List of publication IV

Journal Publication IV

Conference Publication IV

Chapter 1: Introduction 1

1.1 Introduction to photodetectors 1

1.2 Types of photodetectors 3

1.2.1 Photoconductor 3

1.2.2 Photomultiplier tube 3

1.2.3 Photodiode and Avalanche Photodiode 5

1.3 Motivation and Target Application 7

1.3.1 AlInP Application: Underwater Communication 8

1.3.2 AlInP Application: High Temperature Environemnt Detection 11

1.4 Organisation of the Thesis 12

Chapter 2: Background Theory 14

2.1 Impact Ionisation in Semiconductors 14

2.2 Avalanche Multiplication 15

2.3 Avalanche Noise 18

2.4 Review of Front-End Design 20

2.4.1 High Impedance Amplifiers 20

2.4.2 Impedance Match Amplifiers 21

2.4.3 Transimpedance Amplifiers 21

2.5 Light source selection 23

Chapter 3: Measurement Technology 27

3.1 Current Voltage Measurement 27

3.2 Capacitance Voltage Measurement 28

3.3 Photomultiplication Measurement 29

3.4 LED Drive Circuit 31

3.5 Phase Sensitive detection 31

3.6 Review of Excess Noise Measurement Systems 33

3.6.1 Bulman's System 34

3.6.2 Ando and Kanbe's System 35
3.6.3 Xie's System 35
3.6.4 Lau's System 36
3.6.5 Green's System 37
3.6.6 Summary of Prior Noise Measurement Systems 38
3.7 Conclusion 39
Chapter 4: Weak Optical Input Power Noise Measurement System 40
4.1 Introduction 40
4.2 Noise Measurement System 41
4.2.1 A Noise System Design Requirements 43
4.3 The Transimpedance Amplifier – Circuit Description 44
4.3.1 TIA Noise Performance 45
4.3.2 TIA Noise Performance using SPICE 47
4.3.3 Characterisation of the Transimpedance Amplifier Frequency Response 48
4.3.4 Selection of a suitable op-amp 49
4.4 Bandpass Filter and Effective Noise BandWidth (ENBW) 51
4.5 Nose Power Meter 53
4.6 System Testing 55
4.6.1 Dark current Limit 56
4.6.2 Series resistance limit 57
4.7 Measurement Results 60
4.7.1 Layer Details 60
4.7.2 CV Measurement 61
4.7.3 IV Measurement 62
4.7.4 Photo-multiplication Characterisation 63
4.7.5 Excess Noise Characterisation 65
4.7.6 Comparison of the Excess Noise With Low and High Input Current 67
4.7 Conclusion 69
Chapter 5: Room Temperature Avalanche Multiplication and Excess Noise Characteristics of AlInP Diodes 70
5.1 Introduction 70
5.2 Layer Details 70
5.3 Electrical Characterisation 72
5.3.1 IV Measurement 72

5.3.2 CV Measurement 73
5.4 Photomultiplication Characteristics 75
5.5 Excess Noise Characteristics 77
5.6 Modelling 79
5.6.1 Random path length (RPL) model 79
5.6.2 Results 81
5.7 Summary 82
Chapter 6: High temperature performance of AlInP Diodes 84
6.1 Introduction 84
6.2 Layer Details 85
6.3 IV Measurements 85
6.4 CV Measurements 88
6.5 Photomultiplication Characteristics 88
6.6 Excess Noise Measurements 91
6.6.1 High Temperature Excess Noise Set-up 91
6.6.2 Results 93
6.7 Modelling Results 97
6.7.1 Effective Impact Ionisation Coefficients 97
6.7.2 Modelling Multiplication Results 100
6.8 Summary 102
Chapter 7: Conclusion and proposed further work 103
7.1 Conclusion 103
7.1 Proposed further work 104
Reference 106
Appendix A: Electric Field Profile Modelling 116
Appendix B: Derivation of the transimpedance amplifier (TIA) transfer function V_o/I_{ph} . 119
Appendix C: Derivation of the transimpedance amplifier (TIA) output noise voltage 121
C1 Input noise voltage transfer function V_o/v_n 121
C2 Feedback resistance noise voltage transfer function V_o/v_{nf} 123
C3 Input noise current transfer function V_o/i_n 124
C4 Total Output noise voltage transfer function 124

Chapter 1: Introduction

Two related topics are investigated in this thesis. Firstly, the development of electro-optical measurement systems. Secondly, the characterisation of AlInP and AlGaInP avalanche photodiodes (APDs) from room temperature to 475 K.

1.1 Introduction to photodetectors

Photodetectors are used to detect optical signals which have properties including energy, E and wavelength, λ. These optical signals are converted into electrical signals (current and voltage signals). The diagram of the electromagnetic spectrum from gamma rays to radio is shown in Figure 1.1. The relationship between the energy and wavelength is [1]

$$E = \frac{hc}{\lambda} \tag{1.1}$$

Where h is the Planck's constant, 6.63×10^{-23}, and c is the speed of the light. There is no detector that covers the whole range of the electromagnetic spectrum. Therefore, it is important concentrate on the design of high sensitivity photodetector in a particular range of wavelengths.

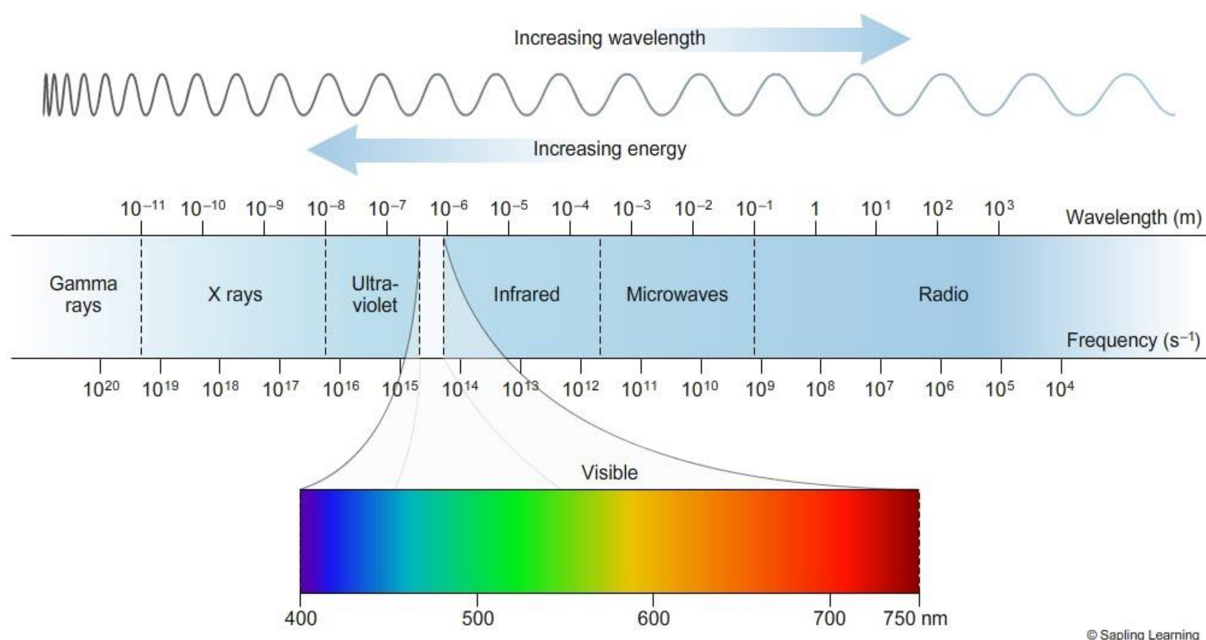

Figure 1.1: Schematic diagram of the electromagnetic spectrum [2].

The photodiode is one of the most important components in the optical communication system. In general, the performance of a particular optical communication system will improve with improving photodiode performance. Three metrics of photodiode performance are.

1. Quantum Efficiency

Quantum efficiency is the likelihood that any incident photon will generated the number of the electron hole pair. The responsivity, which is the ratio of the photocurrent to the optical power generating the photocurrent is related to the quantum efficiency. Therefore, for a given wavelength (which is no longer than the material cut off wavelength), the responsivity increases with quantum efficiency.

2. Response Speed

The response speed of the photodiode is limited by one of two factors, firstly the diode is said to be RC limited if the time constant RC limits the diode's capacity to detect high frequency signals. Where C is capacitance of the depletion region and R is the total resistance of the diode and any load circuit. Secondly the diode is said to be transit time limited if the detection of high frequency signals is curtailed by the time required for carriers to transit the depletion region.

3. Device Noise

The information contained in the signal is not easily extracted when the signal is corrupted by noise. It is important to design the device to have as little noise as possible in order to detect the lowest amplitude signals. Device noise is also a key factor in determining the signal to noise ratio (SNR) of an optical communication system. There are two main factors which contribute to the noise of a photodetector, shot noise and thermal noise. Thermal noise is the internal device noise generated by series resistance. Shot noise is contributed by the current. In avalanche photodiodes, excess noise is an additional noise source that arises due to the randomness in the ionization process. The detail of this process will be discussed in chapter 2. The purpose of designing the APD is to get the maximum useful internal gain with the associated optimum excess noise.

1.2 Types of photodetectors

This section reviews some major types of photodetectors and illuminates their operating principles and some advantages and disadvantages of these photodetectors are given.

1.2.1 Photoconductor

A photoconductor consists of a slab of semiconductor with two ohmic contacts made on the opposite ends [3]. When light is injected into the semiconductor, carriers are generated by band-to-band transitions. When a moderate electric field is applied across the two terminals, the electrons ,with higher mobility, move more quickly through the semiconductor while holes move more slowly due to lower mobility. More electrons are attracted from one electrode in order to maintain charge neutrality until the holes reach the other electrode, resulting in a photoconductor gain up to 10^6 [4][5]. It is widely accepted that the gain of the photoconductor is equal to the recombination lifetime divided by the transit time for the minority electrons moving between the two contacts of the photoconductor [6][7].

The advantage of the photoconductor is low cost and ease of fabrication because of the simple structure. They are widely used for infrared detection from 1000 nm to 4800 nm [8]. However, it only can operate at a lower speed than the photodiode due to the high leakage current and it is not suitable for the high speed application.

1.2.2 Photomultiplier tube

Photomultiplier tubes (PMT) are used to detect light and convert it to an electrical signal [9]. PMTs are widely used in the high energy experiments, medical diagnosis and industrial measurement [10]. A PMT is a high vacuum glass tube with a photocathode, dynodes and an anode. The theory operation of the PMTs is that of the photoelectric effect and secondary electron emission. The construction of the PMT is shown in Figure 1.2. Incident photons release electrons from the photocathode due to the external photoelectric effect. Figure 1.2 represents the electrons which are emitted from the photocathode towards the first dynode and move to the second dynode, resulting in secondary electron emission. This secondary emission is repeated until the electrons are collected in the last dynode behind the anode. A

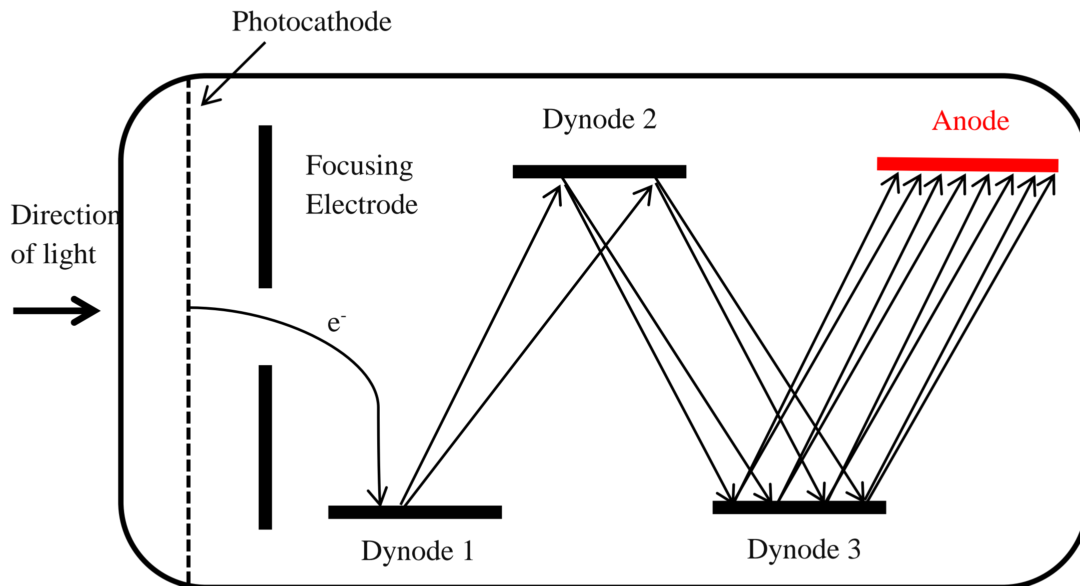

Figure 1.2: Theory operation of a PMT.

PMT may have 10 dynodes and each dynode may provide a gain of 4, for example. Therefore, the PMT can produce an overall gain of 4^{10} (around 10^6).

An advantage of PMTs is high gain, up to 10^6 and very small gain fluctuation [11]. Therefore, a PMT can be used for single photon detection from ultraviolet to near infrared wavelength because of high sensitivity. However, the PMT normally requires high operating voltages of more than 1000 V [12]. Moreover, the size of the PMT is larger than the other photodetectors, because it needs a larger vacuum tube. Commercial PMTs have quantum efficiency of more than 40 % for λ = 400 to 700 nm. QE reduces to around 20 % for λ between 700 to 900 nm. The lowest quantum efficiency of PMTs is less than 2.5 % at λ between 900 to 1600 nm [12]. For example, the Hamamatsu NIR PMT with InP/InGaAs has spectral response from 950 nm to 1700 nm, they need to reduce the dark current by using air cooling and very low QE of 2.5 % is obtained at 1600 nm [13].

1.2.3 Photodiode and Avalanche Photodiode

An optical receiver system normally consists of a photodiode, an amplifier and other additional circuits. The purpose of this system is to convert optical signals into electrical signals. The signal to noise ratio (SNR) of an optical receiver system with a photodiode is limited by the quantum efficiency and shot noise power of the photodiode, the noise level of the first stage amplifier and, to a much lesser extent, the other additional circuits. The SNR can be generalised as [14]

$$SNR = \frac{P_s}{N_{sn} + N_{Amp}} \quad (1.2)$$

Where P_s is the optical signal power, N_{sn} is the shot noise power at unity gain and N_{Amp} is the noise power of the amplifier. The SNR can be improved by reducing the background radiation and the amplifier noise. Impact ionisation provides internal current gain in avalanche photodiodes (APDs), which provides the opportunity to optimise the signal-to-noise ratio (SNR) of an optical receiver. Therefore, the APD is used to replace the *p-i-n* (PIN) photodiode in order to improve the SNR. APDs are used in many different areas, such as optical communication [15] and imaging [16] and over a range of wavelengths. The principle of operation of the avalanche photodiode (APD) is that carriers are accelerated under high electric field and obtain momentum when they are drifting. Carriers can create electron-hole pairs through impact ionisation when they have enough energy. The impact ionisation process will be described in chapter 2. This will increase electrical output signal.

The SNR of an optical receiver with APD can be viewed as [14]

$$SNR = \frac{P_s}{F \cdot N_{sn} + N_{Amp} / M^2} \quad (1.3)$$

Where F is the excess noise factor of the photodiode and M is the mean avalanche multiplication factor. When the amplifier noise is higher than the photodiode noise, the SNR of the system is limited by the amplifier noise. The SNR can be significant improved by operating the APD with gain provided the amplifier is nosier than the shot noise of the diode when it is operated without multiplication. Figure 1.3 shows that the advantage of an APD over a PIN photodiode as a function of the avalanche multiplication factor for two situations. The optimum SNR can be obtained with the APD operating at high gain when the APD noise is equal to the amplifier noise floor. It is necessary to investigate the excess noise properties of the APD in order to optimise the overall SNR of a receiver system.

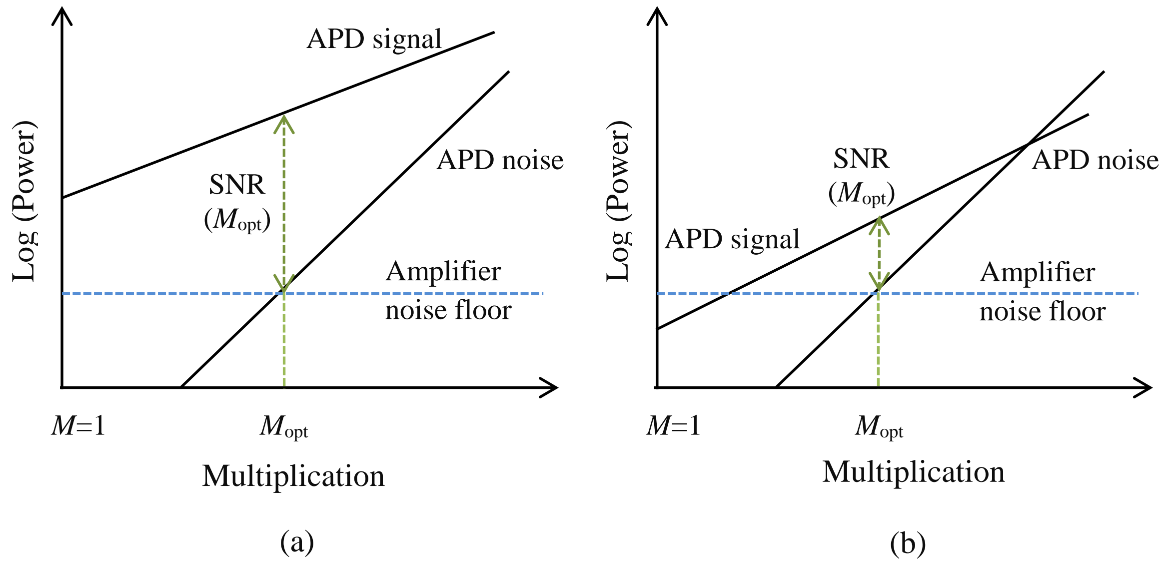

Figure 1.3: Schematic diagram shows the advantage of an APD over a PIN photodiode when the unmultiplied signal is a) above the amplifier noise floor and b) below the amplifier noise floor. Optimum SNR is achieved by operating the APD with gain when the APD noise is equal to the amplifier noise floor.

Impact ionisation rate is a key property of semiconductor materials related to the design of APDs. Knowledge of the ionisation coefficients is required to appropriately design the APDs doping and layer thicknesses. New materials must be characterised to support the design of devices. For thick avalanching structures, where the carriers can be assumed to be in equilibrium with the electric field, the excess noise factor (F) was described by McIntyre [17] as

$$F = kM + (1-k)(2-\frac{1}{M}) \tag{1.4}$$

where k is the ionization ratio given by β/α and α/β associated with M_e and M_h, respectively. α and β are ionization coefficients for electrons and holes respectively and they are the reciprocal of the average distance that a carrier travels before initiating an impact ionization event.

1.3 Motivation and Target Application

This thesis introduces several additions or changes to the experimental methods used to measure excess noise in avalanche photodiodes including:

- To avoid the use of lasers as light sources in excess noise measurement.
- Design a higher sensitivity avalanche noise measurement system which can reliably measure the excess noise factor of devices where the primary photocurrent of the measured device is weak (10 nA). Shot noise should be measureable in this un-multiplied photocurrent. This primary photocurrent is approximately two orders of magnitude lower than the primary photocurrents routinely used in measurements at Sheffield and more than one order of magnitude less than reported by Lau *et al.* [18]. This new measurement front end will be used to characterise the multiplication, excess noise of $Al_xGa_{1-x}InP$ avalanche photodiodes and to determine the ionisation coefficients for this material.

The laser may be replaced with the LED to perform the excess noise measurement. This carries several benefits, and some drawbacks. Normally, a HeNe laser is quite expensive (>£1000), but LEDs are inexpensive (much less than £10). It is very difficult to find a low noise laser of the correct wavelength to match the peak response of some materials, because only certain gas lasers, which are low noise can be used to perform excess noise measurements. For example, the peak response of AlInP is at 480 nm, the nearest He-Ne laser line is at 543 nm. An LED can provide more wavelengths than lasers because the material band-gap used to make LEDs can be engineered by the addition of ternary or quaternary alloys to produce particular emission wavelengths. LED can be electrically chopped by using a signal generator. A source of mechanical jitter can be removed making lock-in-detection easier. Many lasers have some RIN (relative intensity noise) which is described in chapter 2, making them unsuitable for noise measurements. In this work every LED used has exhibited no measurable additional noise. The advantages of the LED are: cost, number of available wavelengths and low noise compared to many types of laser and the disadvantages are: the LED cannot be focused to a very small spot like a laser. The power per unit area of an LED is often lower than a laser (due to the spot size). Moreover, the large photocurrents can result in device heating and also distortion of the electric-fields under which the APD operates [19]. If the excess noise measurements could be done at very low optical powers and hence photocurrents, we could use LEDs which avoid both the aforementioned problems.

The new measurement system can operate using a range of LEDs, even when the power of the LED is low (primary photocurrent as low as 10 nA is acceptable). Therefore, the excess noise characteristics yielding pure electron injection of the $Al_xGa_{1-x}InP$ avalanche photodiodes using a range of LEDs can be investigated. In the prior system, it is very difficult to perform the pure electron injection excess noise measurement using gas laser because of the low primary photocurrent. Furthermore, the peak wavelength of these $Al_xGa_{1-x}InP$ devices at low operation voltage is from 480 nm to 655 nm. The optimum wavelength of the LED makes the measurement possible.

1.3.1 AlInP Application: Underwater Communication

Underwater communication plays an important role in a wide range of applications, such as long term and real time ocean observation and event forecasting [20]. An example of the underwater acoustic sensor networks [21] is shown in Figure 1.4. It has been used for long term and real time ocean observation in order to detect earthquakes, storms, pollution and other disaster events and to explore the underwater environment. Autonomous underwater vehicles (AUV) are used to improve the performance of these systems. They need high bandwidth for control communication and data transfer between the operators and the AUVs near the seafloor [22].

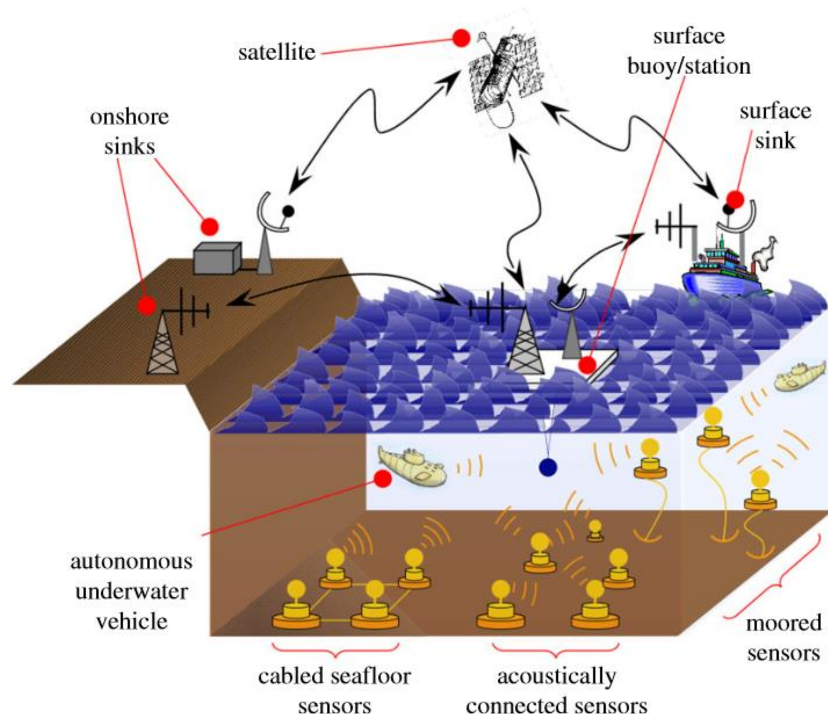

Figure 1.4: The diagram of the underwater acoustic sensor networks [22].

In general, there are three types communication systems can be uses as free space underwater communication.

1. Acoustic Communication Systems.
2. Electromagnetic (EM) Communication Systems.
3. Optical Communication Systems.

The acoustic communication system is the most popular type of the underwater communication which the data transmission distances can be up to 20 km [23]. However the drawback of this system has limited data rates up to only hundreds of kilobit per second (kbps) [24]. Moreover, acoustic waves are affect by multi-path propagation especially at the surface and bottom of swallow waters [22]. This will cause inter symbol interference (ISI) which is a form of signal distortion in telecommunications where one bit interferes with subsequent bits at the receiver and cause the overall system to become less reliable [25]. In addition, acoustic waves suffer from the other environmental noise sources such as ships, pumps, animals etc. [26][27].

Electromagnetic (EM) communication systems suffer from limited distance for data transmission [28]. For the spectrum of EM waves, visible light shows the least attenuation compared UV, infrared and microwave regions [29][30].

The advantage of an optical communication system is that it can give high data rates from Mbps to Gbps which can reduce power consumption and support video and the high resolution picture transfer over a short transmission distance of around 100 m [31][32]. Tsuchida *et al.* [28] have developed an underwater optical detector system for recording crayfish muscle and neuronal activities. Fung *et al.* [33] have reported an underwater optical system used on robots communicating using a green laser. Therefore, optical communication systems are more suitable than traditional acoustic communication systems for underwater applications.

Optical underwater communication systems require a high-sensitivity detector with a peak responsivity at approximately 480 nm, as this corresponds to the maximum transmittance in seawater [34]. There are several semiconductor materials which can detect light at 480 nm, such as Si and GaP [35][36], however these also have a broad spectral response and so will be sensitive to the presence of extraneous light sources at other wavelengths.

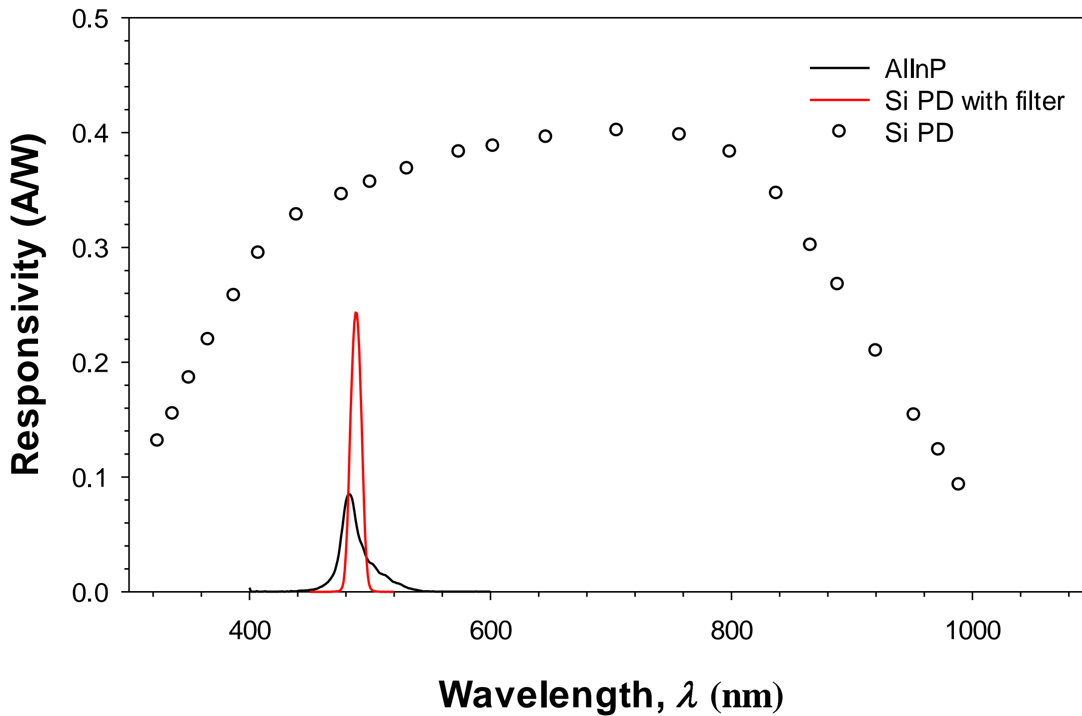

Figure 1.5: Responsivity versus wavelength in a 1 µm AlInP PIN device (black line) and Si commercial photodiode with filter (red line) and without filter (black circles) at punch-through voltage.

Using these broadband detectors will require optical band-pass filters with a high rejection ratio and centre wavelength of approximately 480 nm, which adds cost and complexity to the system. Consequently an inherently narrow spectral response photodetector is preferred. Zhang *et al.* [37] demonstrated that an $Al_{0.52}In_{0.48}P$ (hereafter AlInP) PIN photovoltaic detector with a $Ga_{0.52}In_{0.48}P$ p^+ cladding has a peak spectral response at 480 nm and a full-width-half-maximum (FWHM) of 45 nm. Later, Cheong *et al.* reported the photo-response of an AlInP homo-junction PIN diode with a narrower FWHM of 22 nm and an effective responsivity of 18 A/W, with a multiplication factor of 167 at approximately 480 nm [38]. This was achieved by employing a thick p^+ AlInP cladding, which yields small FWHM but has the undesirable effect of the peak responsivity. The peak reosponse wavelength shift slightly to longer wavelength with increasing cladding thickness. Exploiting multiplication factor from the diode however allowed them to eventually achieve the reported responsivity value [38].

Although avalanche multiplication can increase the sensitivity of an optical receiver, the maximum useful gain is ultimately limited by the associated excess noise that originates from the impact ionization process. The ionization coefficients measured by Ong *et al.* [39] showed that β/α is 0.4 - 1.0 over the electric-field range of 400-1300 kV/cm consequently (1.4) would

suggest that AlInP should exhibit high excess noise and that any amplification of the photocurrent due to impact ionization would be matched by an almost similar increase in the excess noise, thereby not improving the overall sensitivity of the system.

However, it is now well known, both experimentally and theoretically [40][41][42] that, for a given *M*, the excess noise reduces with decreasing avalanche layer thickness due to the increasing significance of the carrier 'dead space', defined as the minimum distance a carrier has to travel in the direction of the electric-field to gain the ionization threshold energy. This dead space has the effect of reducing the randomness in where carriers ionize and hence reduces the excess noise. The beneficial effect of the dead-space increases as the avalanching width reduces and the lower limit that can be practically utilized is determined by dark currents due to quantum mechanical tunnelling across the band gap at high electric fields, i.e. the tunnelling current. Being the widest bandgap material which can be grown lattice matched to GaAs, and having an indirect band gap, AlInP is expected to have negligible tunnelling effect even at high-fields > 1 MV/cm and therefore it should be possible to utilize a thin avalanche layer to give low dark currents and low excess noise simultaneously.

1.3.2 AlInP Application: High Temperature Environment Detection

There is a need for avalanche photodiodes (APDs) that are capable of operating at high temperatures in areas such as oil well logging [43], space exploration [44], high energy physics [45] and radiation detection [46][47]. A silicon APD can cover the visible wavelength and cost is very low. However, the dark current of the silicon APD will increase more than five orders of magnitude from room temperature to 473 K [48] reducing the sensitivity of the APD. Guo *et al.* [49] showed that the dark current of the 4H-SiC APD increases by only one orders of magnitude from room temperature to 491 K however the cutoff wavelength of the SiC is limited to 380 nm [50], less than the visible wavelength and cost of the SiC is relatively high. Zhou *et al.* [51] shows that the GaN schottky diode can work in the temperature range of 298 to 473 K. Also, the cut-off wavelength of the GaN is limited to 360 nm [52]. There is a need for APDs capable of operating in the visible part of the spectrum at temperatures beyond that of silicon.

The temperature sensitivity of the dark current in a semiconductor is linked to its bandgap [3] so relatively wide bandgap IIV-V semiconductor materials such as AlGaAs and AlGaInP, with bandgaps from 1.42 eV to 2.34 eV should have better dark current performance than silicon

while covering the visible part of the spectrum [53][54]. Zheng *et al.* [55] have reported that the temperature dependence of the multiplication and excess noise of $Al_xGa_{1-x}As$ up to 400 K.

$Al_{0.52}In_{0.48}P$ (hereafter AlInP), which has the widest bandgap at 2.34 eV has a further advantage that it can be grown lattice matched to GaAs [56]. Ong *et al.* [39] have showed that homojunction AlInP PINs have a low dark current density which is less than 6 nA/cm^2 at 95% of breakdown voltage at room temperature. Qiao *et al*. [57] have reported that the AlInP has a very low excess noise corresponding to $k = 0.11$ in the 0.04 µm structure at room temperature and no tunnelling current was observed in AlInP even at high-fields > 1 MV/cm.

There are presently no reports on characterization of this material system at high temperatures. In chapter 6, excess noise and multiplication data is presented that was obtained from a series of AlInP PIN and NIP diodes with nominal avalanche layer thickness ranging from 0.04 to 1.0 µm from 298 to 475 K and the temperature dependence of their dark current and impact ionization coefficient.

1.4 Organisation of the Thesis

In chapter 2, a description of impact ionisation, the APD gain mechanism and the excess noise factor is presented. A review of the front-end circuits for the optical system applications is presented. The noise properties of semiconductor diode lasers, He-Ne lasers and LEDs are also discussed.

Chapter 3 describes some characterisation measurements including current voltage, capacitance voltage and photo-multiplication measurements. The second half of this chapter introduces the previous excess noise measurement systems.

In chapter 4, A high sensitivity system for measuring the excess noise associated with the gain in avalanche photodiodes (APDs), using a transimpedance amplifier front-end and based on phase-sensitive detection is described. The system can reliably measure the excess noise factor of devices with primary photocurrents as low as 10 nA, which is more than one order of magnitude better than the previous reported systems. The impact ionization process in nominally 1 µm $Al_xGa_{1-x}InP$ is described. The multiplication and excess noise characterisation as the aluminium fraction increases is presented.

Chapter 5 represents the multiplication and excess noise characteristics of a series of AlInP homo-junction PIN and NIP diodes with *i* region widths ranging from 0.04 µm to 1 µm, using

442 nm and 460 nm wavelength light. Excess noise measurements of a separate absorption multiplication avalanche photodiode (SAM-APD) with a nominal multiplication region width of 0.2 µm are also reported.

Chapter 6 details the temperature dependence of multiplication and excess noise of series of AlInP diodes from 297 K to 475 K. The temperature dependence of the ionisation coefficients in AlInP diodes are also extracted.

Chapter 7 concludes the thesis and provides a summary of the results and some ideas for future work.

Chapter 2: Background Theory

This chapter describes the impact ionisation processes, the local model multiplication and excess noise factor for pure electron injection and pure hole injection. The front-end circuits which are used in optical systems applications are presented. The last section reviews the noise properties of the semiconductor diode laser, the He-Ne laser and the LED.

2.1 Impact Ionisation in Semiconductors

The imapct ionisation process provides a mechanism to increase to the photocurrent in avalanche photodiodes. Figure 2.1 shows the impact ionisation of an electron (hole) initiated in the conduction band (valence band) which creates an electron-hole pair where the electron is promoted to the conduction band and the hole is left behind in the valence band. The minimum energy required for impact ionisation or the impact ionisation threshold energy, E_{th} is strongly dependent on the bandgap of the semiconductor. The free carrier energy must exceed the ionisation threshold energy for ionisation to occur. The threshold energy is always higher than the bandgap and the extra energy is lost as phonons or in other pathways that do not lead to the promotion of a secondary carrier. Impact ionization [58] properties are described by ionization coefficients, α and β for electrons and holes respectively. They describe the reciprocal of the average distance that carrier travels before initiating an impact ionisation event. This distance is often much smaller than the device depletion region.

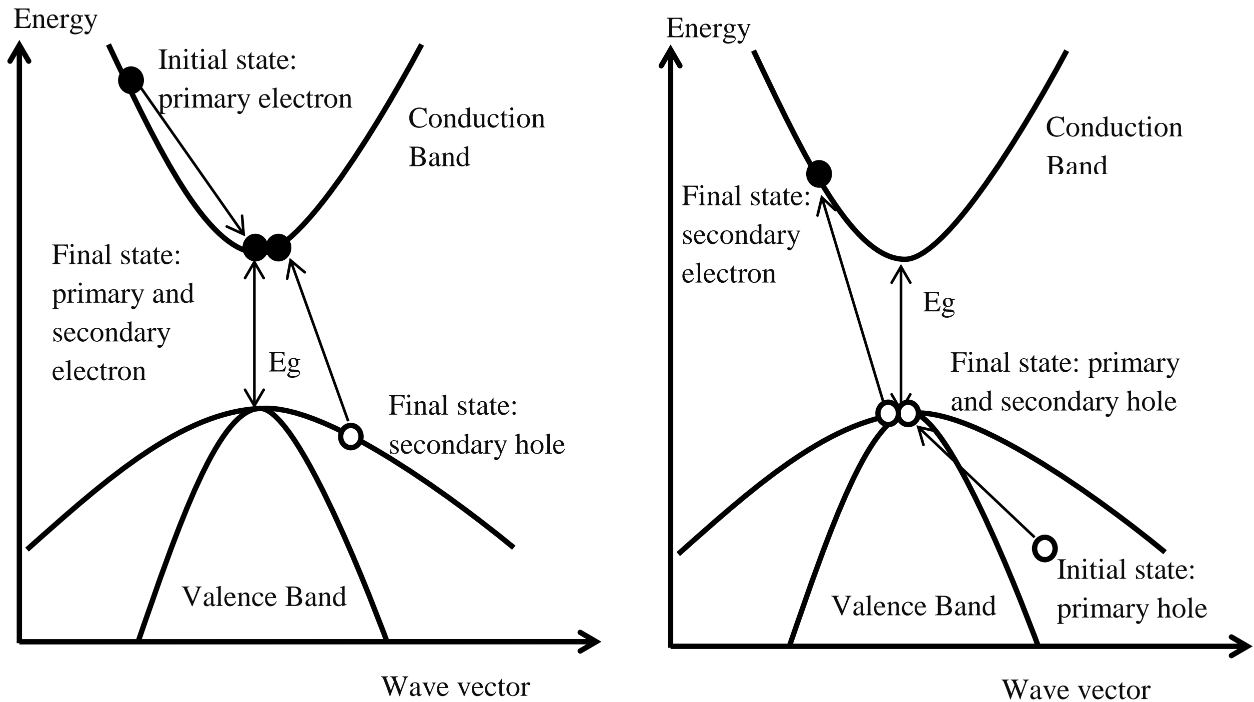

Figure 2.1 Schematic energy band diagram of the electron (left) and the hole (right) initiated an ionisation event.

2.2 Avalanche Multiplication

The avalanche photodiode has a high electric field in the depletion region when it is biased at high voltage. When a free carrier obtains sufficient energy the impact ionisation process can occur. A diagram of the impact ionization process in the depletion region, w, is shown in Figure 2.2. Assume that an injected electron diffuses into the high field region from the left at position $x = 0$. The initial injected hole is not shown in the diagram. The primary carrier creates a secondary e-h pair after it ionises the lattice. Having travelled a short distance, the second generation electron ionises the lattice generating a third e-h pair. Finally, the third generation electron ionises the lattice to produce a fourth e-h pair. In Figure 2.2, the multiplication for this pure electron injection condition is 5.

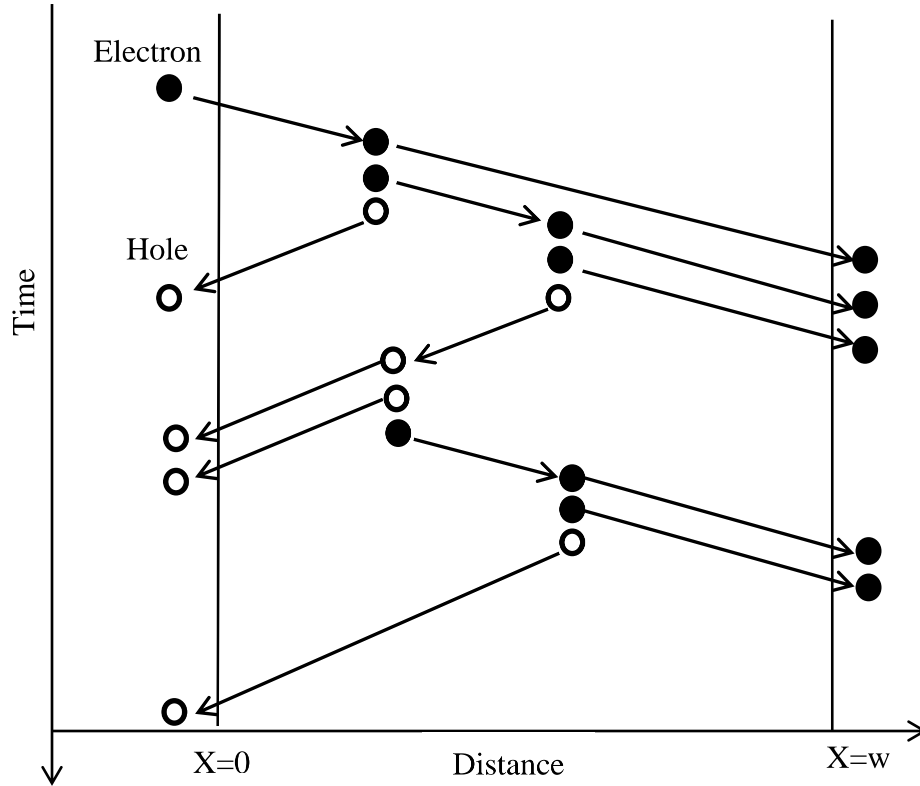

Figure 2.2: The multiplication with an initiating electron moving from the left of the multiplication region to right of the multiplication region shown schematically.

Now assume there is one electron-hole pair injected at position x in the avalanche region. The hole at position x will travel from the right to the left while the electron at position x will travel from left to right. The average of the total multiplication is [17],

$$M(x_0) = 1 + \int_x^{w_T} \alpha(x')M(x')dx' + \int_0^x \beta(x')M(x')dx' \tag{2.1}$$

The initial unity term, in (2.1), means there is an initial electron-hole pair has been generated at position x of the depletion region. First integral and second integral represent the mean number of electron-hole pairs generated in the depletion region between x and high field region with a width of w_T and the mean electron-hole pairs generated in the depletion region between x and 0, respectively. Ionization coefficients α and β only depend on the electric field and properties of the semiconductor material. The mean multiplication factor $M(x_0)$ can be transposed from (2.1),

$$M(x_0) = \frac{\exp(-\int_0^x (\alpha(x) - \beta(x))dx)}{1 - \int_0^{w_T} \left[\alpha(x) \exp(-\int_0^x (\alpha(x') - \beta(x'))dx') \right] dx} \tag{2.2}$$

The multiplication for pure electron injection at $x = 0$ can be written as

$$M_e = \frac{1}{1 - \int_0^{w_T} \left[\alpha(x) \exp(-\int_0^x (\alpha(x) - \beta(x)) dx') \right] dx} \tag{2.3}$$

Similarly, the multiplication for pure hole injection at $x = w_T$ can be expressed as,

$$M_h = \frac{1}{1 - \int_0^{w_T} \left[\beta(x) \exp(-\int_x^{w_T} (\alpha(x) - \beta(x)) dx') \right] dx} \tag{2.4}$$

The equations (2.3) and (2.4) can be simplified when the electric field region is uniform, such as ideal PIN structure because the ionisation coefficients are no longer a function of distance. The expression is given by,

$$M_e = \frac{1}{1 - \frac{\alpha}{\beta - \alpha} \left[\exp((\beta - \alpha) w_T) - 1 \right]} \tag{2.5}$$

and

$$M_h = \frac{1}{1 - \frac{\beta}{\alpha - \beta} \left[\exp((\alpha - \beta) w_T) - 1 \right]} \tag{2.6}$$

In the ideal PIN structure with uniform electric field, there is a simple way to extract the impact ionization coefficients of a material using M_e and M_h. The value of doping levels in the cladding layers needs to be high compared to the value of the unintentional doping in the avalanche region. Equations (2.5) and (2.6) can be transposed to express the ionization coefficients α and β in terms of M_e and M_h,

$$\alpha = \frac{1}{w_T} \left(\frac{M_e - 1}{M_e - M_h} \right) \ln \left(\frac{M_e}{M_h} \right) \tag{2.7}$$

and

$$\beta = \frac{1}{w_T} \left(\frac{M_h - 1}{M_e - M_h} \right) \ln \left(\frac{M_e}{M_h} \right) \tag{2.8}$$

The ideal PIN structure assumption is suitable for thick devices and it is most the convenient way to predict the multiplication when the dead space effect is negligible. However, for thin structures, even when the doping density in the cladding layer is high, cladding layer depletion can still be a significant fraction of the *i* region width and the electric field cannot often be assumed uniform in this situation.

2.3 Avalanche Noise

Since the impact ionisation process is inherently stochastic, the measured gain of an avalanche photodiode is the mean or average gain experienced by the ensemble of free carriers. This variation in gain manifests itself a an extra noise source, usually called the excess noise or multiplication noise. In many applications this limits the maximum useful gain of an APD. The excess noise factor, F, is the standard deviation of the avalanche gain [59] and it is defined as,

$$F = \frac{\langle M_i^2 \rangle}{\langle M_i \rangle^2} \tag{2.9}$$

Where M_i is the avalanche gain for each carrier and the measured ensemble multiplication, $M = < M_i >$ is the average value of M_i. McIntyre [17] has shown that the excess noise factor, F, can be expressed as a function of the avalanche multiplication, M, and the ratio of the ionization coefficient, k (= β/α). The electron is the more readily ionising carrier if $\alpha > \beta$ while $\alpha < \beta$ shows that the hole is the more readily ionising. The excess noise factor for pure electron initiated multiplication can then be calculated from ,

$$F_e(M_e) = kM_e + (2 - \frac{1}{M_e})(1-k) \tag{2.10}$$

and the pure hole initiated excess noise is,

$$F_h(M_h) = \frac{1}{k}M_h + (2 - \frac{1}{M_h})(1 - \frac{1}{k}) \tag{2.11}$$

Figure 2.3, (2.10) and (2.11) show that the excess noise factor depends on the ratio of the ionization coefficients and on the mean multiplication. Low excess noise factor can be obtained if the ratio of the ionization coefficients is large. It is very important to choose the carrier with the more readily ionizing carrier in order to obtain the lowest excess noise. Otherwise extremely high excess noise is produced when the 'wrong' carrier type is chosen. In a thick avalanche structure, the excess noise factor may be estimated using (2.10) and (2.11). The local model provides several design rules for APDs when dead space effects are not at work.

This McIntyre noise theory however only holds true in structures, where the carriers can be assumed to be in equilibrium with the electric field. It is now well known, both experimentally and theoretically [40][41][42] that the excess noise reduces with decreasing avalanche region width due to the carrier 'dead space', defined as the minimum distance a carrier has to travel to obtain the ionisation threshold energy. This dead space has the effect of decreasing the randomness in ionisation position and hence decreases the excess noise.

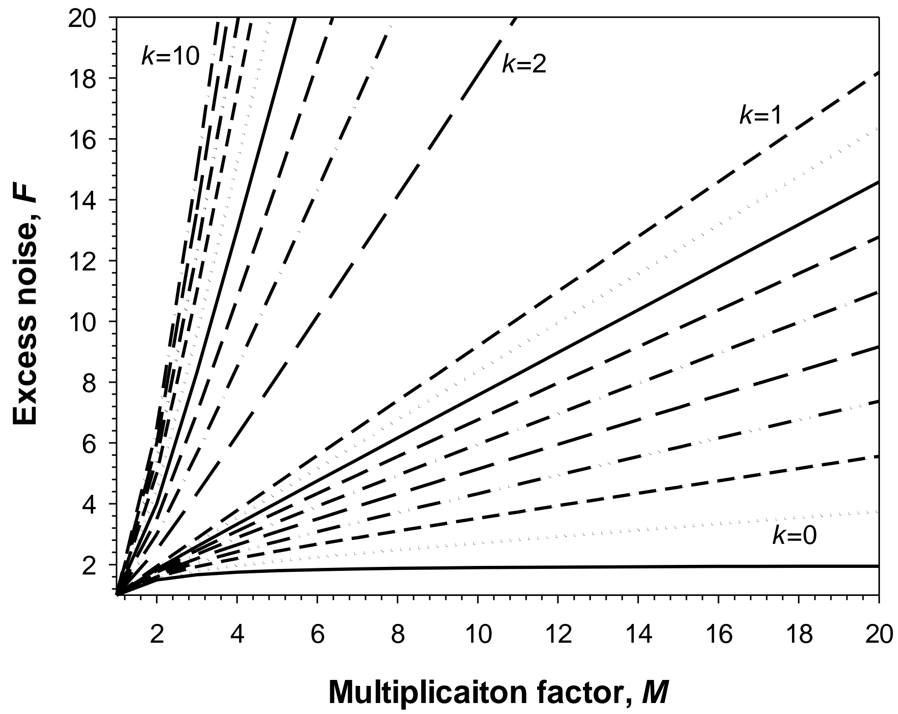

Figure 2.3: McIntyre's local noise model for $k = 0$ to 1 in steps of 0.1 and $k = 2$ to 10 in steps of 1.

2.4 Review of Front-End Design

This section briefly describes several of the front-end circuits which are commonly used in electronic systems with electro-optical detectors. These electronic circuits are used to convert photocurrent to voltage. The aim of this section is to highlight their relative merits and dis-advantages they can be sorted into three groups depending on their input impedance [60]:

1) High impedance amplifiers
2) Impedance matched amplifiers
3) Transimpedance amplifiers

2.4.1 High Impedance Amplifiers

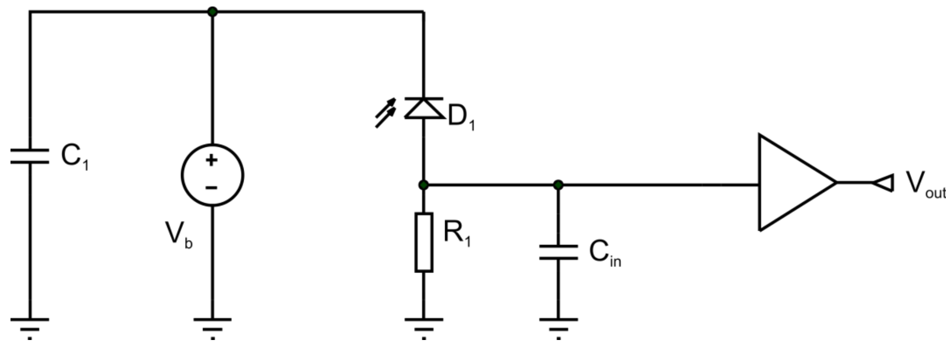

Figure 2.4: A generic high impedance amplifier

A generic high impedance amplifier is shown in Figure 2.4. A photodiode is reverse biased and it is connected to the resistance, R_1 in series. The photocurrent flows through the R_1 when the photodiode is illuminated. The theory of this type of the circuit is using large input impedance (R_1) to get maximum input voltage for the amplifier. However, the bandwidth of the system is determined by the R_1 and input capacitance C_{in} and the noise of the overall circuit is mainly dominated by the R_1. It is not possible to choose large resistance when the circuit is used for the high speed or low noise applications.

2.4.2 Impedance Matched Amplifiers

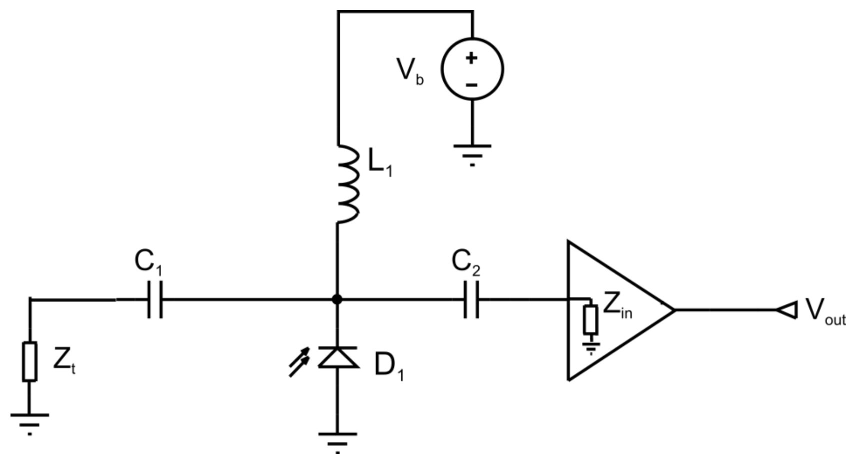

Figure 2.5: A typical impedance match amplifier.

The diagram of the impedance matched amplifier with fixed input impedance 50 Ω is shown in Figure 2.5. The limit of this topology is the impedance of the APD needs to be designed carefully in order to make sure all noise power which has been generated in the APD entering the noise measurement system. Xie *et al.* [61] have reported that this method was used to perform excess noise measurement. In Xie's system, the photodiode is terminated by Z_t is equal to 50 Ω. The noise power of the photodiode is separated equally between the input impedance of the measurement system, Z_{in} and the termination, Z_t.

2.4.3 Transimpedance Amplifiers

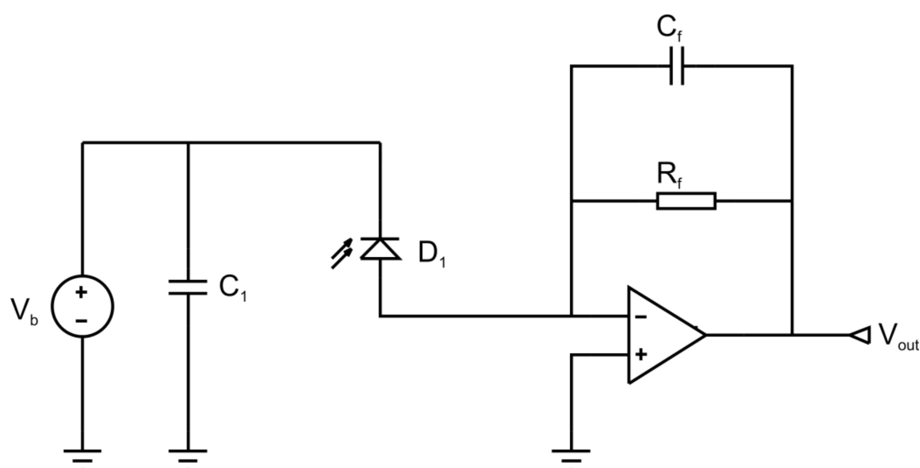

Figure 2.6: A simplified op-amp transimpedance amplifier.

A simplified op-amp transimpedance amplifier (TIA) shown in Figure 2.6. The TIA is used to convert the output current of the photodiode into a voltage. In general, TIA topologies based on an operational amplifier is require only a few external components [62]. The Texas Instrument OPA656 [63], OPA657 [64] and the Analog Devices AD9631 [65] are designed for this application depending on the bandwidth, gain and noise performance requirements. Sackinger [66] has reviewed the limitations for several transimpedance amplifier topologies in order to find their merits. The feedback resistance, R_f, determines the transimpedance gain which converts the current to voltage using Ohm's law $V_{out} = - I_{ph} \cdot R_f$ and a feedback capacitor, C_f, is used to stabilise the circuit. The TIA circuit may oscillate with excess input capacitance or without C_f [18]. Figure 2.7 illustrates the relationship between the frequency of the open loop gain and the feedback factor β. Consider the circuit in Figure 2.6 without C_f, the noise gain can be represented by the reciprocal of the feedback factor [67] and it is given by,

$$\frac{1}{\beta} = 1 + sR_f C_{tot} \quad (2.12)$$

Where C_{tot} is the total input capacitance which is includes the photodiode capacitance and PCB board layout capacitance.

The rate of closure is one key factor to determine whether the circuit is stable or not. If the rate of closure of the open loop gain response curve and the feedback factor curve which is shown in Figure 2.7 is 40dB/dec, the circuit will be unstable. Moreover, the inverting of the negative feedback can provide 180° phase shift of the feedback signal. Both the dominant pole of the

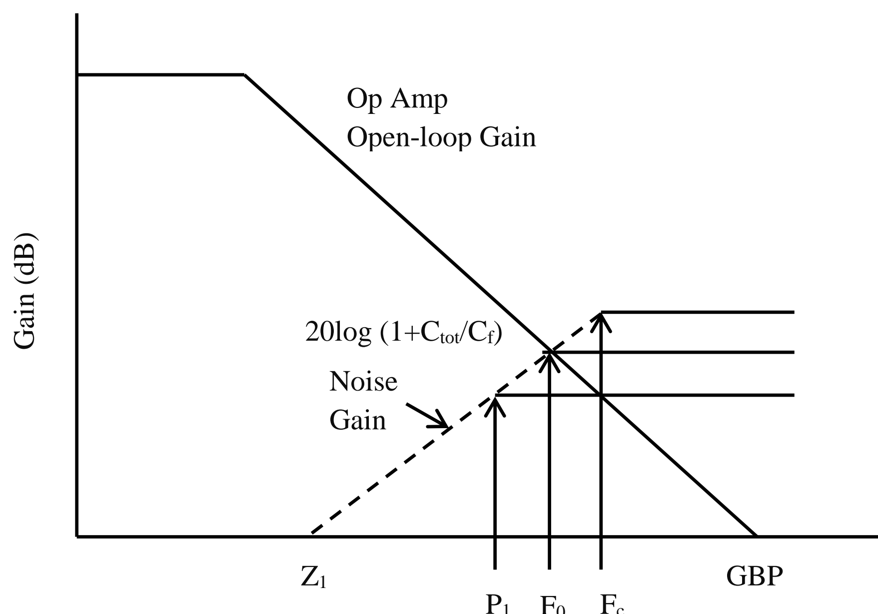

Figure 2.7: Bode plot magnitude of the noise gain intersects the open loop gain.

op-amp and feedback network will add 90° phase shift, respectively. Therefore, a total phase shift of 360° at $A\beta = 1$ will cause circuit to enter self-sustaining oscillation. It is necessary to use a compensation capacitor to stabilize the circuit by flattening the noise gain slope. The noise gain with C_f can be represented

$$\frac{1}{\beta} = \frac{1 + sR_f(C_{tot} + C_f)}{1 + sR_f C_f} \tag{2.13}$$

In Figure 2.7, optimum C_f is achieved at F_o when the noise gain is equal to the open loop gain of the op-amp. For the large input capacitance, the value of the $1 + C_{tot} / C_f$ is so large that the pole will be created outside the open loop gain curve at F_c. Choosing too large a C_f overcompensates the opamp and reduces the bandwidth of the TIA. Overcompensating will generate a pole inside the open loop gain curve (e.g. at P_1) although this reduction in bandwidth can be ignored in very low frequency applications.

Except in low frequency applications, it is necessary to know the maximum available bandwidth. There are four key parameters to determine the bandwidth of the TIA.

1) The input capacitance which is includes the photodiode capacitance and PCB board layout capacitance.
2) The transimpedance gain which is decided by feedback resistance.
3) The feedback capacitance and the parasitic shunt capacitance of the feedback resistance.
4) The gain-bandwidth product (GBP) of the op-amp.

In general, the signal of the photodiode is very small, so the noise level of the circuit needs to be kept as low as possible in order to avoid the TIA negatively affecting the signal to noise ratio. There are three key factors that influence the TIA noise.

1) Input current noise of the op-amp.
2) Input voltage noise of the op-amp.
3) Feedback resistance thermal noise.

The details of the noise model analysis and op-amp chosen will be discussed in chapter 4.

2.5 Light source selection

The optical output from a laser or LED has different kinds of fluctuations or noise such as intensity noise, phase noise [68] and beam pointing fluctuations [69]. For excess noise

measurements on semiconductor detectors, a quiet optical source is required. The following section describes the noise properties of several optical sources, some of which are used in the noise measurement system.

A He-Ne laser offers low noise, high and stable optical power compared to the semiconductor laser. The disadvantage of the He-Ne laser is it can only provide fixed wavelengths such as 543.5 nm, 593 nm, 632.8 nm, 1150 nm and 3390 nm. They are also very expensive such as Thorlabs red He-Ne laser (>£1000) [70]. The main reason why the semiconductor laser noise starts out high, drops, before increasing again is due to mode hopping of the frequency doubled YAG laser line. From Figure 2.8, the noise power of the He-Ne laser is quite stable in 20 minutes. Therefore, using a He-Ne laser to perform noise measurement is a reliable option [71].

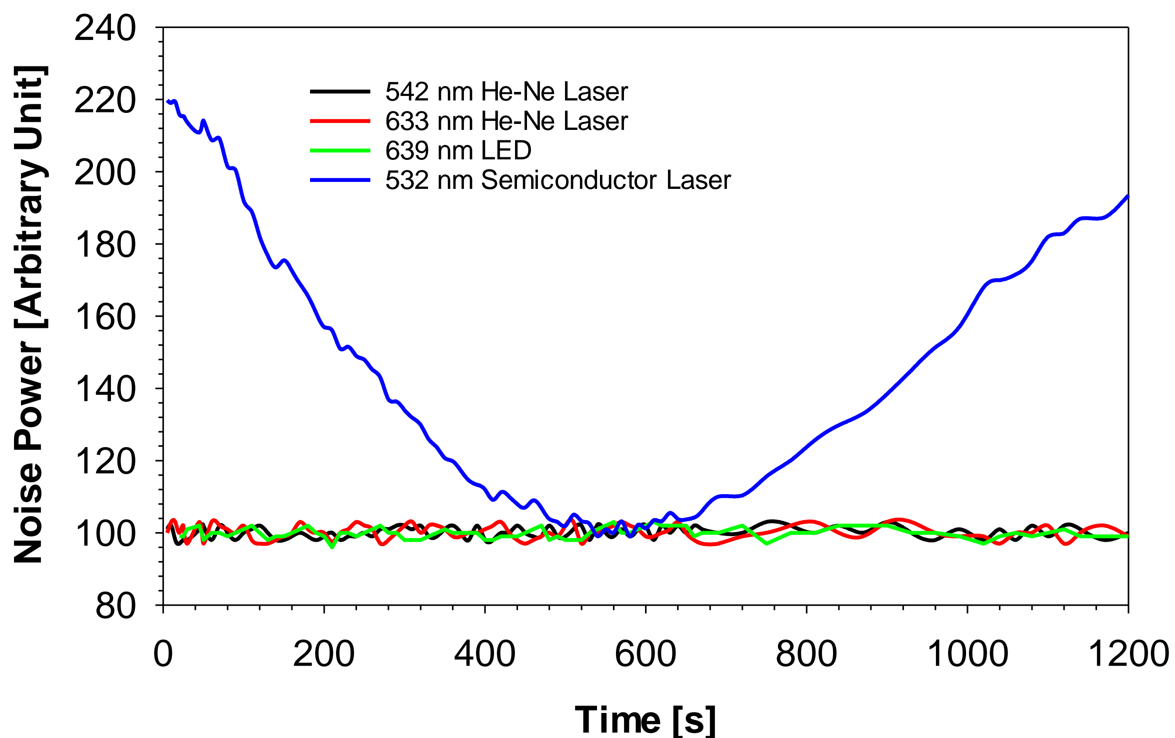

Figure 2.8: Noise Power vs Time. The noise power of the commercial device s2381 [15] was measured by using the semiconductor laser, the He-Ne laser and the LED. The output power of different types of optical source is same. The He-Ne laser and the LED provide almost same noise power.

For the LED, the photocurrent is very stable (+/- 1%) during an experiment. From Figure 2.8, the noise power did not change in 20 minutes. The problem of using LED is the spot size is very large and power density of the LED is very low compare to the He-Ne laser.

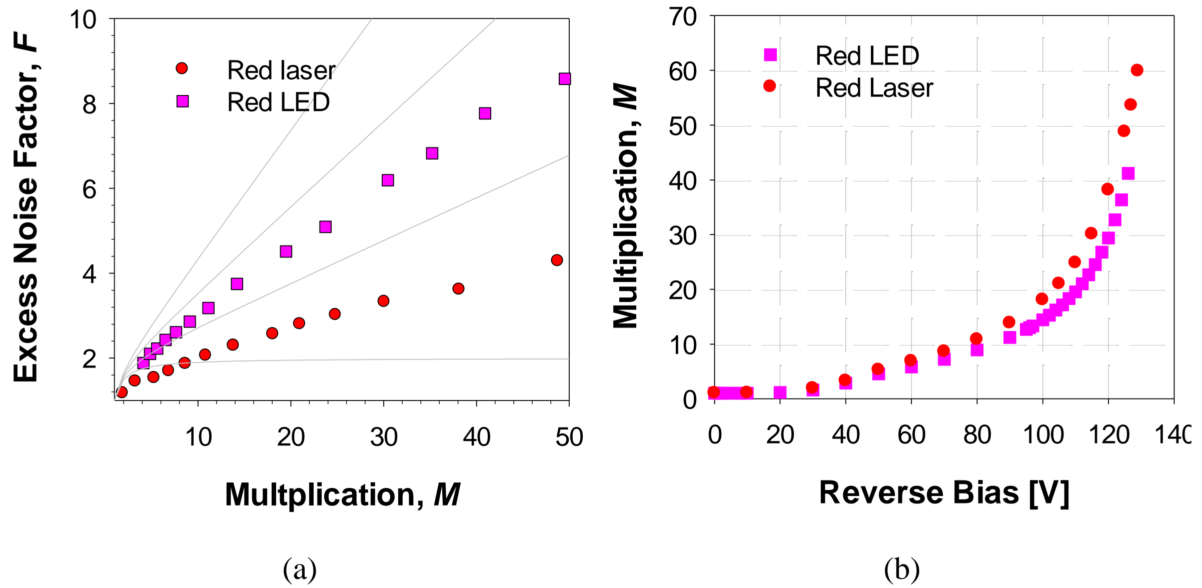

Figure 2.9: (a) Multiplication-Reverse bias voltage measurement for the silicon device Hamamatsu 2381. (b) Excess noise factor *vs* multipliaction for the silicon device s2381. Grey lines are McIntyre's curves with k = 0, 0.1, 0.2 0.3. Red closed circles and pink closed squares represent the device under 633 nm He-Ne laser illumination and 639 nm LED illumination, respectively.

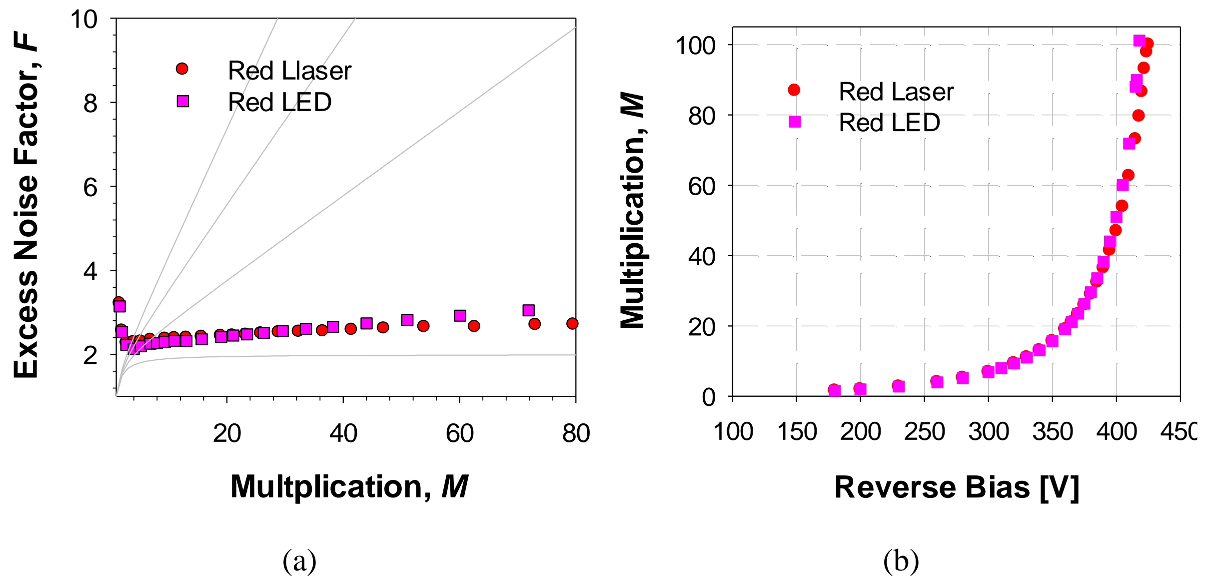

Figure 2.10: (a) Multiplication-Reverse bias voltage measurement for the large area silicon device Hamamatsu s8664 [72]. (b) Excess noise factor *vs*. multipliaction for the large area silicon device s8664. Grey lines are McIntyre's curves with k = 0, 0.1, 0.2 0.3. Red close circles and pink close squares represent the device under 633 nm He-Ne laser illumination and 639 nm LED illumination, respectively.

In order to show that similar noise measurements can be obtained from LED and laser illumination, a commercial silicon device s2381 [73] and s8664 [72] having diameters of 200 μm and 3 mm respectively were measured using 633 nm illumination from a He-Ne laser

and 639 nm from an LED. In Figure 2.9, Light is easily focused on the edge of the device and more noise could be produced than if the light was confined to the optical window. Figure 2.10 shows the LED is a suitable source to perform noise measurements with, if the spot size of the LED is sufficiently small compared to the device window area.

Chapter 3: Measurement Technology

Several different aspects of the performance of an APD needs to be characterised to judge its utility in a particular application. In this chapter, some characterisation measurements are described including current voltage (*IV*), capacitance voltage (*CV*) and photomultiplicaiton measurements. These measurements can supply very useful information about main properties of an APD, especially when a new sample diode becomes available. The previous excess noise measurement systems are also described in this chapter. All measurements were carried out on several devices on all wafers.

3.1 Current Voltage Measurement

Forward and reverse current voltage measurement is usually the first measurement after devices are manufactured. The breakdown voltage and the leakage current can be extracted by using reverse *IV* measurement and forward *IV* measurement, which allows series resistance to be evaluated. A Keithley 236/237/238 Source Measure Unit (SMU) is used to measure the current of the device under test (DUT) under forward bias voltage or reverse bias. The measurement is controlled through a desktop computer. Details of SMU are shown below.

	Source Measurement Unit	High Voltage Source Measurement Unit	High Current Source Measurement Unit
Model number	236	237	238
Max Measured Current Range	±100.000 mA	±100.000 mA	±1.0001 A
Max Applied Voltage Range(v)	±110.00	±1100.0	±110.00

Table 3.1: Performance of source measurement unit [74].

Forward current voltage measurement can be used to obtain the information about the quality of the material like dark current and series resistance. In order to get these information, the expression for the current can be expressed by [3],

$$I = I_s[\exp(\frac{qv}{nkT}) - 1] \quad (3.1)$$

Where I is the total current, I_s is the saturation current, q is the electron charge, v is the voltage across the diode, n is the ideality factor, k is the Boltzmann's constant and T is the absolute temperature. However, there is the series resistance R_s present in practice and it will become significant at high forward current. Equation (3.1) becomes

$$I = I_s[\exp(\frac{q(v - IR_s)}{nkT}) - 1] \tag{3.2}$$

The value of the R_s can be extracted by fitting (3.2) to the experiment data. The ideality factor close to 1 means the forward current is dominated by the diffusion current and the ideality factor close 2 shows the forward current is due to recombination current. The ideal diode should have low series resistance and ideality is close to 1.

Reverse current voltage measurements show the breakdown voltage, which can be combined with the capacitance voltage measurement to model the region widths and doping densities of the devices. Dark current plays an important role in an APD characteristic. The dark current density is a metric of fabrication and material quality. Excess noise cannot be measured easily if the dark current is very high (more than 100 µA).

3.2 Capacitance Voltage Measurement

Capacitance voltage measurements are used to obtain capacitance, built-in voltage, depletion width of the device. The depletion width, W can be determined from the measured junction capacitance of the device, C_j are given by [3],

$$C_j = \frac{\varepsilon_r \varepsilon_0 A}{W} \tag{3.3}$$

Where ε_r is the relative permittivity of the dielectric, ε_o is the permittivity of free space, A is the area of the semiconductor and W is the thickness of the depletion layer.

After extracting the total depletion width, W and the doping concentration, N, at a certain depletion width is,

$$N(W) = \frac{2}{q\varepsilon_r \varepsilon_0 A^2}\left(\frac{dV_t}{d\left[\frac{1}{C^2}\right]}\right) \tag{3.4}$$

The built in voltage can be estimated by a plot of $1/C^2$ against V_a. Transposing equation (3.4) is given by

$$\frac{1}{C_j^2} = \frac{2}{\varepsilon_r \varepsilon_0 AN} V_t = \frac{2}{\varepsilon_r \varepsilon_0 AN}(V_{bi} - V_a) \tag{3.5}$$

Assuming a one sided PN diode with an abrupt junction, a linear graph is produced by plotting $1/C^2$ against V_a and V_{bi} is the intercept when $1/C^2 = 0$.

3.3 Photomultiplication Measurement

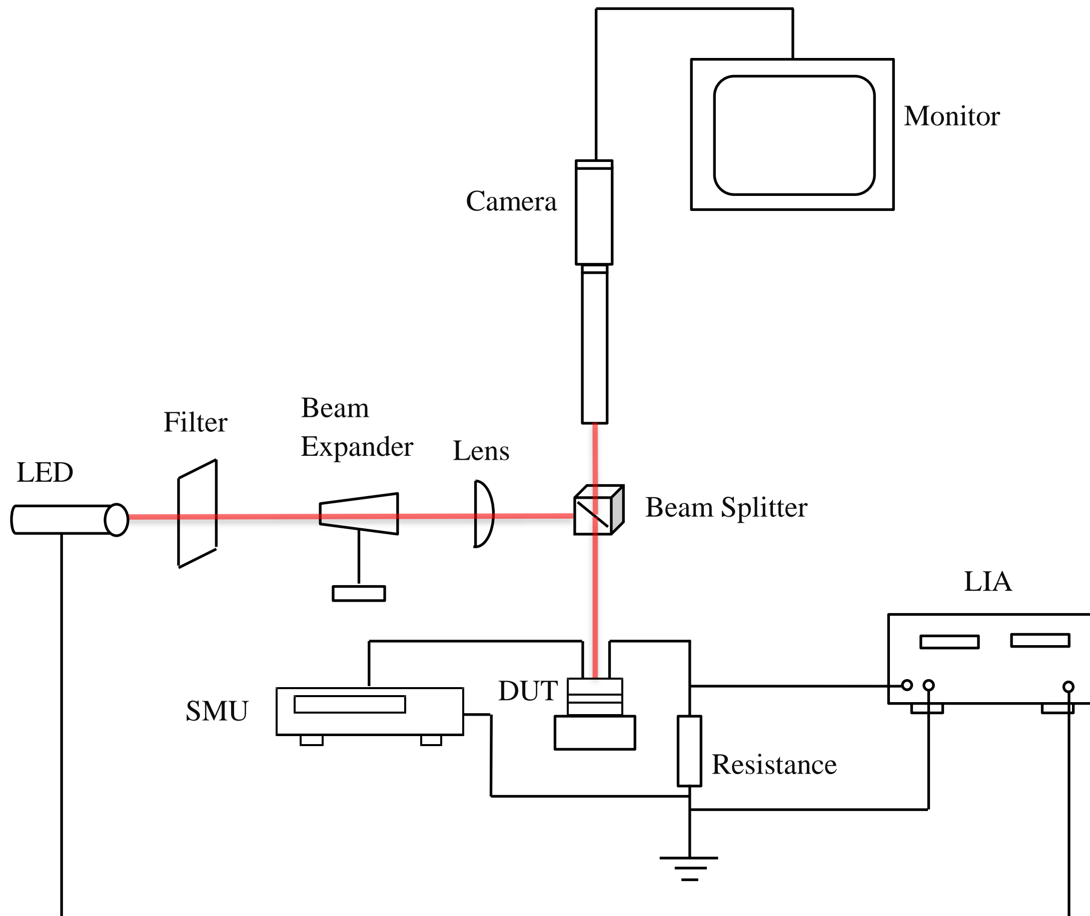

Figure 3.1: Photomulitplication measurement set-up.

The photomultiplication measurements were carried out when the diode was illuminated. The photogenerated carriers in the avalanche region will multiply via the impact ionisation process. A DC experiment can be used when the photocurrent is at least two orders of magnitude higher than the dark current. This is because the DC method measures total current which includes the dark current and the photocurrent. In this work, a phase sensitive detection method is used to ensure accurate photocurrent measurements [75]. This method can extract the photocurrent signal even when the photocurrent is three orders of magnitude lower than the dark current.

The photomultiplication factor is calculated by normalizing the photocurrent, I_{ph} to the primary photocurrent, I_{pr}. The avalanche gain is calculated as

$$M(V) = \frac{I_{ph}(V)}{I_{pr}} \tag{3.6}$$

Where $M(V)$ and I_{ph} are the avalanche gain and the photocurrent at a particular voltage, respectively. I_{pr} is the primary photocurrent. Under pure injection conditions the primary carriers are generated outside the depletion region and then diffuse into the high electric field region. The value of I_{pr} as a function of reverse bias voltage is obtained by measuring photocurrent at low reverse bias voltage values before the onset of any real multiplication. The primary photocurrent is fitted using a linear regression.

The diagram of the photomultiplication measurement set-up is shown in Figure 3.1. The chopping frequency of the LED (180 Hz) is controlled by the signal generator and provides a reference signal to the LIAs. The source measure unit (SMU) provides the reverse bias voltage to the DUT and resistor. The photocurrent is measured by using lock-in amplifier (LIA). In Figure 3.1, the value of the reistance in series with the device under test (DUT) needs be chosen correctly in order to make sure the overall voltage applied across the DUT is almost independent of the voltage drop across the resistor. Too small a resistance value results in a small signal which is corrupted by noise. However, a larger reisitance value will reduce the voltage across the APD significantly thereby affecting the measure multiplication at a given SMU voltage.

3.4 LED Drive Circuit

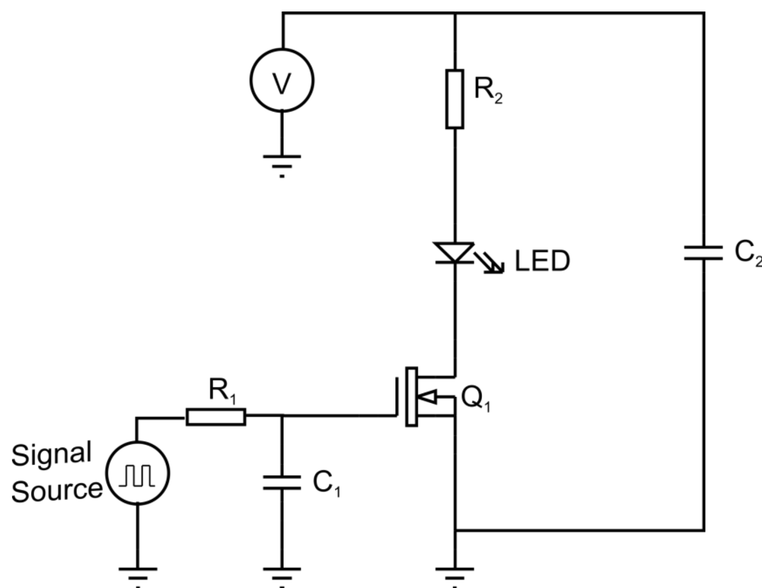

Figure 3.2: LED drive circuit.

An LED can be used to replace the laser in the multiplication and excess noise measurement setups. The circuit diagram of the LED driver circuit is shown in Figure 3.2.

The MOSFET Q_1 acts as a switch and is controlled by the signal generator, and standard silicon power MOSFET is acceptable (e.g. IRF510). The output of the signal generator is applied to a RC circuit R_1 and C_1 in order to set the rise time of the pulse signal. When the switch is turn on, the current flows through R_2 and the LED. R_2 is used to set the current in the LED. C_2 is used to smooth the output of the voltage power supply.

3.5 Phase Sensitive detection

Phase sensitive detection (PSD) is used to measure photocurrent at a fixed frequency. The chopper provides a reference signal to the lock-in amplifier and detection can be performed in synchronization with this fixed frequency. Therefore, the lock-in amplifier only measure the photocurrent at the same frequency and the dark current is ignored. PSD systems can recover signal below -60 dB.

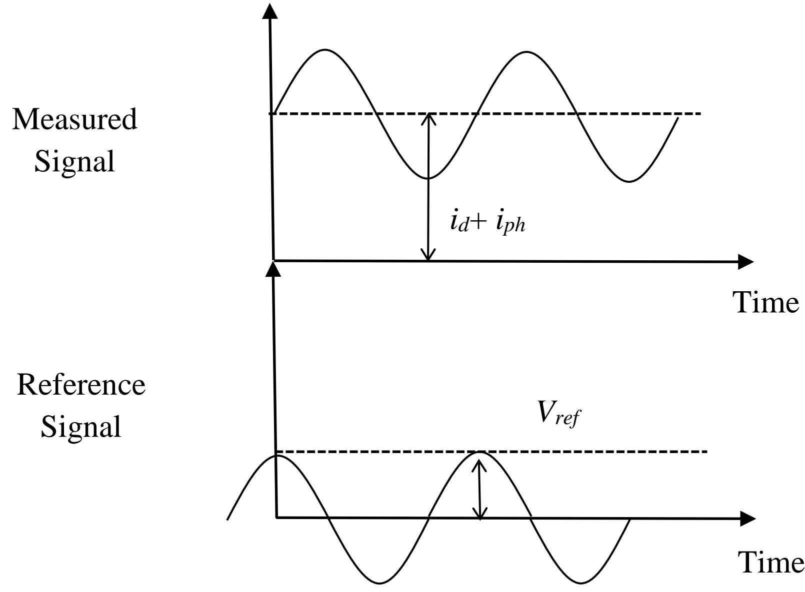

Figure 3.3: Diagram of phase-sensitive detection.

In figure 3.3, the expression for measured signal and reference signal is

$$V_{sig} = R\left[i_d + i_{ph}\left(1 + sin\left(\omega t - \emptyset_{sig}\right)\right)\right] \quad (3.7)$$

$$V_L = V_{ref} \sin\left(\omega t - \emptyset_{ref}\right) \quad (3.8)$$

Where V_{sig} is the measured signal, i_d is the dark current, i_{ph} is the photocurrent, R is the load resistance, ω is the chopping frequency, ϕ_{sig} is the phase measured signal, V_L is the reference signal and ϕ_{ref} is the phase reference signal.

According to (3.7) and (3.8), the mixing output is

$$V_L V_{sig} = V_{ref} R i_d \sin\left(\omega t - \emptyset_{ref}\right) + V_{ref} R i_{ph} \sin\left(\omega t - \emptyset_{ref}\right) + \frac{V_{ref} R i_{ph}}{2} \cos\left(\omega t - \emptyset_{sig}\right) - \frac{V_{ref} R i_{ph}}{2} \cos\left(2\omega t - \emptyset_{sig} - \emptyset_{ref}\right) \quad (3.9)$$

Equation (3.9) can be reduced when $\phi_{ref} = \phi_{sig}$.

$$V_L V_{sig} = \frac{V_{ref} R i_{ph}}{2} + V_{ref} R i_d \sin\left(\omega t - \emptyset_{ref}\right) + V_{ref} R i_{ph} \sin\left(\omega t - \emptyset_{ref}\right) - \frac{V_{ref} R i_{ph}}{2} \cos\left(2\omega t - 2\emptyset_{ref}\right) \quad (3.10)$$

Where V_o is the multiplied modulated and reference signal. When V_o is passed through the low pass filter, the frequency at ω will be filtered out. Therefore the DC equation is given by,

$$V_o = \frac{V_{ref} R i_{ph}}{2} \tag{3.11}$$

As can be seen from (3.11), the DC output is independent of dark current.

3.6 Review of Excess Noise Measurement Systems

The aim of measuring APD noise is to measure the magnitude of the noise power produced by an APD and to help understand of the mechanisms of noise generation in APDs. Several excess noise measurement systems have been published and they will be discussed and compared. The metrics of comparison are,

1. The system signal to noise ratio (SNR), where noise signal is a 1 μA signal current.
2. The minimum primary photocurrent is required.
3. The maximum junction capacitance that the system can accommodate.

There are broadly two methods used in the literature to measure the photocurrent and noise. The first is a direct measurement and secondly phase sensitive methods. Xie *et al*. [61] proposed a direct dc measurement system employs a noise figure meter. The main difficulty with this system is the excess noise factor cannot be accurately measured in the presence of a high dark current. Bulman *et al.* [76] and Ando *et al* [77] described systems based on the phase sensitive detection technology with minimum primary photocurrent 0.63 μA and 6.25 μA, respectively. Lau *et al.* [18] and Green *et al.*[78] reported measurement systems based on the transimpedance amplifier front-end and PSD.

3.6.1 Bulman's System

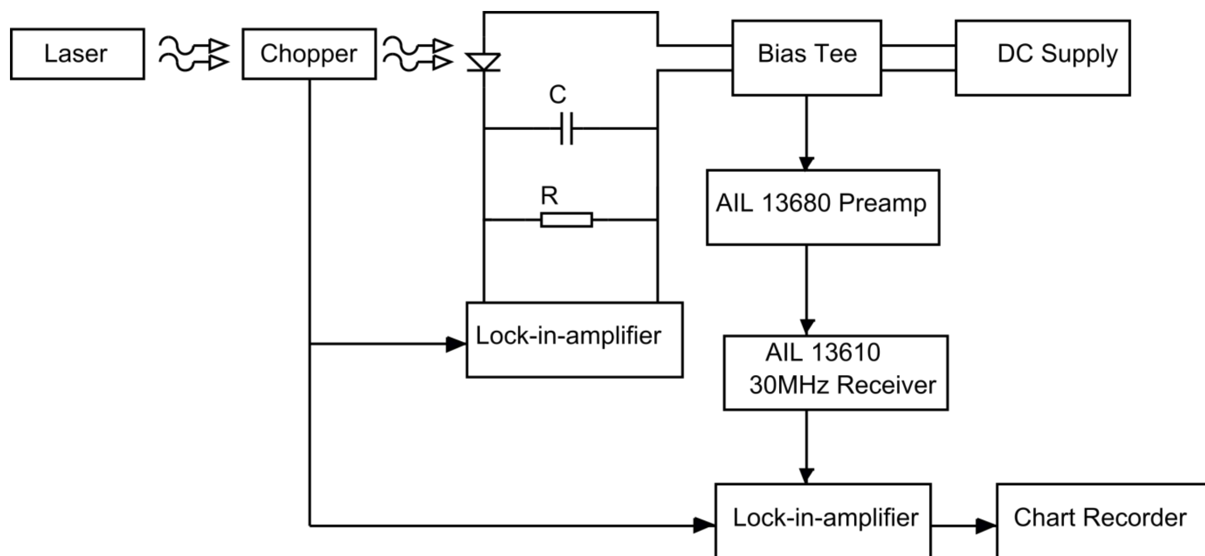

Figure 3.4: Bulman's noise measurement system.

Bulman [76] described a measurement system based on the phase sensitive detection technology shown in Figure 3.4. The photocurrent and excess noise is measured and read out using two lock-in-amplifiers (LIAs) which is synchronised to the chopper frequency. The APD is loaded by the preamplifier through the bias tee which isolates the AC signal from the DC supply. The preamplifier provides gain. The output of the preamplifier is connected to a receiver with centre frequency of 30 MHz and a bandwidth of 1 MHz. The output of the receiver, which is proportional to the noise power, is measured by a lock-in-amplifier. However, this measurement system is not an absolute power value, an initial calibration is done with a pin detector in order to get a baseline which is assumed to be full shot noise. In Bullman's system the DUT can be replaced by a calibrated oscillator to quantify the absolute noise power measured. Bulman reported that the measurement system can be performed with minimum detectable level which equates to full short noise derived from 0.625 µA.

3.6.2 Ando and Kanbe's System

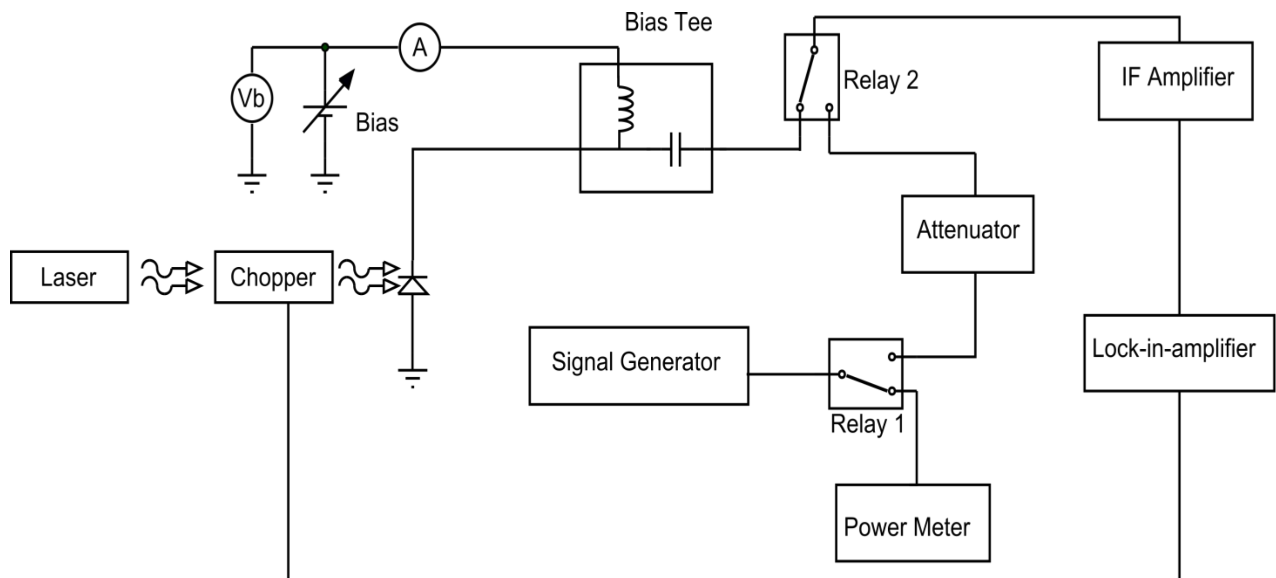

Figure 3.5: Ando and Kanbe's noise measurement system.

Ando and Kanbe [77] reported the noise measurement system shown in Figure 3.5 which employed a phase sensitive detection (PSD) system. The light source with 225 Hz frequency illuminates the APD which is loaded by a 50 Ω resistor. The noise power from the APD is passes through a bias tee to the IF amplifier. The effective noise bandwidth of this measurement system is decided by the IF amplifier which is 1 MHz centred on the 30 MHz. The noise power is extracted by a lock in amplifier. A reference signal source, which is synchronized with a 225 Hz chopper is applied via relay 1 and passes through a calibrated attenuator. The absolute noise power can be determined by comparing the noise power and signal generator power. This noise measurement system can measure the noise power, which is less than -130 dBm within 0.5 dB error. This is equivalent to the shot noise current of 6.25 μA.

3.6.3 Xie's System

The direct dc noise measurement system proposed by Xie [61] is shown in Figure 3.6. The APD is mounted on a micro-strip line and DC voltage is applied by a bias tee. The absolute noise power of the APD is measured by a HP 8970A noise figure meter. Xie's measurement system can operate between the 10 MHz to 1.3 GHz and 4 MHz bandwidth. DC measurements have several disadvantages compare with the PSD measurement system. Firstly, the excess noise factor cannot be accurately measured in the presence of a high dark current. Secondly,

the lowest practically measurable photocurrent is higher than the PSD systems. The measurement system after Xie can measure noise power as low as -194 dBm/Hz at room temperature which corresponds to a shot noise current of 2.5 μA.

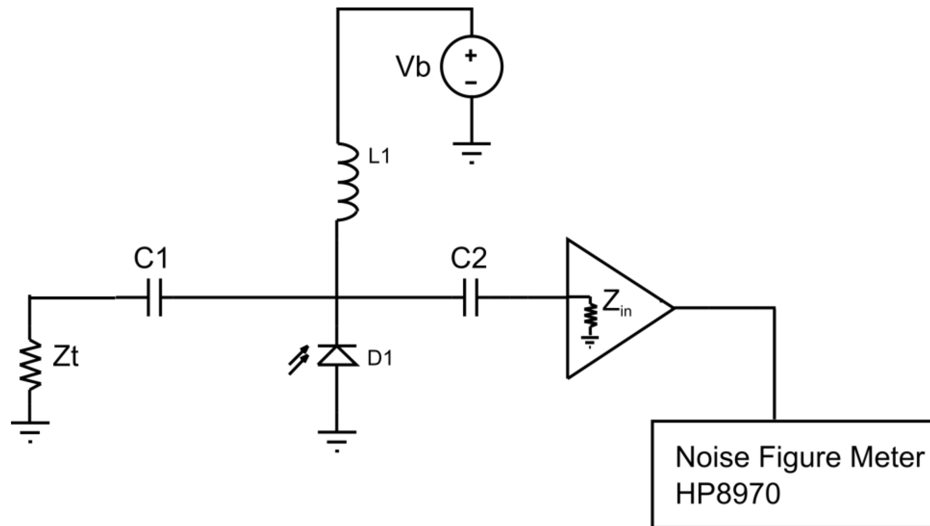

Figure 3.6: Xie's noise measurement system.

3.6.4 Lau's System

The system after Lau [18] reported the system which uses phase sensitive detection and a transimpedance amplifier shown in Figure 3.7. A mechanical chopper is used to modulate light from a laser source at 180 Hz and the light is focused to a small spot (about 10 μm diameter) on the diode. The TIA, which is based on the operantional amplifier AD9631 with a gain of 2200 V/A (unterminated) is used to convert current into a voltage. The output of the TIA is measured using a lock in amplifiier (photocurrent LIA) to determine the photocurrent characteristic. The output of the TIA is also amplified using the commercial low noise amplifier Minicircuits ZFL-500LN+ and through the commercial bandpass filter SBP-10.7 +LC with a bandwidth of 4.2 MHz and centre frequency at 10 MHz. The noise signal is amplified by an additional voltage amplifier before entering a squareing and averaging circuit which acts as a noise power meter. The ouput of the noise power meter is measured using the another lock in amplifier (excess noise LIA). The signal to noise ratio, where noise signal is a 1 μA signal current is -25.7 dB [18] and the shot noise of this system is measured from a photocurrent as low as 0.22 μA.

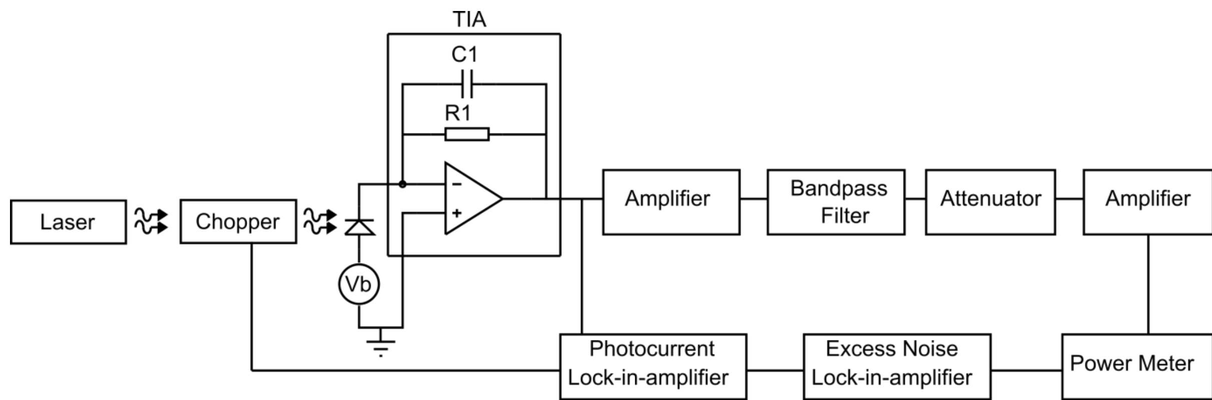

Figure 3.7: Block diagram of the noise measurement system after Lau.

The noise signal to noise ratio (1 µA signal current) of Lau's systems is -25.7 dB [18]. The limit of this system is the lock-in-amplifier can not extract the in-phase signal from the system noise if the primary photocurrent is less than 0.3 µA. In the practical experiment, excess noise factor can be measured precise when a primary photocurrent is obtained at low bias of 0.5 µA to 5 µA depend on the dark current and amount of gain. In order to measure higher multiplicaiton value, the optical illumination power may be reduced. A larger primary photocurrent is required if the lower multiplication value needs to be measured.

Lau [18] has reported that the capacitance tolerated by this noise measurement is lower than all of the other measurement system. The resonance in the frequency response of the TIA depends on the APD junction capacitance, the feedback resistance and open loop gain of the operational amplifier. The circuit gives oscillation when the capacitance is more than 50 pF. This limt was obtained by calibrating the bandwidth of the TIA with capacitance range from 0 pF to 68 pF.

3.6.5 Green's System

A block diagram of the Green's noise measurement system [78] is shown in Figure 3.8 and the overall structure of Green's noise measurement system is similar to Lau's [18], because they use the similar method which includes TIA and PSD. A new design transimpedance amplifier based on the transistor applies a gain of 2200 V/A and converts current into a voltage. The output of the TIA is connected to a bandpass filter which has bandwidth range from 8.9 to 12.7 MHz with a centre frequency of 10.7 MHz. Green [78] has reported that up to 5 nF does not casuse any oscillation. So the capacitance tolerated by his noise measurement is higher than all of the other measurement systems. Furthermore, the minmum primary photocurrent is 1 µA

for this system. The noise signal to noise ratio (1 µA signal current) of Green's system is -25.55 dB while C_j = 1 pF [78]. The SNR falls to -34.75 dB and -55.34 dB while C_j is equal to 1 nF and 5 nF, respectively.

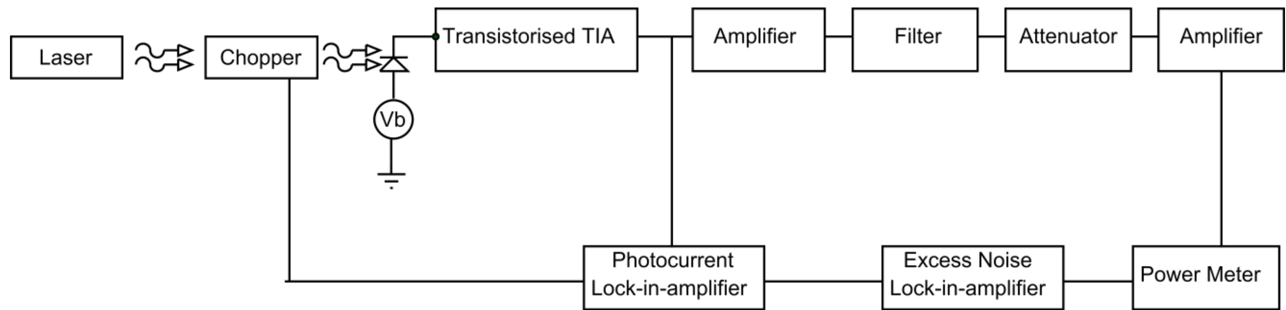

Figure 3.8: Block diagram of the noise measurement system after Green.

3.6.6 Summary of Prior Noise Measurement Systems

Green [78] has review the signal to noise ratio (SNR) of the noise measurement system. The SNR is a very important factor to determine the performance of the each system without considering the bandwidth and the input impedance. Table 3.2 shows the summary of the reviewed noise measurement systems. The minimum required photocurrent of the noise system is 0.22 µA and the highest SNR of the all systems is -25.55 dB. In chapter 4, a very high sensitivity measurement system with very weak photocurrent required will be introduced and discussed.

Author	Min Photocurrent (µA)	SNR (dB) (C_j = 1 pF)	Max C_j (1 pF)
Bulman *et al.*	0.63	-36.72	106
Xie *et al.*	2.5	-31.58	636
Ando *et al.*	6.25	-23.98	106
Lau *et al.*	0.22	-25.7	50
Green *et al.*	1	-25.55	5000

Table 3.2: Compare between different noise measurement systems.

3.7 Conclusion

The first part of this chapter introduced some common experimental methods such as dark forward and reverses current volatge (*IV*) characteristics, capacitance voltage (*CV*) characteristics, and photomultiplicaiton measuerment.

Forward *IV* characteristics are used to find the ideality factor, the saturation current and the series resistance. Reverse *IV* characteristics are used to determine the breakdown voltage and the dark current. *CV* characteristics are used to estimate the doping density, the bulit-in voltage and the layer widths.

The second part of this chapter summarises the published excess noise measurement system in photodiodes. There are three metrics of comparison which are noise signal to noise ratio, maximum photodiode junction capacitance and minimum input photocurrent required. SNR is an excellent method of comparison between different measurement systems with independent system bandwidths and input impendences. Excess noise power factor can be obtained using a low power LED light source if the input photocurrent required is very low.

Chapter 4: Weak Optical Input Power Noise Measurement System

In this chapter, a high sensitivity system for measuring the excess noise associated with the gain in avalanche photodiodes (APDs) is described. This system makes use of a transimpedance amplifier front-end and is based on phase-sensitive detection. This system can reliably measure the excess noise power of devices, even when the photocurrent is low (~10 nA). This figure is more than one order of magnitude better than previously reported systems. This improvement in performance has been achieved by increasing the feedback resistor and reducing the bandwidth. It is the first time that low power density light sources such as LEDs, rather than lasers, have been used to investigate APD noise performance. This measurement system has been used to measure the 1 μm AlInP diode reported in chapter 5 and is in good agreement with the data from Qiao *et al.* [57] with the same structure. The excess noise performance of the $Al_xGa_{1-x}InP$ has been measured using this system and the data is been discussed and analysed in this chapter.

4.1 Introduction

Impact ionisation provides internal current gain in avalanche photodiodes (APDs), which are often used to improve the signal-to-noise ratio (SNR) of an optical receiver in military, medical and communications applications [79]–[81]. The maximum useful gain in APDs is ultimately limited by the excess noise generated by the stochastic nature of the avalanche multiplication process. This noise can degrade the overall SNR of the optical receiver at very high gain values. McIntyre's local noise model [17] showed that the when electrons initiate the ionization process, the ratio of the hole to electron ionization coefficients $k = \beta/\alpha$ is required to be much smaller or more than unity if the APD is to show low noise. Consequently, the measurement of the excess noise in APDs as a function of gain is often used to characterise their performance and to determine the optimum value of gain. It is also often used as a way of inferring the ionization coefficient ratio of the material system. Traditionally, the measurement of excess noise has been undertaken by using a noise figure meter (NFM) [82]–[84]. These suffer from the problem that they need a high photocurrent level relative to the dark current. Not only does this necessitate the use of fairly high power lasers, which often can add noise to the

measurement by way of their relative intensity noise (RIN), the large photocurrents can result in device heating and also distortion of the electric-fields under which the APD operates [19]. In chapter 2, LED and gas lasers are used to perform excess noise measurements but recently the LED has been developed in a wider range of wavelengths than exist for the He-Ne gas lasers and LEDs avoid both of the aforementioned problems provided the excess noise measurements can be done at very low optical powers.

The systems used by Bulman [76] and Ando [77] required minimum primary photocurrents of 0.63 μA and 6.25 μA respectively for their measurements. Lau *et al.* [18] and Green *et al.* [78] reported measurement systems based on a transimpedance amplifier front-end. In [18] the excess noise factor could be measured on APDs with sub-micron depletion region widths, high dark currents, a capacitance of up to approximately 50 pF and required a minimum primary photocurrent of 0.22 μA. The latter system by Green *et al.* [78] was designed to reliably measure the excess noise factor of large area relatively low dark current devices with a capacitance of up to 5 nF and required a minimum primary photocurrent of 1 μA. The signal to noise ratios (SNRs) of the measurement systems have been compared by Green *et al*. [78]. The system described Green *et al.* [18] has the most desirable SNR which is –25.55dB. In the work reported in [18], [76]–[78] phase the photocurrents were modulated and sensitive detection techniques were used as this largely removed the impact of the dark currents of the APD.

In this chapter, a high sensitivity measurement system which is capable of measuring the excess noise of an APD with a photocurrent as low as 10nA is described. The maximum capacitance is restricted to 22 pF but this is well with the range of most practical APDs of interest, with device diameters of up to 400 μm and total depletion widths that exceed 1 μm.

4.2 Noise Measurement System

The principal difference between the system reported here and Lau's system [18] is the change in circuit gain (feedback resistance), the measurement bandwidth and centre frequency. The measured noise power, N consisted of mean avalanche gain M, a photocurrent I_{ph}, and excess noise factor F (M) is,

$$N = 2eI_{ph}B_{eff}(C_p)A^2M^2F(M) \tag{4.1}$$

Where $B_{eff}(C_p)$ represents the effective noise bandwidth (*ENBW*) at the device capacitance C_p and A is the total gain of the whole system. Therefore, increasing the total gain of the whole system is the only way to effectively measure lower photo-generated noise power.

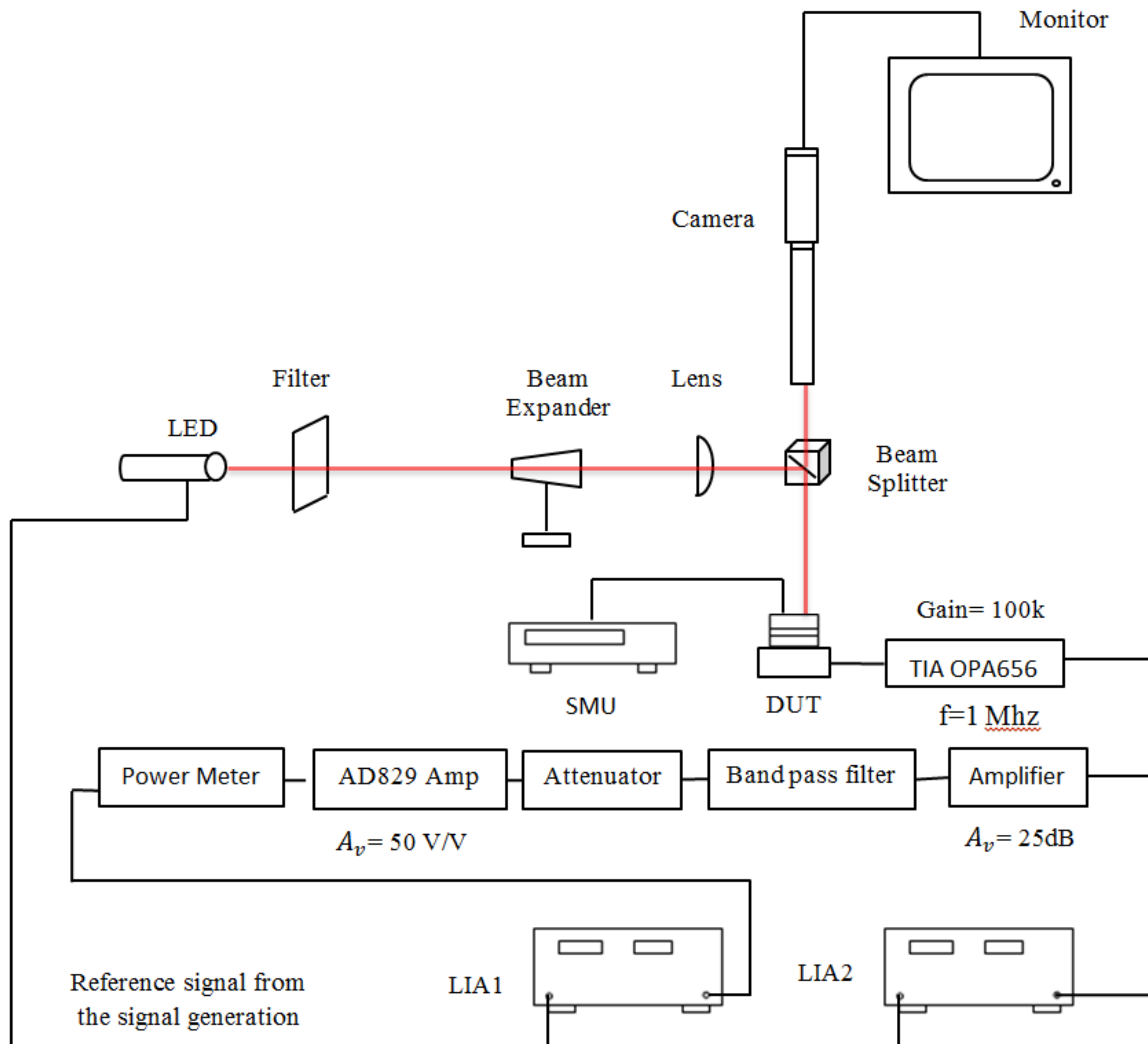

Figure 4.1: A block diagram of the 1 MHz operational amplifier based noise measurement system.

The structure of the measurement system, based on that by Lau *et al* [18], is shown in Figure 4.1. A signal generator and single transistor switching circuit is used to provide power to the LED which provides electrical “chopping” at 180 Hz and thereby provides a reference signal to the lock in amplifiers (LIAs) used in the phase sensitive detection. This becomes essential when the photocurrent being measured starts to decrease to the level of the device dark current. The LED light is focused on the device by using filters and lenses. The spot size of the LED is aproximately 1 mm diameter, therefore the mesa sidewall of the devices are covered by metal to prevent any edge illumination during the measurment.

A Keithley 236 or 237 source measure unit (SMU) provides the reverse bias voltage to the DUT. The transimpendance amplifier (TIA) is shown schematically in Figure 4.2. The TIA, which is based on the operantional amplifier OPA656 with a gain of 100 kV/A (unterminated) is used to convert current into a voltage. Thereafter the voltage is amplified using the Minicircuits ZFL-500LN+ with a terminated gain of 27.98 dB. A precision stepped attenuator, HP 335D, is used to adjust the system gain from 0 dB to 120 dB. The photocurrent signal must first be removed before the noise information can be extracted. A casdcade of single tuned Friend bandpass filters [85] with a bandwidth 0.2 MHz, centred at 1 MHz is used and the circuit diagram is shown in Figure 4.8.

The bandpass filter greatly attenuates the photocurrent, only keeping the information related to noise. The center frequency of 1 MHz is high enough to avoid $1/f$ noise [86]–[89] ,but it is still within the bandwidth of the TIA. The noise signal is amplified by the second voltage amplifier, which is based on the AD829 operational amplifier with a terminated gain of 35.56 dB before entering a squareing and averaging circuit. The squareing and averaging circuit which acts as a noise power meter uses an Analogue Device AD835 analogue multiplier. The circuit diagram for the power meter is shown in Figure 4.11. The ouput of the noise power meter is measured using the first lock in amplifier (LIA1). The photocurrent signal is taken from the an additional output of the TIA and is measured by using the second lock in amplifier (LIA2).

Lau et al [18] designed a transimpedance amplifier by using an Analog Devices AD9631 at 10 MHz with a 2.2 kΩ feedback resistor in order to optimise the bandwidth and gain of the very thin avalanching structures with high capacitances. In more conventional optical communication systems, the SAM-APD has a thick absorption region for providing high quantum efficiency and this reduces the device capacitance. The new system increased the gain of the system from 2.2 kΩ to 100 kΩ and reduces the bandwidth from 10 MHz to 1 MHz in order to obtain higher sensitivity.

4.2.1 A Noise System Design Requirements

The high sensitivity noise measurement system is developed from the existing Lau [18] noise measurment system and the design requirments of this new system are,

- Transimpedance gain of approxinatley 100 kV/A. Outputs for noise power and phtocurrent to be measured using two lock in amplifiers while the primary photocurrent is 10 nA.

- The laser is replaced with an LED as light source.
- – 3 dB bandwidth of the measurement system is at least 1 MHz in order to avoid $1/f$ noise and remain below upper corner frequency of the frontend.
- To be capable of measuring the excess noise on a wide range of samples with a maximum device junction capacitance of 22 pF.
- The SNR of the system is greater than the other reported noise measurment systems.
- The excess noise is measurable even if the dark current level is higher than the photocurrent.

4.3 The Transimpedance Amplifier – Circuit Description

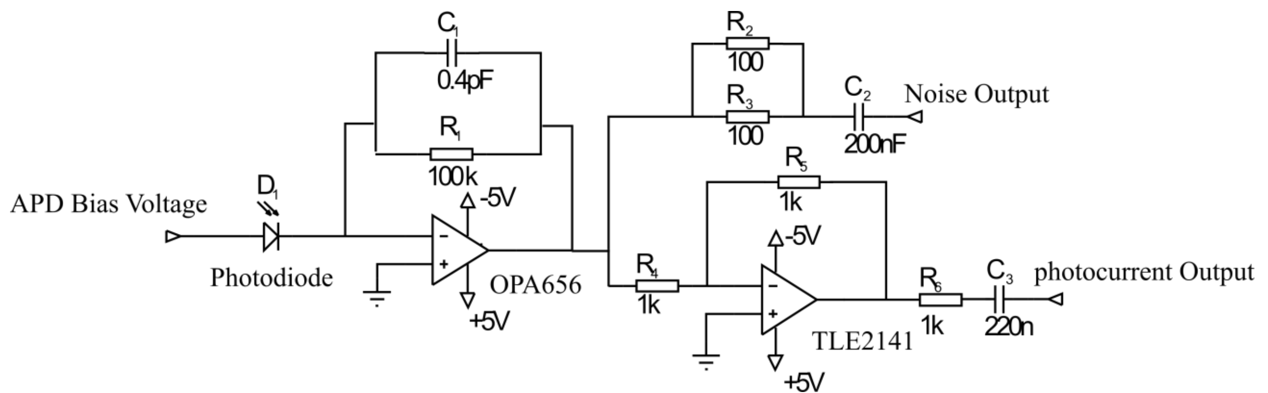

Figure 4.2: A circuit diagram of the transimpedance amplifier based on the OPA656.

The transimpendance amplifier (TIA) is shown schematically in Figure 4.2. The TIA is based on the operational amplifier OPA656 [63] which is a very wideband (500 MHz) unity gain stable voltage feedback amplifier. R_1, C_1, the junction capacitance of the APD (C_j) and the operational amplifier OPA656 gain bandwidth product (GBP) determine the useful bandwidth of the TIA. R_1 is 100 kΩ in order to give a large transimpedance gain while maintaining the required bandwidth of the system. C_1 (0.4 pF) is selected based on the calculation which will be introduced in section 4.3.4 to maximise both transimpedance gain and bandwidth. The shot noise developed by 10 nA is approaching the limit because of the background noise and the shot noise is only 56.6 fA/$\sqrt{\text{Hz}}$. Since the bandwidth of this measurement system is 0.2 MHz, Noise currents as low as 25 pA_{RMS} yield a unity signal to noise ratio. Decoupling capacitors on the operational amplifiers are not shown in Figure 4.2.

4.3.1 TIA Noise Performance

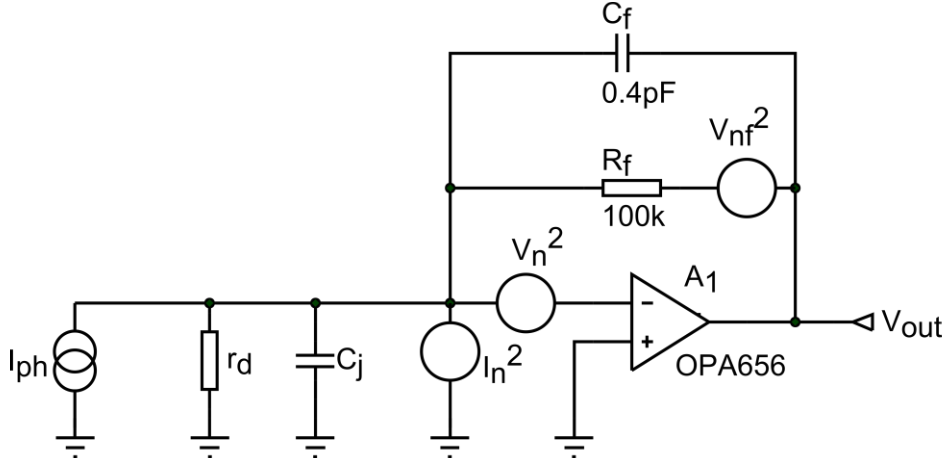

Figure 4.3: Noise model of the transimpedance amplifier shows feedback resistance thermal noise voltage, V_{nf} and input op-amp input current (I_n) and input voltage (V_n) noise equivalent source. I_{ph}, r_d and C_j represent the equivalent circuit of the APD.

The noise performance of the transimpedance amplifier can be analysed using the standard opamp noise model which has an equivalent noise current source, I_n , and an equivalent noise voltage source, V_n. The equivalent noise model of the TIA is shown in Figure 4.3. As can be seen in Figure 4.3, the input noise current source, i_n is parallel with the phtocurrent current source, I_{ph}. Therefore, it shows the transfer function V_o/i_n and transfer function V_o/I_{ph} are same.

The output noise voltage from the photocurrent source, is given by:

$$\frac{V_o}{I_{ph}} = G(f) = -\frac{A_o r_d R_f}{(A_o r_d + R_f + r_d) + s(k + \tau_o r_d + \tau_o R_f + A_o C_f R_f r_d) + s^2 \tau_o k} \quad (4.2)$$

Where $k = C_j r_d R_f + C_f r_d R_f$, R_f is the feedback resistance, C_f is the feedback resistance, r_d and C_j represents the equivalent circuit of the APD, shunt resistance and junction capacitance, respectively. A_o is the dc open loop gain of the op-amp and τ_o is the open loop time constant of the op-amp.

The output noise voltage from the input noise voltage from the op-amp, is given by:

$$\frac{V_o}{V_n} = -\frac{A_o(r_d + R_f) + skA_o}{(A_o r_d + R_f + r_d) + s(k + \tau_o r_d + \tau_o R_f + A_o C_f R_f r_d) + s^2 \tau_o k} \quad (4.3)$$

The output noise voltage due to the thermal noise of the feedback resistance is,

$$\frac{V_o}{V_{nf}} = -\frac{A_o r_d}{(A_o r_d + R_f + r_d) + s(k + \tau_o r_d + \tau_o R_f + A_o C_f R_f r_d) + s^2 \tau_o k} \quad (4.4)$$

The total noise voltage at the output from the input noise current, I_n , the input voltage noise, V_n and feedback thermal noise, V_{nf} is,

$$V_{on}^2 = \frac{I_n^2(A_o r_d R_f)^2 + V_n^2[(A_o(r_d + R_f))^2 + (\omega k A_o)^2] + V_{nf}^2(A_o r_d)^2}{[(A_o r_d + R_f + r_d) - w^2 \tau_o k]^2 + \omega^2(k + \tau_o r_d + \tau_o R_f + A_o C_f R_f r_d)^2} \tag{4.5}$$

The details of the noise analysis are given in Appendix C. In order to make comparsions with other noise measurement systems, the signal to noise ratio for the TIA is given by:

$$\frac{S}{N} = \frac{\int_a^b 2eI_{ph}|G(f)|^2 df}{\int_a^b \overline{V_{on}^2}(f)df} \tag{4.6}$$

Where I_{ph} is the stimulated photocurrent, $G(f)$ is the transfer function given by (4.2), V_{on} is the total noise voltage of the TIA given by (4.5) and a and b are the start and end of measured noise power frequency range.

Figure 4.4 shows the noise signal to noise ratio (NSNR) as a function of frequency for different values of C_j. NSNR is a useful metric to permit comparisons between different measurment systems independent of the bandwidth and input capacitance. The NSNR of this TIA is approximately 2.62 dB while C_j = 1 pF and falls to -14.624 dB at C_j = 68 pF for shot noise derrived from 1 μA signal current which is based on the measured on the SMU. This is an improvement of approximately 23 dB over the other noise measurment systems which were introduced in chapter 3. The SNR of this TIA is -20 dB while C_j = 1 pF, and the photocurrent is 10 nA.

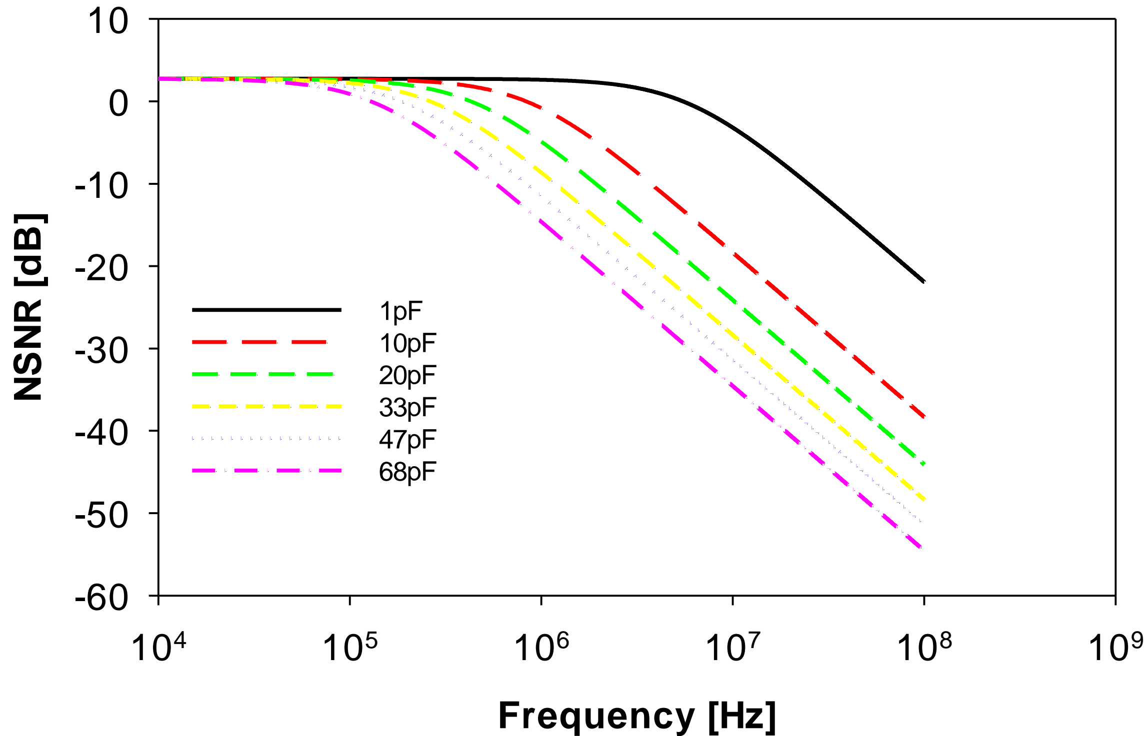

Figure 4.4: The analytical model noise signal to noise ratio (NSNR) against frequency with different value of the C_j from 1 pF to 68 pF for a 1 μA signal current.

4.3.2 TIA Noise Performance using SPICE

The noise performance of the transimpedance amplifier was analysed using a SPICE model in order to check that the calacultation results were consisent with simulation. Figure 4.5 shows the compasion of the calculation and simulation transfer function, V_o/V_{nf}, V_o/V_n and V_o/I_{ph} while C_j = 10 pF. Good agreement is observed on all noise transfer functions.

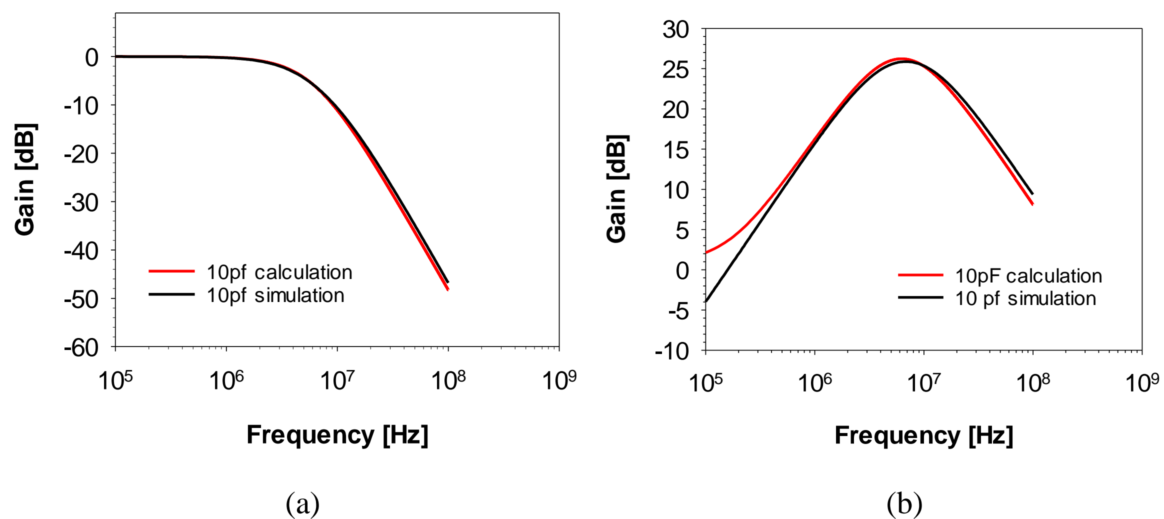

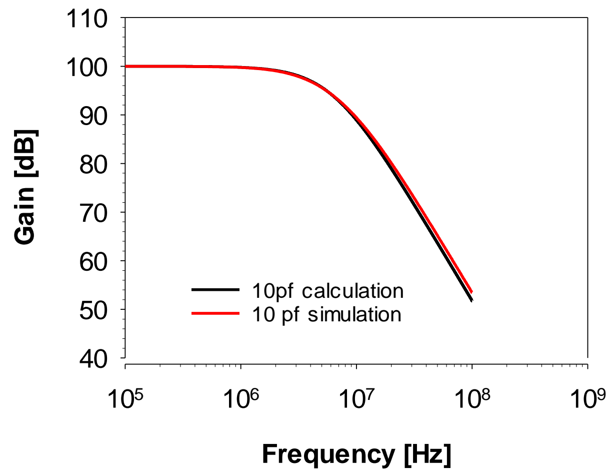

(c)

Figure 4.5: (a) Results of the feedback noise voltage transfer function, V_o/V_{nf} due to the feedback resistance. (b) Results of the input votlage transfer function, V_o/V_n. (c) Results of the input noise current transfer function V_o/I_{ph}.

4.3.3 Characterisation of the Transimpedance Amplifier Frequency Response

Characterisation of the transimpedance amplifier can be accomplished by using a network analyser. An HP4396B VNA was used in this work. The test setup is shown in Figure 4.6. The purpose of the circuit configuration, which consists of a chain of resistors is to convert the voltage signal output from the VNA RF source into a current, before it passes into the input of the TIA. C_j represents the junction capacitance of a APD and a range of 1206 or 0805 chip capacitors are used to provide appropriate values.

Using the test circuit of Figure 4.6, the frequency response of the TIA is measured as a function of increasing APD capacitance, C_j. The result in the range C_j = 0 to 68 pF is shown in Figure 4.7. This figure shows that there is considerable dependence of gain on C_j at frequencies above 1 MHz. The value of the feedback capacitance, C_f = 0.4 pF is chosen empirically because it provides acceptable gain peaking over the range of values of the C_j between 0 pF and 68 pF. The response for different values of C_j (which represents the input junction capacitance of the APD) can be used to correct for the effects of the different gain peaking for different input junction capacitance. This allows APDs with different junction capacitance to be compared. The details are discussed in the section 4.4.

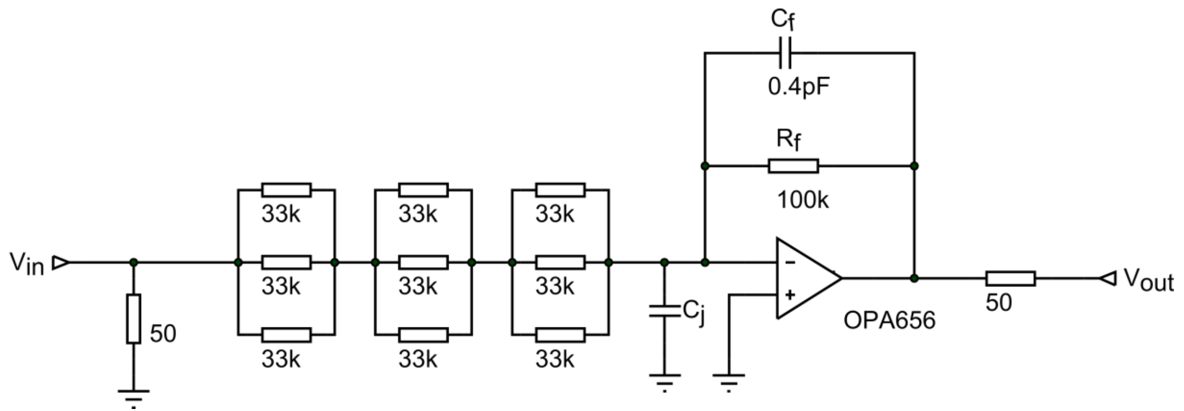

Figure 4.6: APD approximation circuit used for measurement of TIA frequency response.

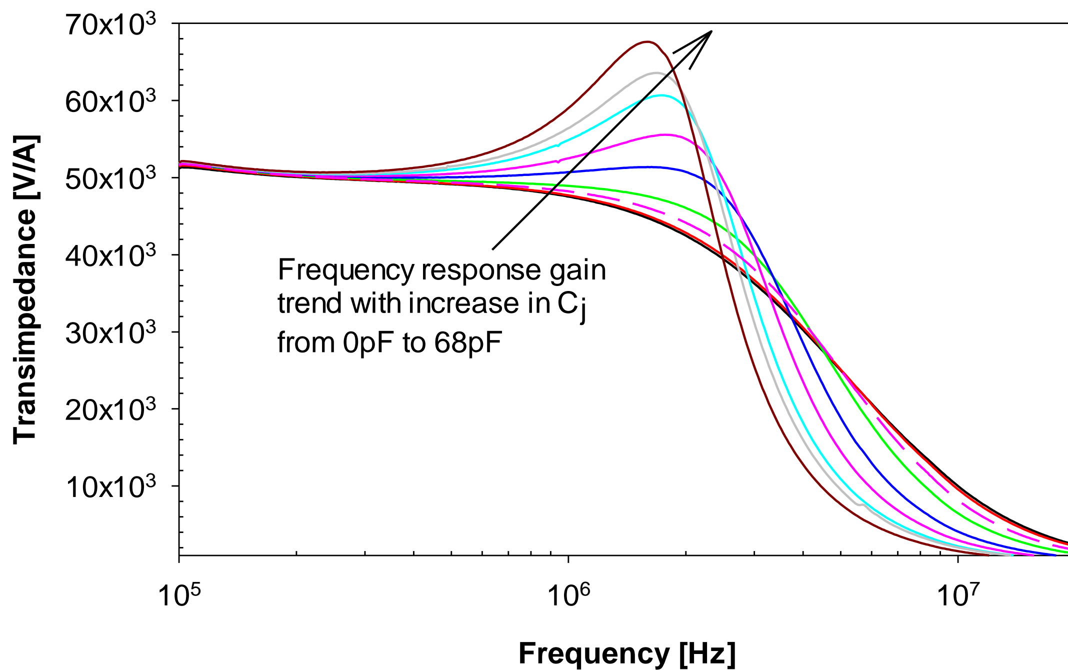

Figure 4.7: Frequency response of TIA with input capacitance C_j from 0 pF to 68 pF.

4.3.4 Selection of a suitable op-amp

An op-amp needs to be chosen in order to evaluate the SNR of the transimpedance amplifier (TIA). Ideally, the suitable amplifier will need the following performance.

1. A low noise op-amp should generate both low current noise, i_n and voltage noise, v_n. The input voltage noise, v_n of the op-amp in the 1 MHz frequency dominates in this application according to equation (4.5).

2. Op-amps designed for high gain and high frequency applications should have a large gain bandwidth product (GBP) in order to obtain a higher cut-off frequency this is expressed by (4.7).

The cut-off frequency of the transimpedance amplifier circuit is given by:

$$f_{cut-off} = \sqrt{\frac{GBP}{2\pi R_f C_j}} \tag{4.7}$$

Where R_f is the feedback resistance and C_j represents the expected diode capacitance. The relationship between the feedback components R_f and C_f is,

$$\frac{1}{2\pi R_f C_f} = \sqrt{\frac{GBP}{4\pi R_f C_j}} \tag{4.8}$$

Where C_f is the feedback capacitance. Suitable amplifiers are summarised in table 4.1.

	v_n (nV/Hz$^{1/2}$)	i_n (pA/Hz$^{1/2}$)	GBP (MHz)
AD9631[65]	7	2.5	175
OPA656 [63]	7	0.0013	230
OPA604 [90]	10	0.004	20
MAX4100 [91]	8	0.8	500

Table 4.1: Specifications of the op-amp.

It is necessary to choose a suitable op-amp to obtain a low noise system and high cut-off frequency. Although the MAX4100 has the highest GBP, the voltage and current noise is higher than OPA656. The dominant noise is input voltage noise, v_n of the op-amp and the OPA656 has the lowest the voltage and current noise. Noise property is the primary driver for the choice of these opamp in order to get higher signal to noise ratio. OPA656 is chosen in the noise measurement system. The GBP of the OPA656 is 230 MHz and (4.7) estimates the cut-off frequency of the TIA is 6.05 MHz when the R_f and C_j is 100 kΩ and 10 pF, respectively. Therefore, the feedback capacitance can be calculated (0.4 pF). However, the C_f will reduce to 0.1 pF when the R_f increases from 100 kΩ to 1 MΩ. It is very difficult to obtain C_f = 0.1 pF with any accuracy because this is similar in magnitude to the parasitic capacitance from the feedback resistor and PCB trace.

4.4 Bandpass Filter and Effective Noise BandWidth (ENBW)

The effective noise bandwidth (ENBW) of the measurement system is used to correct for the different input junction capacitance of APD samples. It provides a relationship between ENBW and junction capacitance. The bandpass filter in Figure 4.1 has a bandwidth of 0.2 MHz, and a centre frequency of 1 MHz which is within the bandwidth of the TIA and it is high enough to avoid 1/*f* noise. The bandpss filter is designed by using cascade of single tuned Friend bandpass filters [85]. The circuit diagram is shown in Figure 4.8. The frequency response of the combination of the TIA and bandpass filter as a function of input junction capacitance is shown in Fig.4.8. and this data can be used to compute the ENBW of the system.

The ENBW of the measurement system is given by:

$$B = \frac{1}{G_0^2}\int_{f_1}^{f_2} |G(f)|^2 df \qquad (4.9)$$

Where $G(f)$ is the voltage gain of the system. G_o is the gain at the centre frequency while C_j = 0 pF. f_1 and f_2 are the start and stop frequency over which there is significant voltage gain.

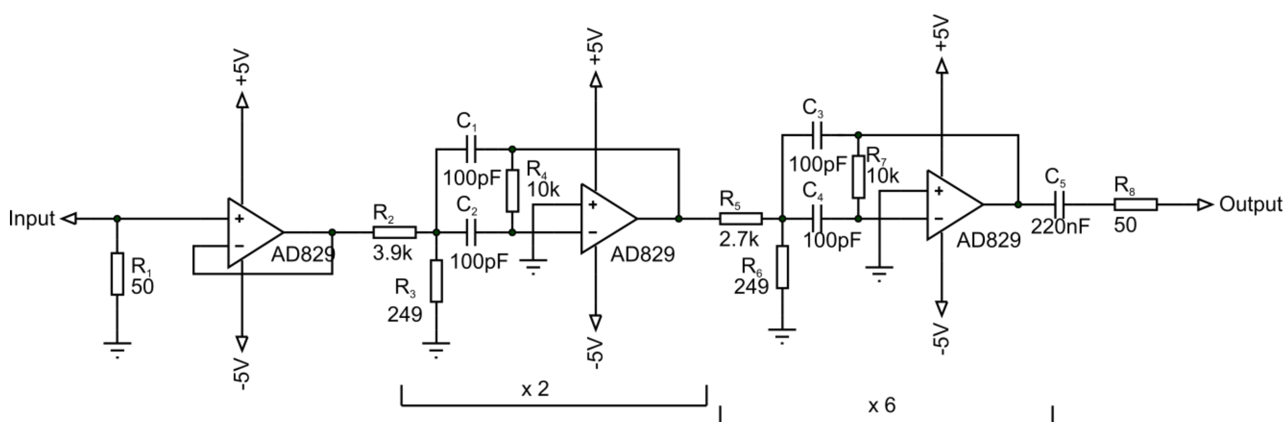

Figure 4.8: A circuit diagram of the bandpass filter with a bandwidth 0.2 MHz, centred at 1 MHz.

As can be seen in Figure 4.9, the gain peaking tends to increase with C_j. Figure 4.7 suggests that the avalanche noise should be measured at a lower frequency where passband gain is almost constant with C_j. However this risks encountering 1/*f* noise. The ENBW is calculated for different values of C_j from 0 pF to 68 pF using (4.9) and it is plotted in Figure 4.10. The ENBW can be expressed as the third order polynomial and is given by,

$$B(C_j) = -6.3\times10^{-3} C_j^3 + 3.31\times C_j^2 + 4.61\times10^2 C_j + 92240 \qquad (4.10)$$

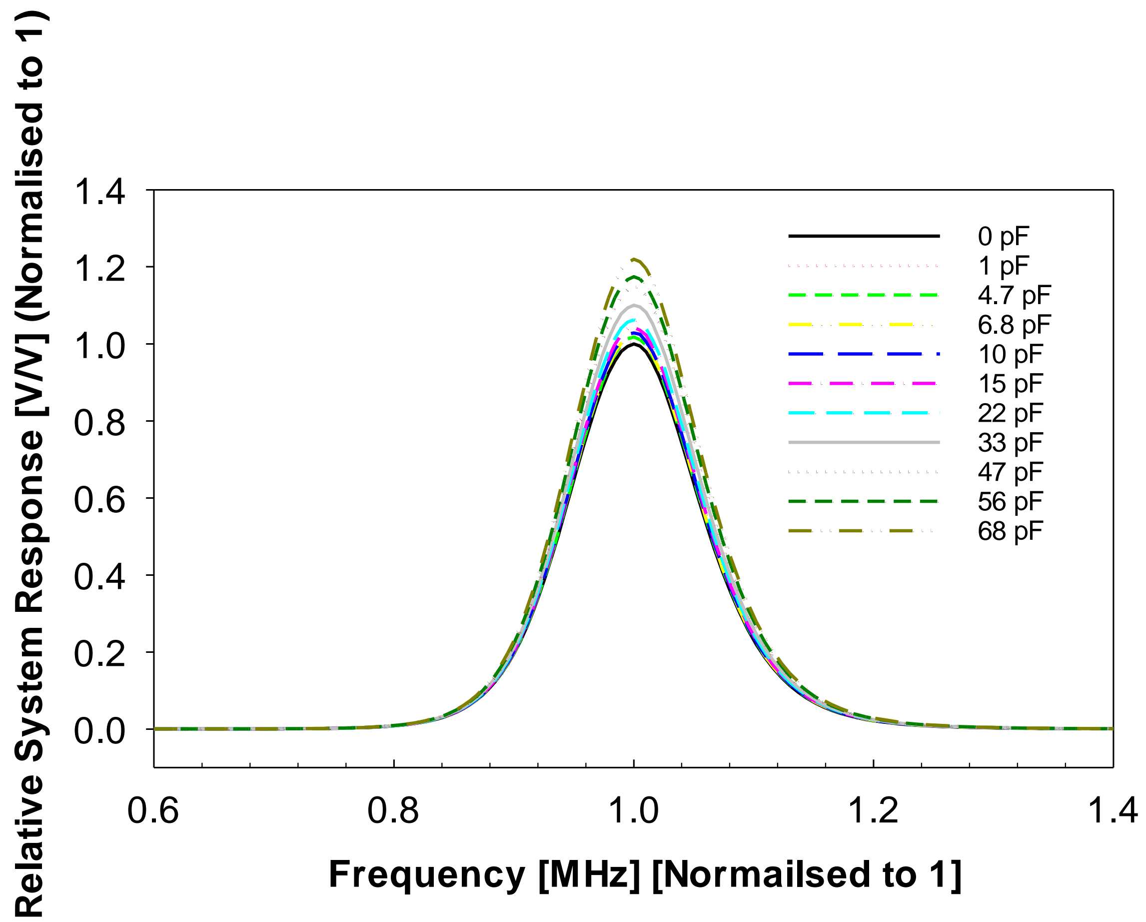

Figure 4.9: Frequency response of transimpedance and bandpass as a function of input junction capacitance, C_j.

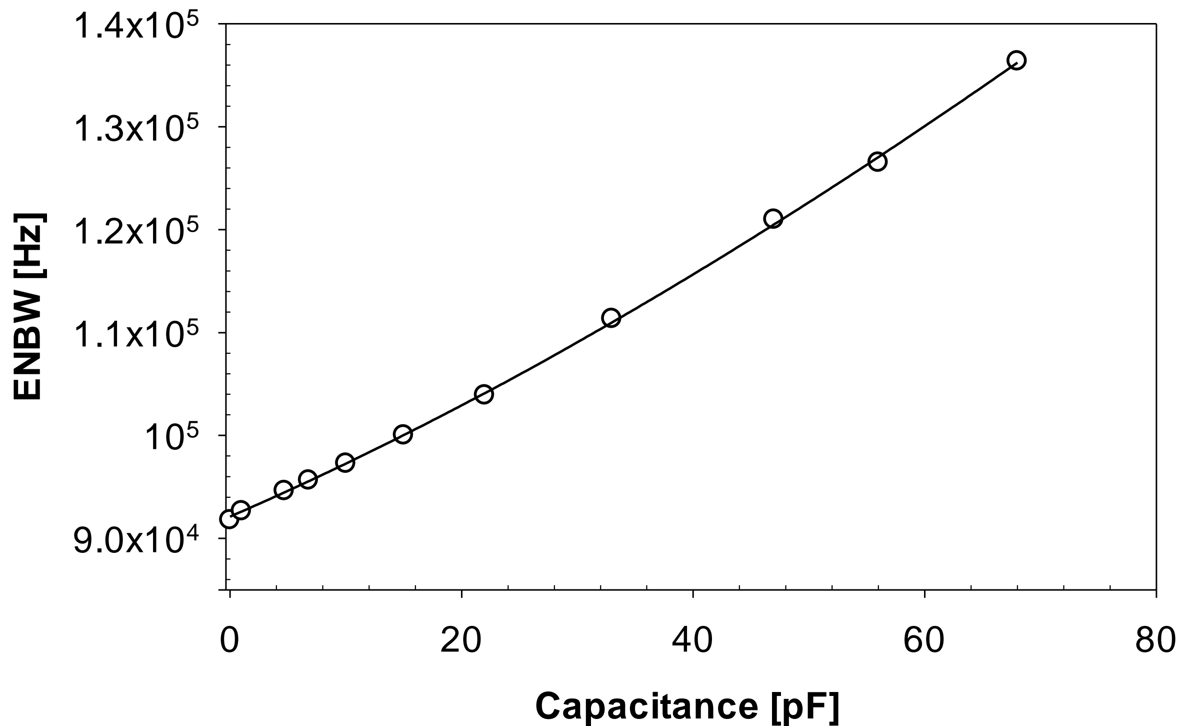

Figure 4.10: The effective noise bandwidth of the TIA as a function of APD junction capacitance. Open circles represent calculated results using (4.10) and the solid line third order fitting results, respectively.

4.5 Noise Power Meter

The noise power meter, developed by Ng [58], is based on the Analog Devices AD835 wide band analogue multiplier. The circuit diagram of the noise power meter is shown in Figure 4.11, where the structure of the AD835 is shown in a grey block diagram form. The non-inverting inputs of the AD835 multiplier are connected together in parallel, so the output voltage of the multiplier is proportional to the square of the input signal. The DC offest is lessened by trimming the offset null of the TLP71 and finally removed by AC coupling the power meter output to the LIA. The output of the AD835 multiplier is applied to a first order low pass filter, C_1 and R_4, with a cutoff frequency 1.59 kHz in order to obtain the mean squared value. The TL071 forms a non-inverting amplifier which amplifies the mean square value with a voltage gain of 16 providing a suitable level to drive the LIA.

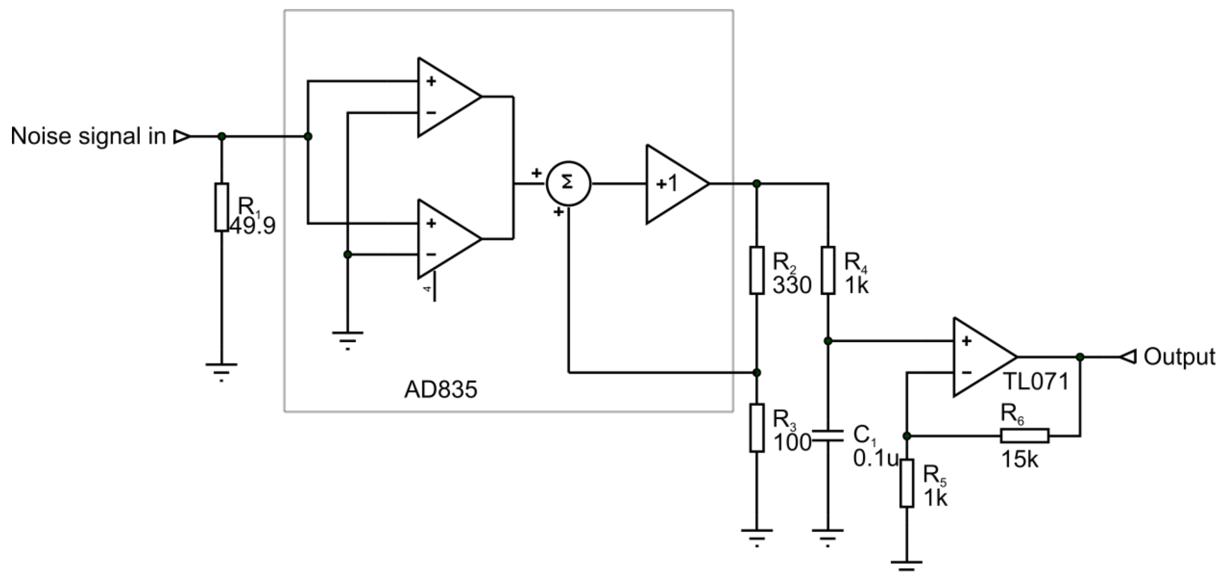

Figure 4.11: Circuit diagram of the noise power meter based on the AD835.

The transfer function for the multipiler circuit is,

$$V_o = 4.68V_i^2 + 0.012V_i + 0.465 \qquad (4.11)$$

Where V_o is the mean squared output voltage and V_i is the RMS input voltage.

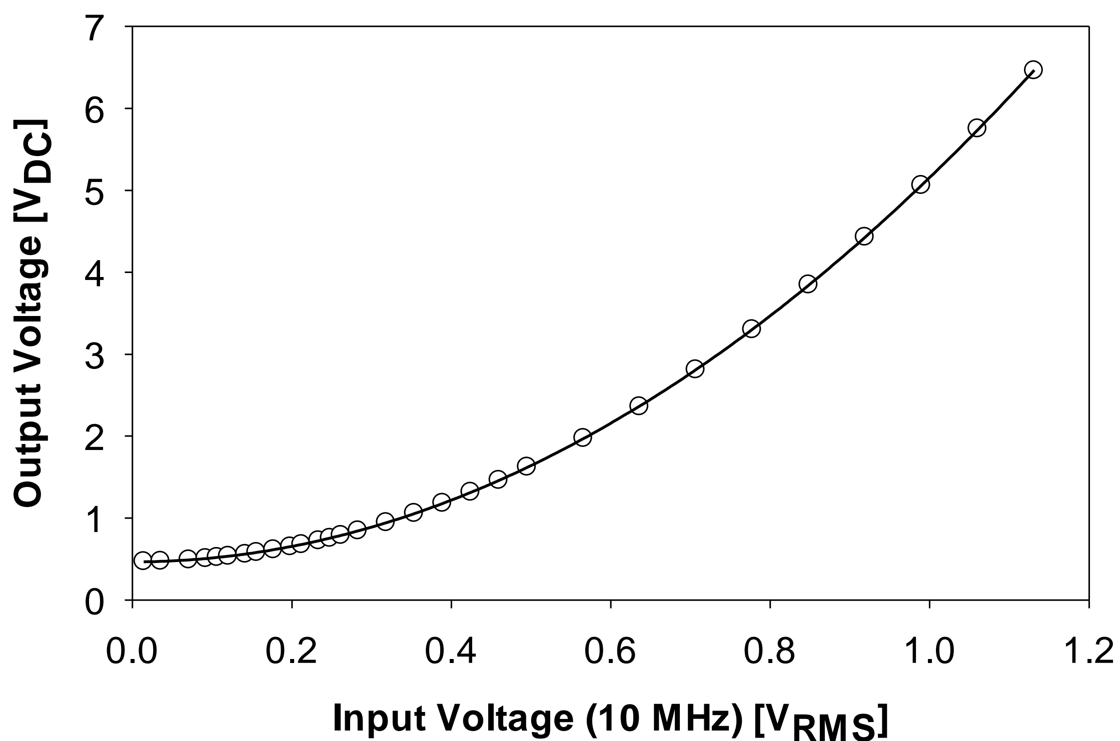

Figure 4.12: Measured power meter transfer characteristic. This data is generated using a sinusoidal test signal to drive the power meter.

4.6 System Testing

The noise measurment system is calibrated by measuing the noise power as function of photocurrent in a silicon commerical PIN photodiode (type BPX65) with a known junction capacitance at a fixed bias voltage before determine excess noise factor. The BPX65 has a unity gain ($M = 1$) so that the photodiode produces only shot noise and excess noise factor is equal to 1. The graph of measured noise power as function of photocurrent is shown in Figure 4.13. The relationship between measured noise power and excess noise factor is given by (4.1). The ratio of the noise power to photocurrent is given by,

$$\frac{N_{si}}{I_{ph}} = 2eB_{eff}(C_{si})A^2 = a \tag{4.12}$$

Where $B_{eff}(C_{si})$ is the effective noise bandwidth of calibrating Si photodiode (C_{si}) and A is the total gain of the system.

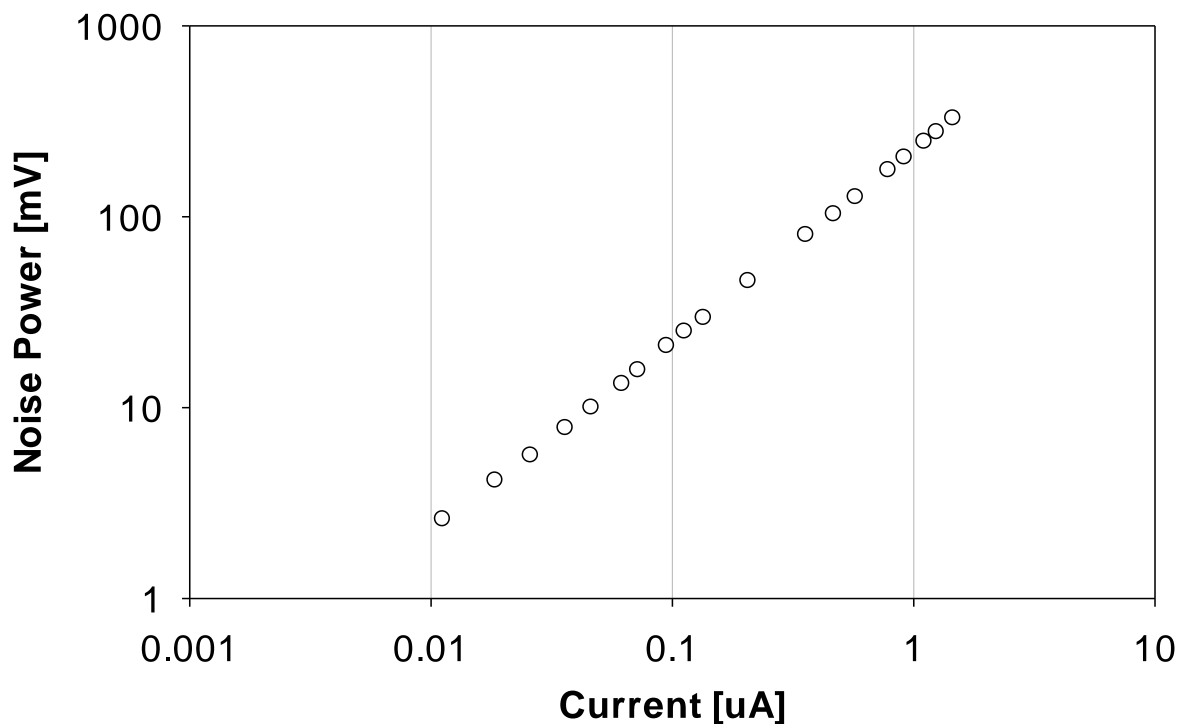

Figure 4.13: Noise power versus photocurrent of a silicon commercial device (BPX65).

Figure 4.13 shows the photocurrent generated noise power is measureable while the photocurrent is approximately 10 nA and the ratio of the noise power to photocurrent is shown to be linear and proportional. The slope is unity which is expected given (4.12) and suggests that the great majority of the device's noise enters the measurment system. The noise power of the device under test (DUT) is given by,

$$N_{DUT} = 2eIB_{eff}(C_{DUT})A^2MF(M) \quad (4.13)$$

Where $B_{eff}(C_{DUT})$ is the effective noise bandwidth at the device under test's capacitance, M is the corresponding multiplication and I is the multiplied photocurrent, $I = I_{ph}M$. Combining (4.12) and (4.13), the excess noise factor is given by,

$$F(M) = \frac{N_{DUT}}{aMI} \cdot \frac{B_{eff}(C_{si})}{B_{eff}(C_{DUT})} \quad (4.14)$$

where I is the multiplied photocurrent, $B_{eff}(C_{si})$ is the effective noise bandwidth of calibrating Si photodiode and $B_{eff}(C_{DUT})$ is the effective noise bandwidth at the device under test's capacitance. To ensure the dark current does not affect the measurements especially at high gains, optical sources were modulated and the resulting photocurrents and noise power were measured using lock in amplifiers.

4.6.1 Dark current Limit

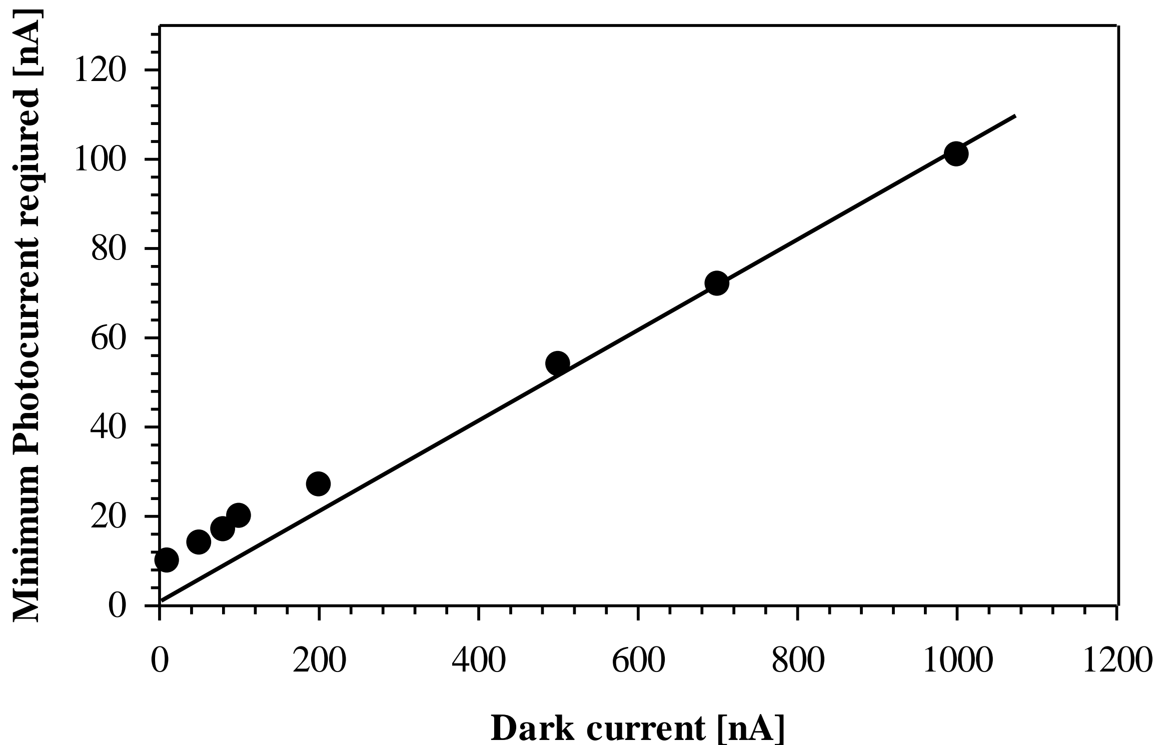

Figure 4.14: Minimum photocurrent vs dark current by using commercial silicon device BPX65.

Figure 4.14 shows the measurement of the minimum photocurrent required for a BPX65 to obtain a measurable noise power using this circuit. The photo current is obtained by a modulated LED and the 'dark' current is provided by varying the illumination of the

photodiode with broad band dc visible light. The noise power can be reliably measured even when the photocurrent is significantly less than the dark current. The minimum photocurrent required versus dark current has a linear relationship at higher dark current values, implying that the dark current is dominating the NSNR of the system across this range of values. The system noise however becomes relatively more significant at low photocurrents, which is why it is difficult to measure excess noise when the un-multiplied photocurrent is below 10 nA.

4.6.2 Series resistance limit

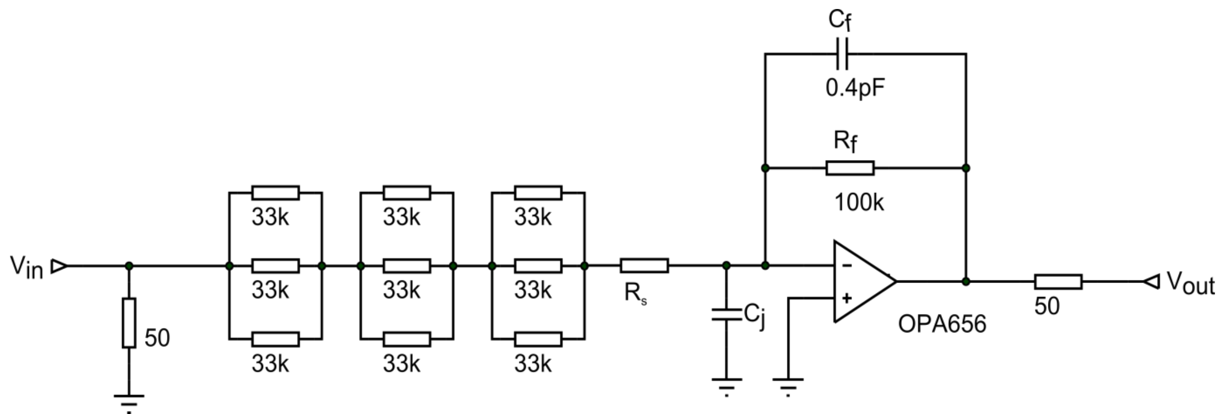

Figure 4.15: APD approximation circuit used for measurement of TIA frequency response with series resistance R_s.

Ong [92] reported that in the Lau's system which was described in chapter 2, the excess noise factor can be artificially reduced as compared to the noise factor obtained a low series resistance device. It is important to know the limitation of the series resistance in the new noise measurement system. Using the test circuit of Figure 4.15, the frequency response of the TIA is measured as function of increasing APD series resistance, R_s when the APD capacitance is equal to 0 pF, 4.7 pF and 15 pF. The result in the range $R_s = 0$ to 10 kΩ is shown in Figure 4.16. In Figure 4.16, the effect of series resistance can be ignored when the series resistance is less than 1 kΩ. The gain at the output of the TIA reduces when the series resistance is equal to 10 kΩ.

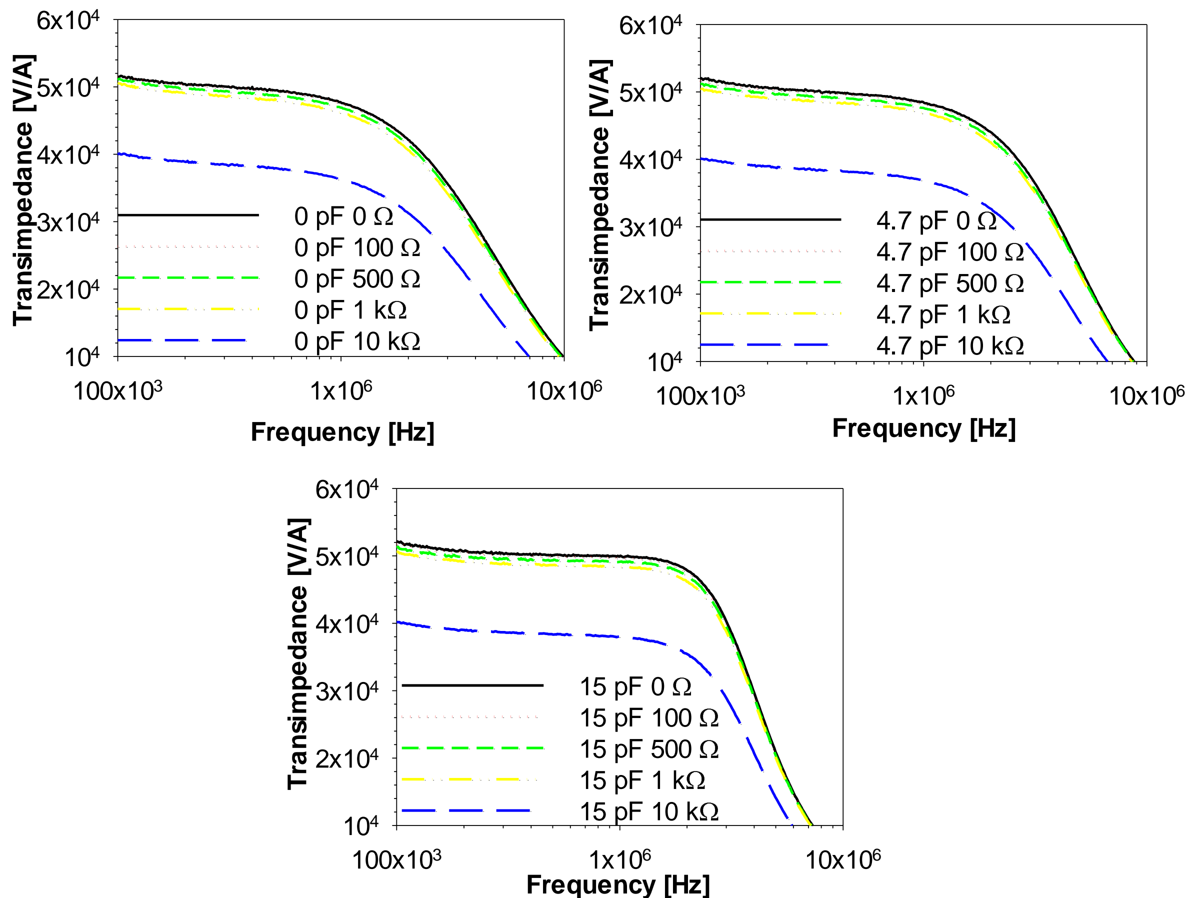

Figure 4.16: Comparison of frequency response of the front end TIA with different combinations of series resistance and input capacitance before passing through the bandpass filter.

The frequency response of the combination of the TIA and bandpass filter is shown in Figure 4.17. The reduction of the output of the bandpass filter in the range from 0.8 - 1.2 MHz is more significant when the series resistance is larger than 1 kΩ. Therefore, the noise power at the output of the bandpass filter with a larger series resistance device is lower than the noise power measured with a very low series resistance device. The excess nosie factor calculated by (4.14) will be reduce due to the noise power is decreased. In this system, the excess noise factor can be measured accurately when the series resistance is less than the 1 kΩ.

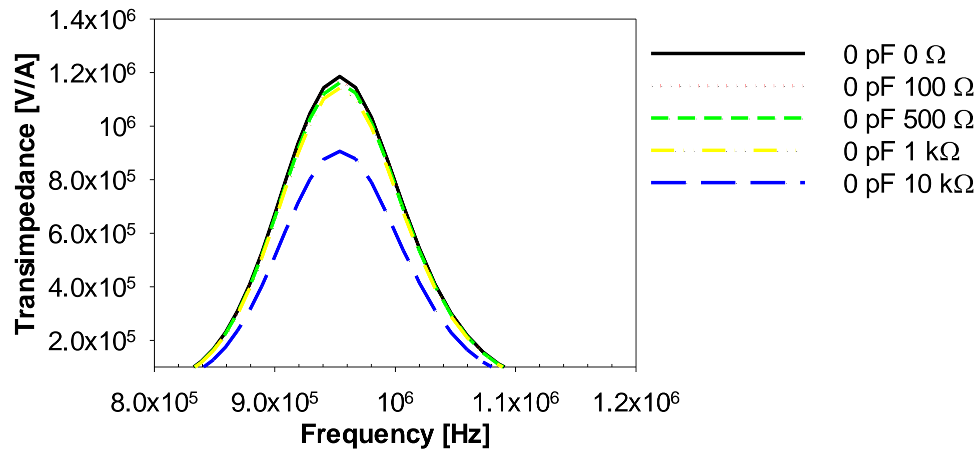

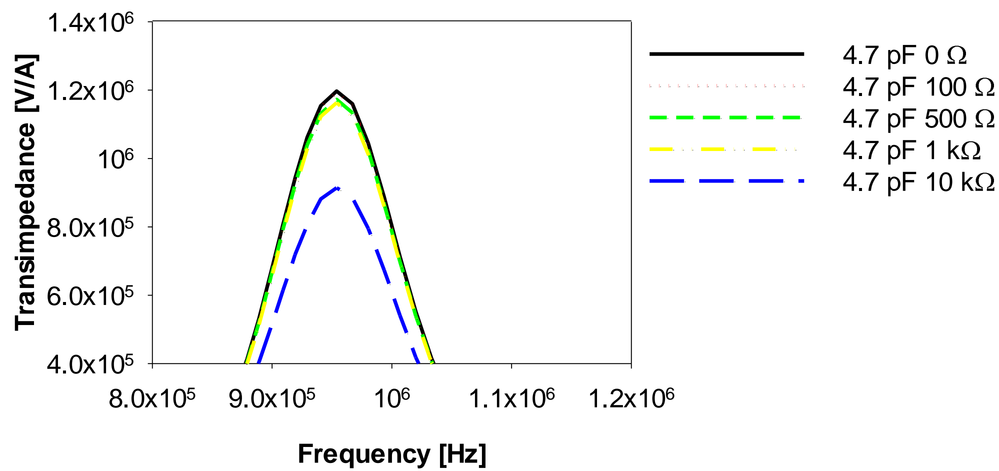

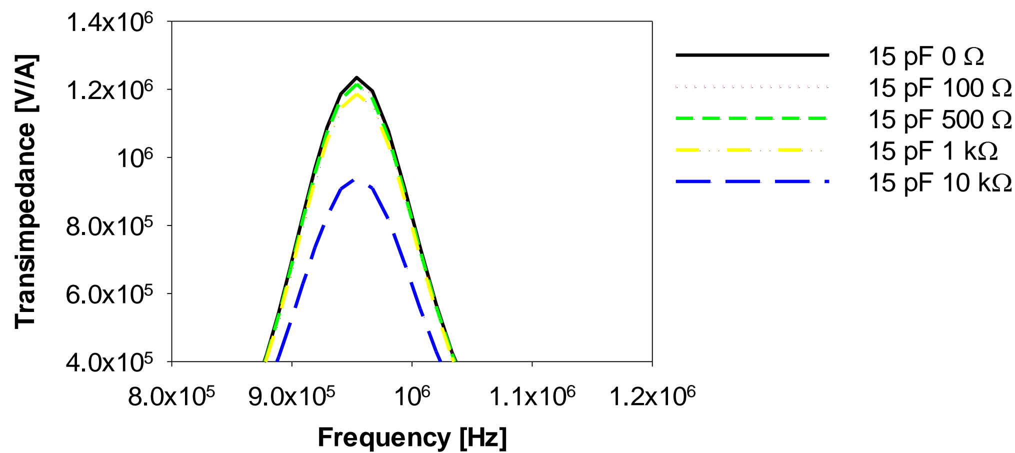

Figure 4.17: Comparison of frequency response of the front end TIA with different combinations of series resistance and input capacitance after leaving the bandpass filter.

4.7 Measurement Results

Multiplication and avalanche noise measurements have been measured on a series of homo-junction $Al_xGa_{1-x}InP$ PIN diodes with different Al fraction x from 0% to 100% with nominal *i* region widths, *w*, of 1.0 µm using the new noise measurement system presented in this thesis. Chapter 2 documents some problems with semiconductor lasers that mean only gas lasers and, in this thesis for the first time at Sheffield, LEDs have been used to perform excess noise measurements. Several different wavelengths of light are chosen in order to obtain the excess noise factors of the pure and mixed injection. It is difficult to find a low noise laser of the correct wavelength to match the requirements of this material. In this work LEDs and lasers are used to provide optical excitation. The system can reliably measure the excess noise even when the optical excitation power density is very low.

4.7.1 Layer Details

The set of diodes used in this work includes the four homo-junction PINs structure. Table 4.2 shows the structure of the layers and it is as follows: a doped GaAs buffer layer followed by a 0.3 µm doped AlInP cladding region, the un-doped AlGaInP layer, a 1 µm doped top AlGaInP cladding layer and finally a thin 0.05 µm heavily doped contact layer to facilitate top ohmic contact formation.

Wafer	Al fraction	Structure	Top/bottom cladding thickness (µm)	Width (µm)
MR2812	100	PIN	1/0.3	1
MR3917	78	PIN	1/0.3	0.94
MR3916	64	PIN	1/0.3	0.96
MR3919	61	PIN	1/0.3	1
MR3920	47	PIN	1/0.3	0.93
MR3921	31	PIN	1/0.3	0.99
MR3925	0	PIN	1/0.3	0.97

Table 4.2: The structure of the $Al_xGa_{1-x}InP$ diodes.

4.7.2 CV Measurement

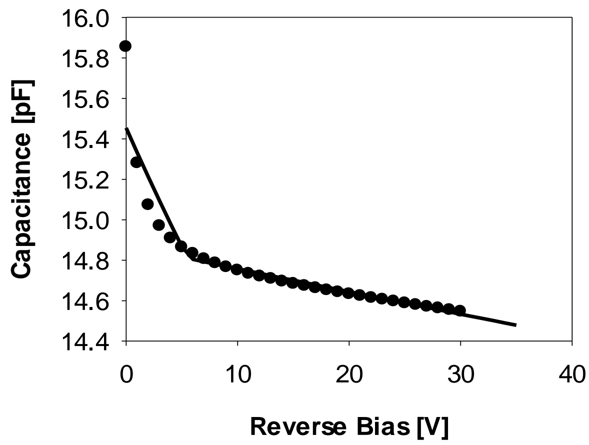

Figure 4.18 (a)

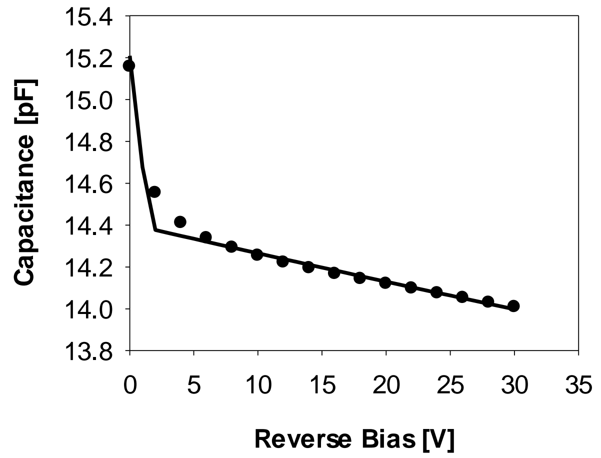

Figure 4.18 (b)

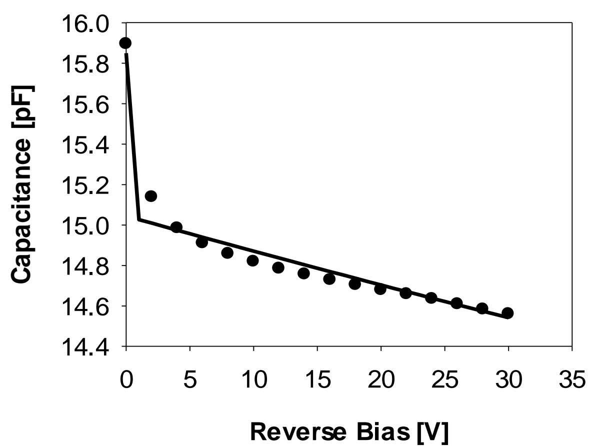

Figure 4.18 (c)

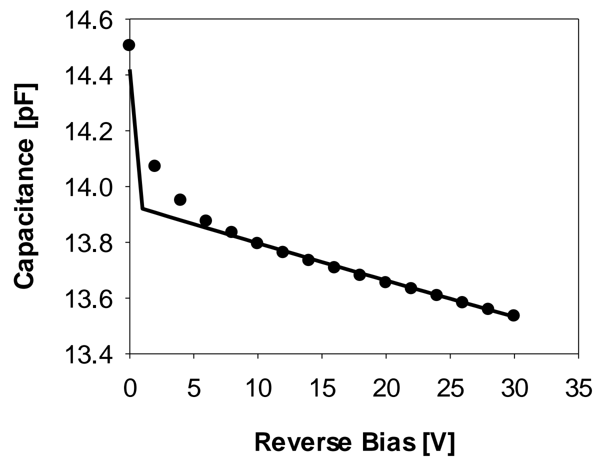

Figure 4.18 (d)

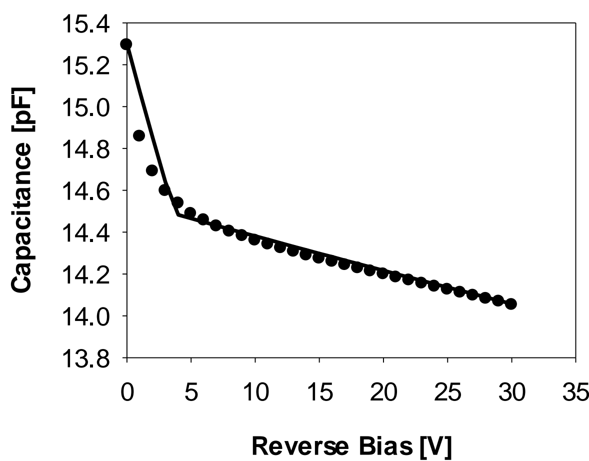

Figure 4.18 (e)

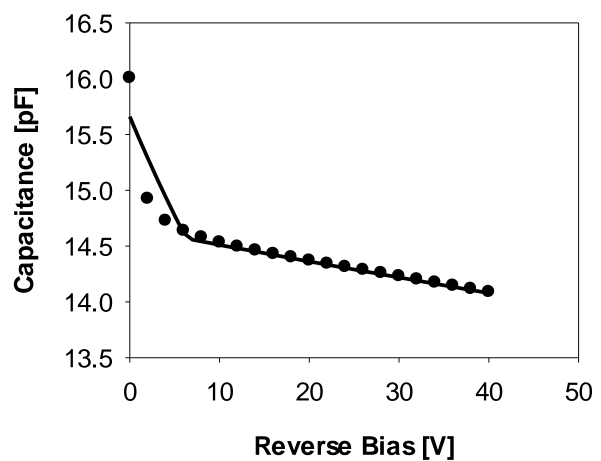

Figure 4.18 (f)

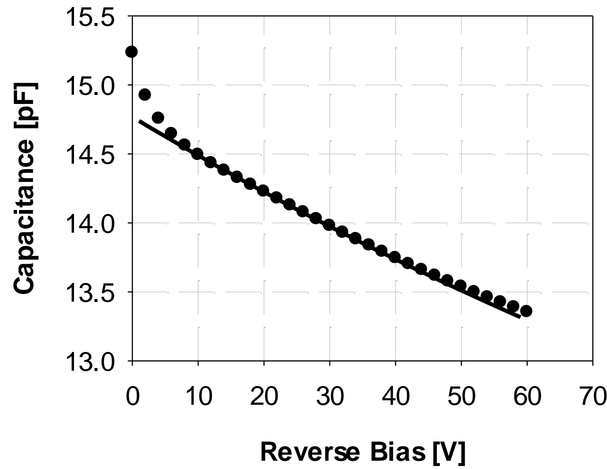

(g)

Figure 4.18: The experiment (circles) and modelling (lines) CV results of $Al_xGa_{1-x}InP$ PIN structure used in this work. (a) MR2925 with 0 % Al. (b) MR3921 with 31 % Al. (c) MR3920 with 47 % Al. (d) MR3919 with 61 % Al. (e) MR3916 with 64 % Al. (f) MR3917 with 78 % Al. (g) MR2812 with 100 % Al.

The Capacitance-voltage (C-V) characteristics of the $Al_xGa_{1-x}InP$ devices are shown in Figure 4.18. The doping densities in p^+ and n^+ claddings, i region doping density and i region width are derived from the C-V results by solving Poisson's equation numerically. Assuming that the doping densities in n^+ claddings in these devices is 2×10^{18} cm^{-3} [93], the doping density in p^+ claddings were determined between 2×10^{17} and 2×10^{18}, which are similar to those reported in [54]. The total depletion width, w in these devices is estimated as 0.93 to 1 µm.

4.7.3 IV Measurement

The reverse dark IV characteristics measured on the largest size devices (ϕ = 420 µm) $Al_xGa_{1-x}InP$ diodes are shown in Figure 4.19. The large bandgap means the dark current of these devices is less than 1 nA at 95% breakdown voltage. Excess noise cannot be measured easily if the dark current is too high or the primary photocurrent is too low. Fortunately, the dark current in these devices is sufficiently low for excess noise measurement to be carried out.

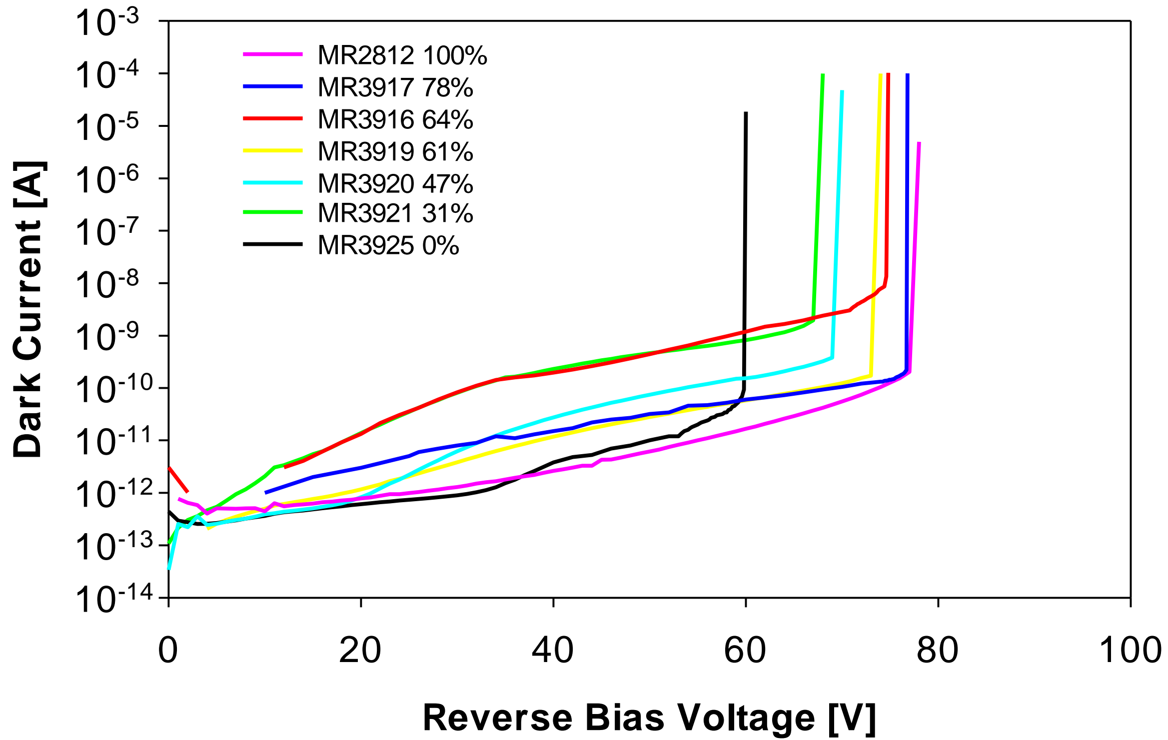

Figure 4.19: Measured reverse dark current characteristics of 200 µm radius PIN AlInP PIN diodes with Al fraction = 100 %, 78 %, 64 %, 61 %, 47 %, 31 % and 0 %.

4.7.4 Photo-multiplication Characterisation

Spectral response measurements were undertaken on seven $Al_xGa_{1-x}InP$ diodes using a white light source and a monochromator. Characterisation of the optical absorption characteristics of this material is required to determine the correct wavelength of the light source for excess noise and photomultilplcation measurements. The peak of the spectral response of the PIN $Al_xGa_{1-x}InP$ (100 %, 78 %, 64 %, 61 %, 47 %, 31 % and 0 %.) at reverse bias voltages of -5 V was found to be ~ 480 nm, 505 nm, 520nm, 530nm, 555nm, 590nm and 655nm, respectively [54]. Only 543 nm and 633 nm wavelength gas lasers can be used for multiplication and excess noise measurements because of the limited availability of lasers in the laboratory. However, these are not sufficiently close to the $Al_xGa_{1-x}InP$ devices peak wavelength. It is necessary to choose the wavelength of any LED or laser appropriately in order to obtain the desired injection conditions.

Multiplication and excess noise measurements were performed using a several LEDs and lasers. For the 430 nm LED [94], 460nm LED [95] and 543nm laser beam, more than 99.9% of photons are absorbed in the 1.0 µm top doped cladding layer in $Al_xGa_{1-x}InP$ (x = 1), Al_xGa_{1-}

$_x$InP (0.47 ≤ x ≤ 0.78) and $Al_xGa_{1-x}InP$ (x ≤ 0.31), respectively, giving virtually pure electron initiated multiplication [54]. For the 460 nm LED [95], 505 nm LED [96], 525 nm LED [97], 530 nm LED [98], 543 nm laser, 590 nm LED [99] and 633 nm laser, these wavelength of the light source absorbed within the depletion region of the AlInP, $Al_{0.78}Ga_{0.22}InP$, $Al_{0.64}Ga_{0.36}InP$, $Al_{0.61}Ga_{0.39}InP$, $Al_{0.47}Ga_{0.53}InP$, $Al_{0.31}Ga_{0.67}InP$ and GaInP, respectively. It will give a significant mixed carrier multiplication characteristic. The details of the above information are shown in table 4.3.

	Pure Injection	Mixed Injection
AlInP	430 nm LED [94]	460 nm LED [95]
$Al_{0.78}Ga_{0.22}InP$	460nm LED [95]	505 nm LED [96]
$Al_{0.64}Ga_{0.36}InP$	460nm LED [95]	525 nm LED [97]
$Al_{0.61}Ga_{0.39}InP$	460nm LED [95]	530 nm LED [98]
$Al_{0.47}Ga_{0.53}InP$	460nm LED [95]	543 nm laser
$Al_{0.31}Ga_{0.67}InP$	543nm laser	590 nm LED [99]
GaInP	543nm laser	633 nm laser

Table 4.3: Pure and mixed injection of the $Al_xGa_{1-x}InP$.

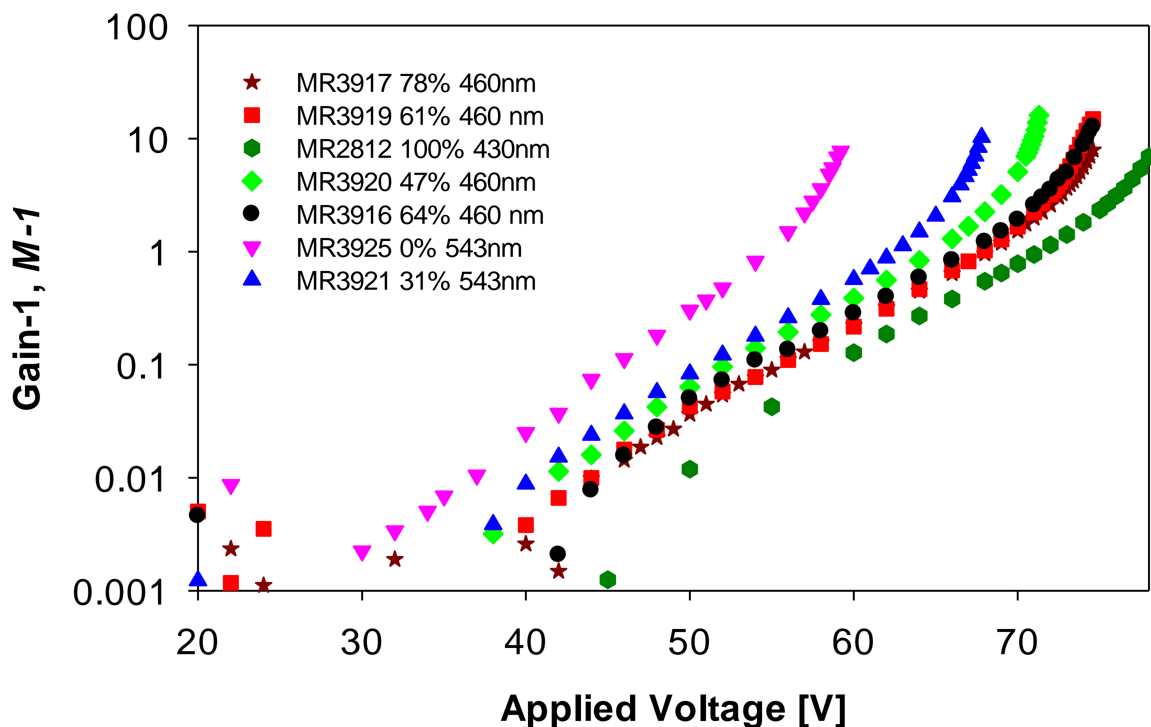

Figure 4.20: Experimental *M*-1 versus reverse Bias for $Al_xGa_{1-x}InP$ PIN diodes using 430 nm LED, 460 nm LED and 543 nm Laser.

Figure 4.20 shows the pure injection multiplication characteristics obtained on the $Al_xGa_{1-x}InP$ diodes plotted as log(*M*-1), to understand the low field multiplication characteristics.

4.7.5 Excess Noise Characterisation

The measurements were performed using the setup described in this chapter. A 460nm LED, 505nm LED, 525 nm LED, 530 nm LED, 590 nm LED, 543 nm laser beam, 590 nm LED and 633 nm laser beam was used to match the different Al fraction AlGaInP's peak wavelength yielding mixed injection. In addition, a 430 nm LED, a 460 nm LED and a 543 nm laser beam was used as the light source to the measure the excess noise characteristics yielding pure injection for the different Al fraction AlGaInP devices.

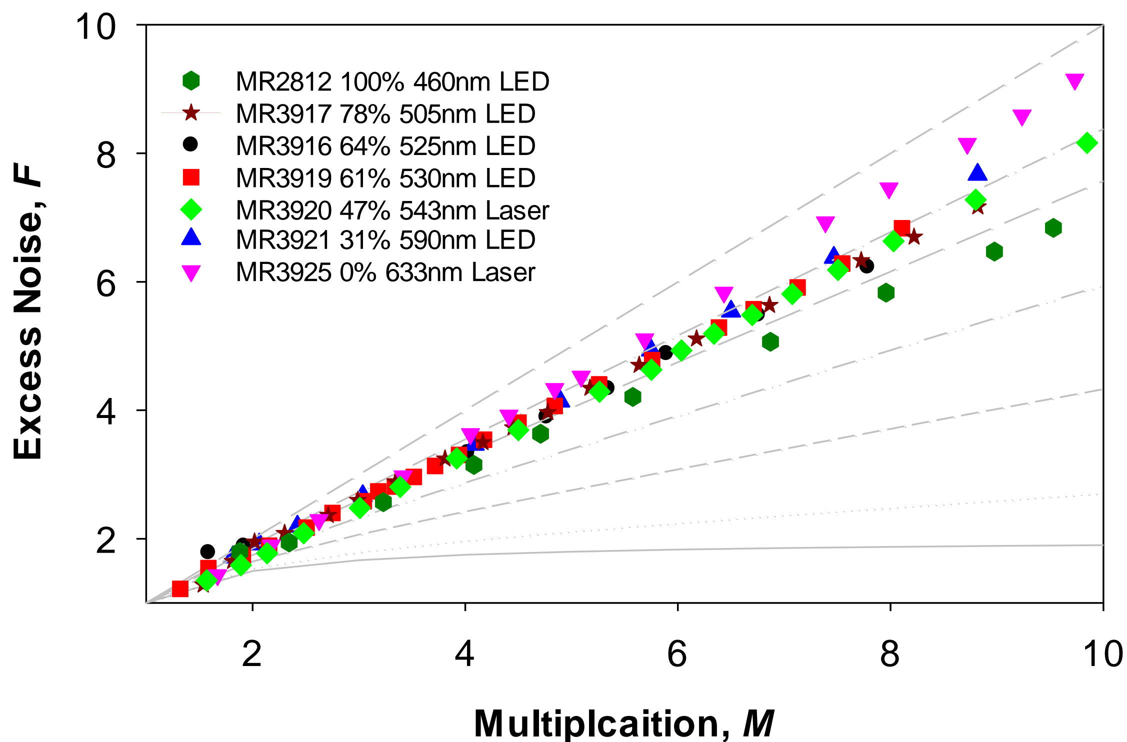

Figure 4.21 : Experimental mixed injection *F* versus *M* using 460 nm LED, 505 nm LED, 525 nm LED, 530 nm LED, 543 nm laser, 590 nm LED and 633nm laser for AlInP PIN diodes with Al fraction = 100% (dark green hex), 78% (dark red star), 64% (black circle), 61% (red square), 47% (green diamond), 31% (blue triangle up) and 0% (pink triangle down). Grey lines are McIntyre's curves with $k = 0$, 0.1, 0.3 0.5, 0.7, 0.8 and 1.

The excess noise-multiplication characteristics for a $Al_xGa_{1-x}InP$ PIN structures (mixed injection) using several different wavelength light source is shown in Figure 4.21. The grey lines correspond to McIntyre's noise model based on the β/α (k) ratio. The excess noise factor is reduced from 0.9 to 0.65 with increasing Al fraction. For the AlInP (Al fraction = 100), the

excess noise factor is equal to 0.65 and it has good agreement with the data which is using Lau's system. The details will be shown in chapter 5.

The excess noise of AlGaInP (Al fraction from 31%-78%) resulting from mixed injection corresponds to k values from 0.7 to 0.8. The excess noises of GaInP (Al fraction = 0) has the highest excess noise factor which is 0.9.

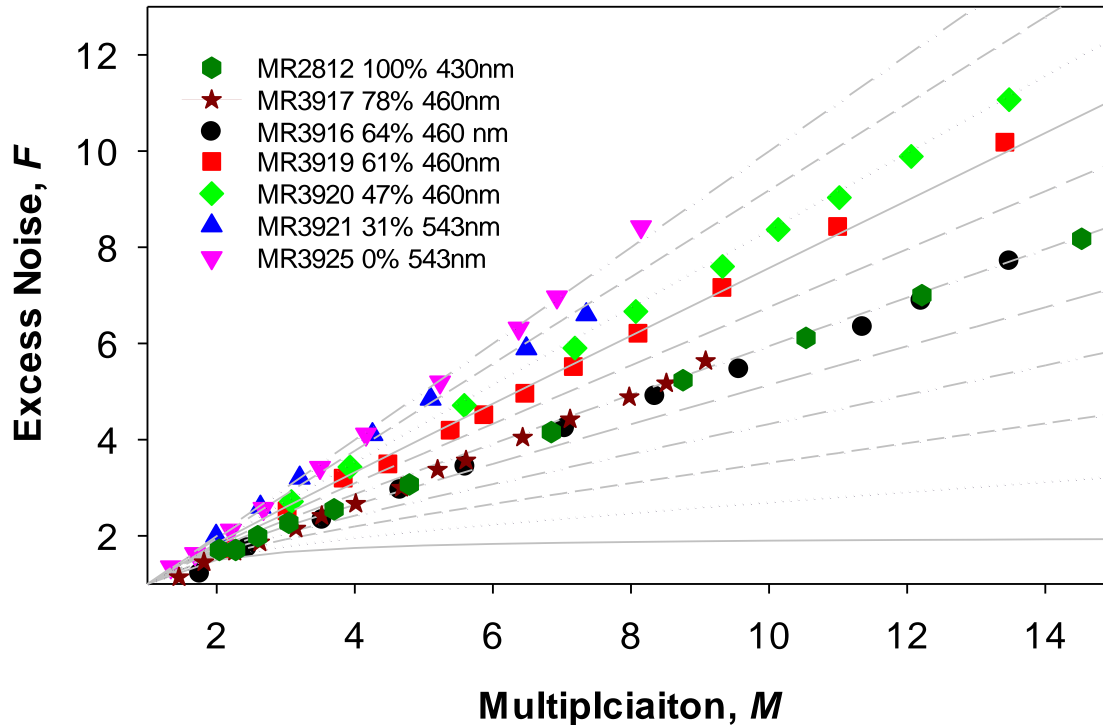

Figure 4.22: Experimental pure injection F versus M using 430 nm LED, 460 nm LED and 543 nm laser for AlInP PIN diodes with Al fraction = 100% (dark green hex), 78% (dark red star), 64% (black circle), 61% (red square), 47% (green diamond), 31% (blue triangle up) and 0% (pink triangle down). Grey lines are McIntyre's curves with k = 0 to 1 in steps of 0.1.

Figure 4.22 shows the excess noise-multiplication characteristics for $Al_xGa_{1-x}InP$ PIN structures using 430 nm LED, 460 nm LED and 543 nm Laser. The grey lines correspond to the McIntyre noise theory based on the β/α (k) ratio. For the AlInP (fraction = 100%) diode, the excess noise factors of the pure electron injection (430 nm) is in good agreement with the data published by Qiao *et al* [57].

The excess noise of the GaInP and $Al_{0.31}Ga_{0.69}InP$ using 543 nm laser correspond to k = 1.05 and k = 0.9, respectively. The mixed injection excess noise factors of two low Al fraction devices (Figure 4.21) are lower than the pure electron injection (Figure 4.22). The excess noises of $Al_{0.61}Ga_{0.39}InP$ and $Al_{0.47}Ga_{0.53}InP$ resulting from pure electron injection using 460 nm LED

correspond to $k = 0.7$ and $k = 0.8$, respectively. In the case of $Al_{0.64}Ga_{0.36}InP$ and $Al_{0.78}Ga_{0.22}InP$ a lower excess noise, corresponding to $k = 0.5$, is obtained and have similar results as the AlInP (Al fraction = 100%). Figure 4.21 and Figure 4.22 show the mixed injection excess noise factor of the $Al_xGa_{1-x}InP$ ($0.31 < x < 1$) is higher than the pure electron injection.

The excess noise falls with increasing x. This suggests that the dead space effect, which is defined as the minimum distance a carrier has to travel to gain the ionisation threshold energy [100], in $Al_xGa_{1-x}InP$ ($0 < x < 0.64$) diodes is significant and increases with x. This dead space effect can reduce the randomness in carrier ionization and hence diodes experiencing dead space effects produce lower excess noise than is predicted by the local model.

4.7.6 Comparison of the Excess Noise with Low and High Input Current

The new measurement system has been used to measure multiplication and excess noise factor of the AlInP (MR2812) using 460 nm light. The AlInP APD used in this work with nominal *i* region widths, w = 1 µm, previously reported in [57]. Figure 4.23 shows the photocurrent and multiplication of the AlInP diode using the 442 nm LED. The multiplication of this diode can reach approximately 25 when the primary photocurrent at 0 V was 4 nA.

The excess noise versus multiplication characteristics for an AlInP diode using 460 nm LED illumination for several optical powers is shown in Figure 4.24. The grey lines correspond to the McIntyre noise theory based on the β/α (k) ratio. The excess noise using the previous measurement system required a minimum of 0.22 µA photocurrent whereas this system now requires 10 nA representing more than 22 times improvement in sensitivity. The excess noise factor of AlInP diodes with optical power attenuated by $10^{-2.3}$ and 10^{0} is similar and has been published [57].

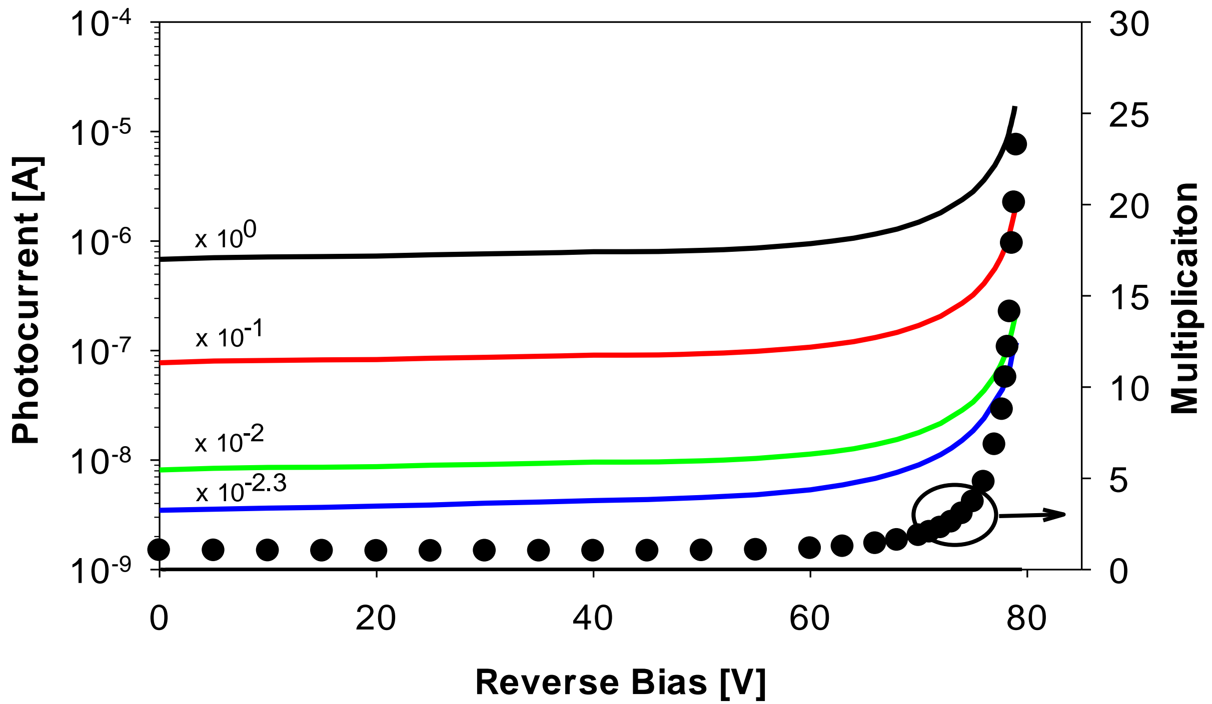

Figure 4.23: Measured photocurrent in AlInP diodes under 460 nm LED illumination with the optical power attenuated by 10^{0}, 10^{-1}, 10^{-2} and $10^{-2.3}$. Also shown is the corresponding gain as a function of bias voltage.

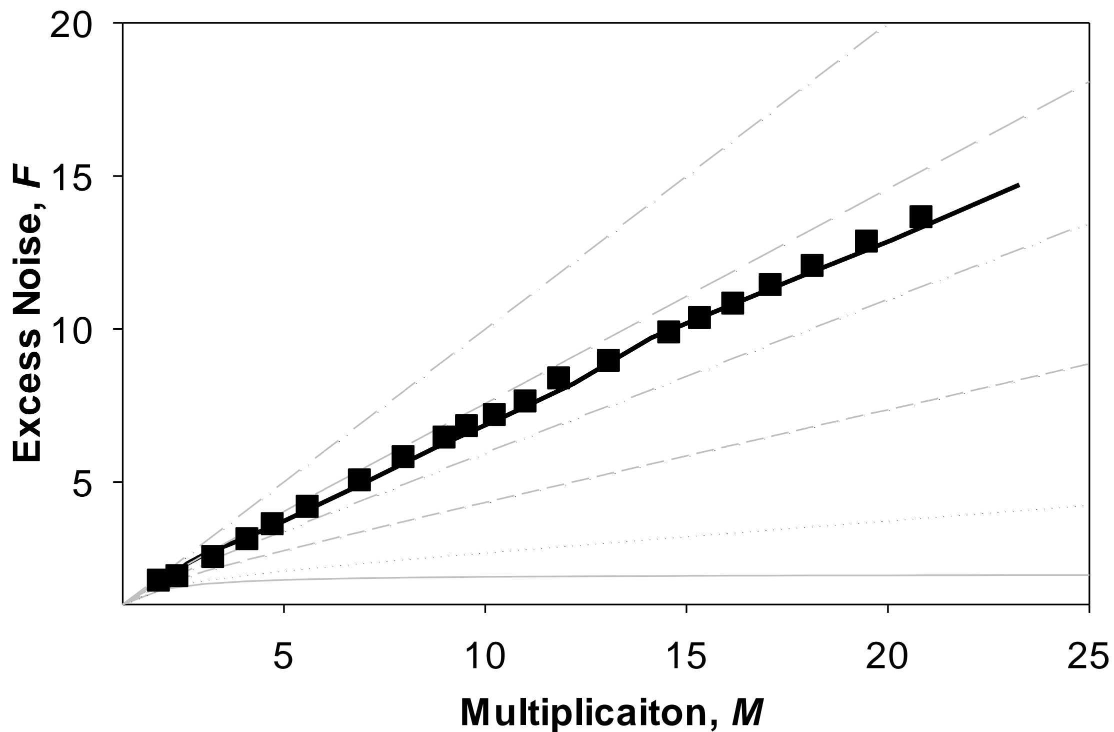

Figure 4.24: Experimental F versus M using 460 nm LED for AlInP diodes with optical power attenuated by $10^{-2.3}$(■) and 10^{0}(solid line).

4.7 Conclusion

A versatile system for measuring multiplication and excess noise in avalanche photodiodes is described and its performance analysed. The system can measure the multiplication and excess noise of APDs in the presence of high dark current when the photocurrent is approximately 10 nA. This system is at least one order of magnitude better than Lau's system in this regard. Signal to noise ratio (SNR) is an excellent method of comparison between different measurement systems with independent system bandwidths and input impedances. The SNR of this system is at least two orders of the magnitude higher than the other measurement systems. However, the excess noise factor can be measured using this system on device with a junction capacitance up to approximately 22 pF. It is the lowest of all reported measurement systems, but this range can still cover the capacitances of majority APDs of interest. If the capacitance of the measured device is too large to perform the noise measurement, devices of smaller area may be fabricated to facilitate the measurement.

Author	Min Photocurrent (μA)	SNR (dB) ($C_j = 1$ pF)	Max C_j (1 pF)
Current System	0.01	2.62	22
Bulman *et al.*	0.63	-36.72	106
Xie *et al.*	2.5	-31.58	636
Ando *et al.*	6.25	-23.98	106
Lau *et al.*	0.22	-25.7	50
Green *et al.*	1	-25.55	5000

Table 4.3: Compare between different noise measurements systems. SNR is calculated using 1 μA signal current.

This new excess noise measurement system measure the avalanche multiplication and excess noise on the $Al_xGa_{1-x}InP$ PIN diode with different composition under pure and mixed injection condition. For the excess noise of the AlInP (Al fraction =1) diodes, it has good agreement with the data published by Qiao *et al.* [57]. The excess noise of the $Al_xGa_{1-x}InP$ diode is reduced and dead space effect is significant with increasing x.

Chapter 5: Room Temperature Avalanche Multiplication and Excess Noise Characteristics of AlInP Diodes

5.1 Introduction

$Al_{0.52}In_{0.48}P$ (hereafter AlInP) being the widest latticed matched semiconductor to GaAs has the potential to be utilized as the avalanche multiplication region in GaAs based avalanche photodiodes (APDs). AlInP APDs can be used for underwater communication systems because seawater has a minimum attenuation between 450 nm to 520 nm and these wavelengths are absorbed in AlInP [37]. As a wide bandgap semiconductor, it benefits from a very low dark current. However in 'photon starved' situations, one may wish to use the impact ionization process to provide avalanche multiplication and gain. Ong *et al.* [39] have determined the ionization coefficients in this material, so the multiplication versus reverse bias voltage can be estimated. Cheong *et al.* [38] have shown a high performance separate absorption multiplication APD (SAM-APD) with a high responsivity of ~18 A/W at 480 nm with a gain of 167. There are however no experimental reports of excess noise for AlInP.

In this chapter, a 460 nm LED (170 mW) and a 442 nm gas laser are used to measure the multiplication and excess noise factor of a set of AlInP diodes with different intrinsic widths (from 0.04 µm to 1 µm) and different layer ordering (PIN and NIP). Mixed injection results (460 nm) are compared with pure electron injection results (442 nm) in order to further refine the impact ionisation coefficients. Being the widest bandgap (2.28eV) material which can be grown matched to GaAs, it is showed tunnelling effect is negligible in AlInP even at high-fields > 1MV/cm and therefore it is possible to grow a thin device (0.04 µm). Using 460 nm wavelength light, measurements showed that a separate absorption multiplication avalanche photodiode (SAM-APD) with a nominal multiplication region width of 0.2 µm had an effective *k* (hole to electron ionization coefficient ratio) of ~ 0.3.

5.2 Layer Details

The set of diodes used in this work include the four homo-junction PINs and a NIP structure with nominal *i* region widths, *w* of 0.04, 0.2, 0.5, 1.0, and 0.8 µm, respectively, The structure of the layers is as follows: a doped GaAs buffer layer followed by a 0.3 µm doped AlInP

cladding region, the undoped AlInP layer, a 1 μm doped top AlInP cladding layer and finally a thin 0.1 μm heavily doped contact layer to facilitate top ohmic contact formation. This work also includes the SAM-APD with a nominal multiplication region width of 0.2 μm. The structure details of the PIN or NIP and SAM-APD are shown in table 5.1 and table 5.2, respectively.

Wafer	Sample number	Structure	Top/bottom cladding thickness (μm)	$n^{+}/i/p^{+}$ doping ($10^{18} cm^{-3}$)	Width (μm)
MR2827	P2	PIN	1/0.3	4.4 / 0.004 / 0.25-0.43	0.04
MR2806	P3	PIN	1/0.3	4.4 / 0.01 / 0.25-0.43	0.2
MR2812	P6	PIN	1/0.3	4.4 / 0.001 / 0.24-0.43	1
Ts577-1	P7	PIN	1/0.3	4.4 / 1.5 / 0.24-0.43	0.5
MR2807	N3	NIP	1/0.3	4.4 / 0.003 / 0.24-0.43	0.8

Table 5.1: The structure of the PIN and NIP AlInP diodes .

Purpose	Thickness (nm)	Material	Type	Doping (cm^{-3})
Cladding	50	GaAs	p^{+}	2×10^{18}
	1000	$Al_{0.52}In_{0.48}P$	p^{+}	2×10^{18}
Absorber	1000	$Al_{0.52}In_{0.48}P$	i	---
Charge	175	$Al_{0.52}In_{0.48}P$	p^{-}	3.0×10^{17}
Avalanche	200	$Al_{0.52}In_{0.48}P$	i	---
Cladding	300	$Al_{0.52}In_{0.48}P$	n^{+}	2×10^{18}
Buffer	500	GaAs	n^{+}	2×10^{18}
Substrate		GaAs	n^{+}	

Table 5.2: The structure of the AlInP SAM-APD

To ensure that the incident light is not attenuated by the 50 nm heavily doped GaAs contacting layer, it was selectively etched from the central window region of the circular mesa devices. As excess noise measurements can be sensitive to any ‘mixed’ carrier injection into the high field region, the mesa sidewalls were passivated and covered by metal to prevent any edge illumination during the measurement. It is important to make sure that the edges of the diodes

were fully covered with the photoresist, otherwise the diodes will be short circuit after the final metal deposition stage. The details of the diode passivation can be found in [109].

5.3 Electrical Characterisation

5.3.1 IV Measurement

The reverse dark *I-V* characteristics measured on the PINs and NIP AlInP diodes where the largest size devices (ϕ = 420 µm) are shown in Figure 5.1. All devices have the low dark leakage current which is less than 0.1 nA at 95% of the breakdown voltage. Due to the limitation of the equipment, dark currents in the smaller size devices could not be measured. Therefore, Figure 5.1 only shows the largest size devices results. Nonetheless, because of the large band-gap in AlInP, no tunnelling current was observed even in the thinnest (w = 0.04 µm) diode structure.

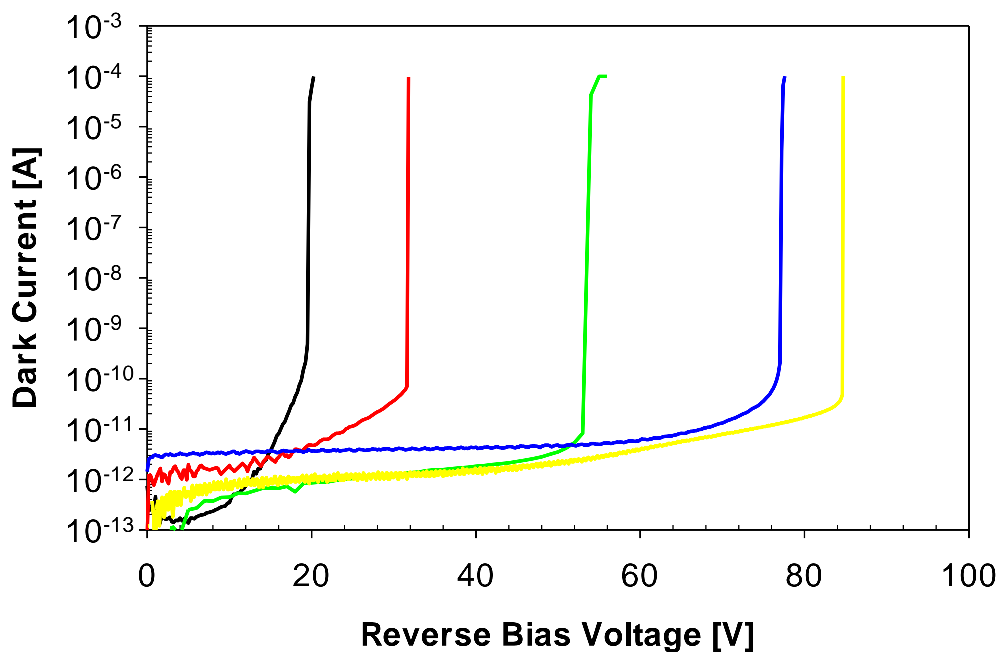

Figure 5.1: Measured reverse dark current characteristics of 200 µm radius PIN and NIP diodes.

Figure 5.2 shows the dark current, photocurrent and multiplication for the AlInP SAM-APD using the 460 nm LED. The dark current is less than 10 pA at 99 % of the breakdown voltage for a 210 µm radius device. Such a low dark current in the device allows the direct measurement of photocurrent even when the optical power was attenuated by 10^7 down to ~1 pW. There is no tunnelling current despite the peak electrical field exceeding 1 MV/cm and the multiplication – voltage (*M-V*) curve shows a gain of 90 can be obtained. The multiplication

here however, was measured using only the 460 nm LED as due to the thick cladding and absorption regions, most of the photons were absorbed before entering the high-field region and therefore can be assumed to be initiated by electrons only.

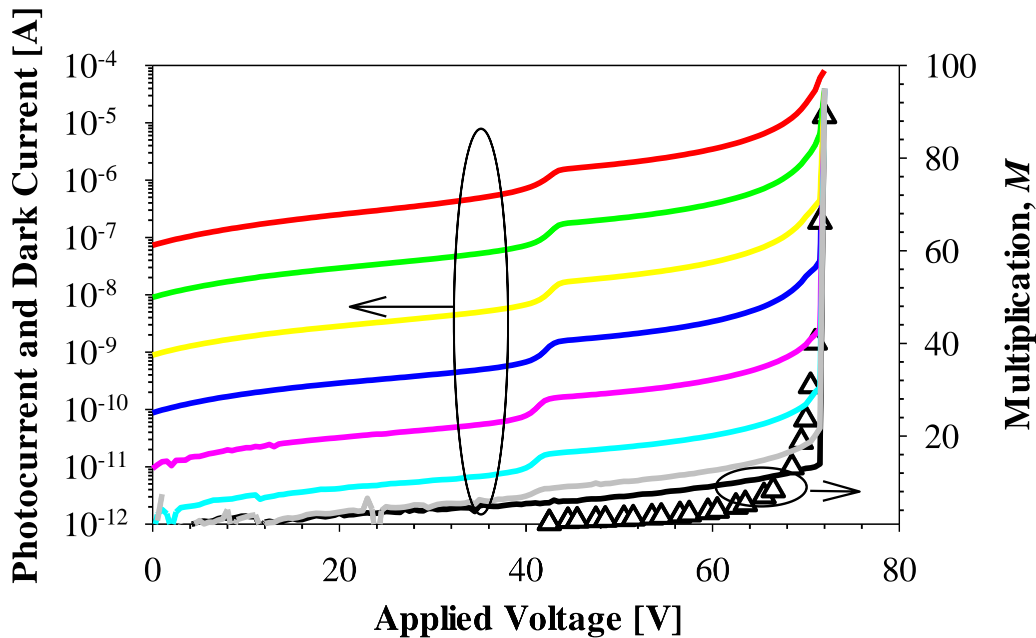

Figure 5. 2: Measured dark current (——) and photocurrents (colour line) in AlInP SAM-APD under 460 nm LED illumination with the optical power attenuated by 10^0 to 10^6. Also shown is the corresponding gain as a function of bias voltage.

5.3.2 CV Measurement

The Capacitance-voltage (*C-V*) measurement was performed on the PINs, NIP and SAM-APD AlInP diodes are shown in Figure 5.3. *C-V* measurements revealed that the doping densities in p^+ and n^+ claddings in all structures are ~ 3×10^{17} cm^{-3} and ~ 4×10^{18} cm^{-3} , similar to those reported in [39]. Using the *C-V* data and solving Poisson's equation, electric field profiles in these structures were simulated at their corresponding breakdown voltages, as shown in Fig. 5.4. The total width was estimated as 0.04, 0.2, 0.5 and 1 μm for the PINs and 0.8 μm for the NIP. The built in potential in AlInP APDs is assumed to be 2.2 V, it is obtained from $1/C^2$ versus voltage. The total depletion widths are thicker than the nominal *i* thicknesses due to the relatively low doping densities in the p^+ claddings which results in a significant depletion into the p^+ cladding layers, especially in the thinnest PIN. For simplicity, hereafter the nominal thicknesses are used in the discussion.

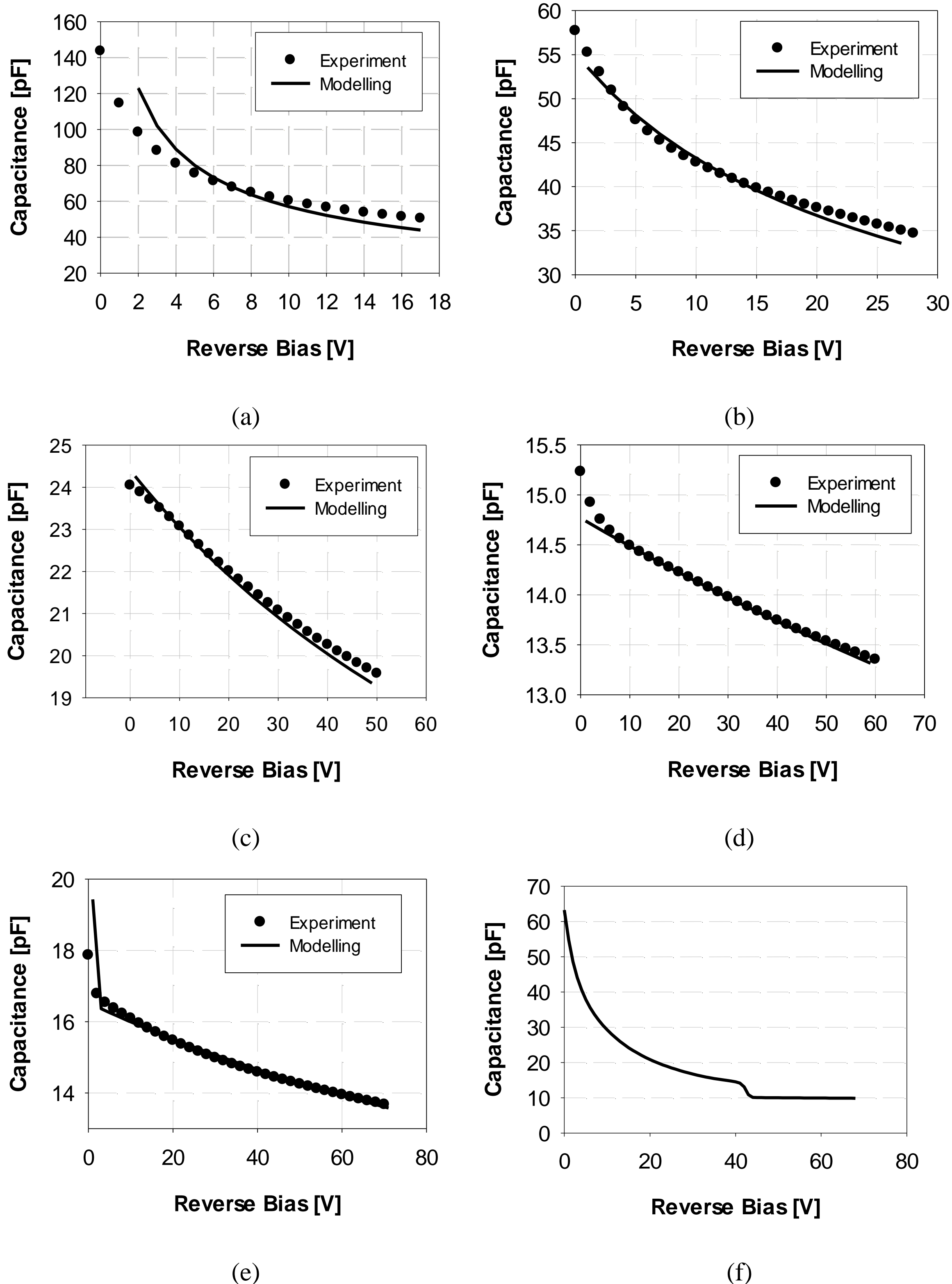

Figure 5.3: The experiment (circle) and modelling (line) CV results of AlInP PIN, NIP and SAM-APD structure used in this work. (a) MR2827 P2 (PIN) with 0.04 µm (b) MR2806 P3 (PIN) with 0.22 µm. (c) TS577-1 P7 (PIN) with 0.5 µm. (d) MR2812 P6 (PIN) with 1 µm. (e) MR2807 N3 (NIP) with 0.8µm. (f). MR3910 (SAM-APD) with 0.2 µm.

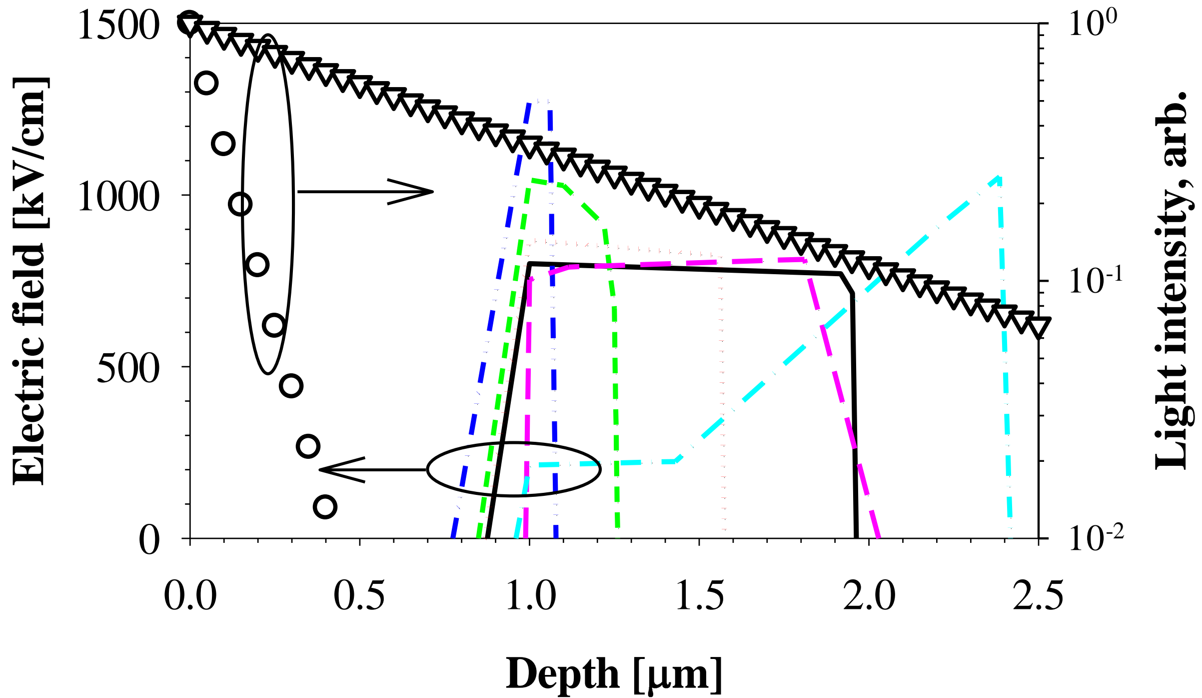

Figure 5.4: Simulated electric field profiles in PINs (w = 1, 0.5, 0.2, 0.04 μm), a NIP (w = 0.8 μm) and the SAM-APD using the results obtained from capacitive-voltage measurement shown as solid (black), dotted (red), short-dashed (green), dashed-dot-dot (blue), long-dashed (pink) and dashed-dot lines (cyan). Also illustrate the absorption profiles of 442 nm and 480 nm, i.e. the light attenuation vs distance, as circles and triangles.

5.4 Photomultiplication Characteristics

To determine if the multiplication characteristics obtained from these light sources are initiated by a single carrier type or otherwise, the absorption profiles for 442 nm and 480 nm wavelength photons in AlInP were calculated using the absorption coefficients [101] as illustrated in Figure 5.4.

Using a white light source and a monochromator, the peak spectral response of PIN and NIP AlInP diodes at reverse bias voltages of -5 V was found to be ~ 480 nm with a FWHM of approximately 22 nm which is narrower than that of previous work [38]. Accounting for the spectral response characteristics of AlInP diodes as illustrated in Figure 5.5, only 442 nm and 532 nm wavelength gas lasers can be used for multiplication and excess noise measurements due to the limited availability of lasers in the laboratory. However, 532 nm is weakly absorbed and there is insufficient optical generation for the excess noise measurement. In order to obtain a light source with a peak emission wavelength close to 480 nm, a Thorlabs LED470L LED is used.

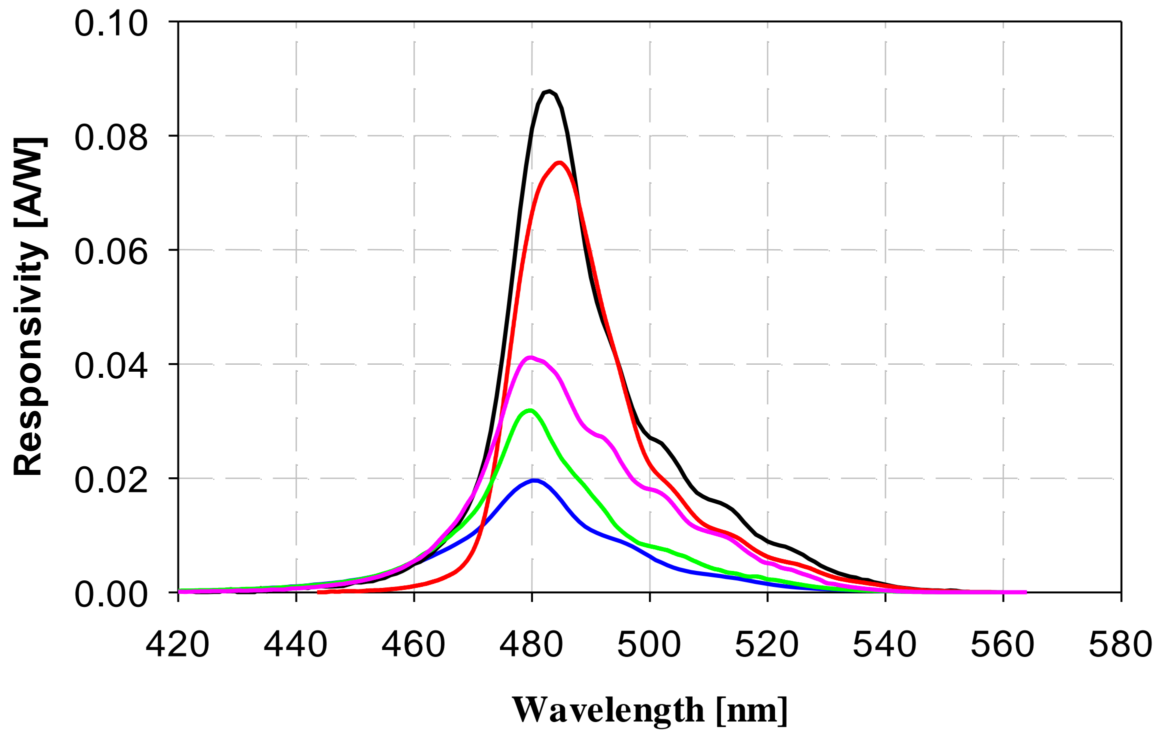

Figure 5.5: Spectral response characteristics of AlInP diodes in PINs (w = 1, 0.5, 0.2 and 0.04 μm), a NIP (w = 0.8 μm) at reverse bias voltages of -5 V as shown black, red, green, blue and pink lines.

Multiplication and excess noise measurements were undertaken using a 442 nm He-Cd laser and a Thorlabs LED470L LED with a 460 nm peak emission [95]. The latter offers the closest emission wavelength available in commercial LEDs with a reasonable output power at 480 nm. For 442 nm, the reported absorption coefficient in AlInp is 1×10^{5} cm^{-3} [101], so more than 99.9% of photons are absorbed in the 1.0 μm top doped cladding layer, giving virtually pure electron (or hole) initiated multiplication. For the 460 nm emission from the LED, due to the relatively short diffusion lengths in the doped AlInP, most of the photocurrent is contributed by the longer wavelength components of the LED spectrum absorbed within the depletion region. This results in a significant mixed carrier multiplication characteristic.

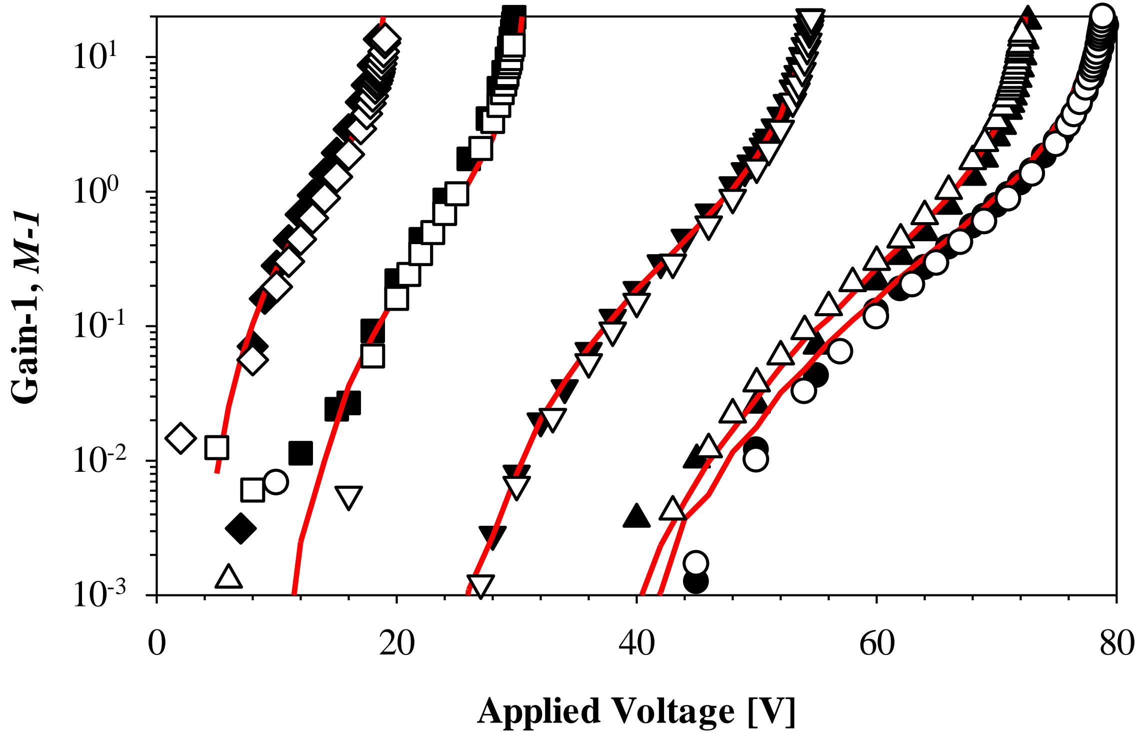

Figure 5.6: Experimental M-1 versus reverse Bias for AlInP PIN diodes using 442 nm laser (close symbol) and 460 nm LED (open symbol) with w = 0.04 µm (♦,◊), 0.2 µm (■,□), 0.5 µm (▼,∇) and 1.0 µm (●,○) and NIP diodes with w = 0.8 µm (▲,∆). Solid lines are modelled results assuming 442 nm illumination.

Figure 5.6 shows the multiplication characteristics obtained in the PINs (NIP) plotted as log(M-1), to emphasize the low field multiplication characteristics. As β/α ~ 0.7, even at low fields, the difference between 442 nm and 460 nm appears almost indistinguishable, especially in the thinner avalanching structures. The maximum gain in these devices is approximately 20 probably due to un-optimized etching process in these mesa devices, resulting in high electric field at the mesa edges [102].

5.5 Excess Noise Characteristics

The measurements were performed using the setup described in Lau *et al.* [18]. The transimpendance amplifier (TIA), based on the Analogue Devices AD9631 with a gain of 2200 V/A (unterminated) was used to convert current into a voltage. The output of the TIA was then amplified by the Minicircuits ZFL-500LN+ and fed into a bandpass filter SBP-10.7+, which had a pass band centred around 10 MHz and a bandwidth of 4.2 MHz. A 442 nm laser beam and a Thorlabs LED470L LED with a 460 nm peak emission [95] was used as the light source to measure the excess noise characteristics yielding pure electron injection and mixed injection, respectively.

Excess noise measurements are sensitive to any 'mixed' carrier injection into the high field region, In order to obtain accurate excess noise factor measurements, the mesa sidewalls were passivated and covered by metal to prevent any edge illumination during the measurement.

Figure 5.7 shows the excess noise-multiplication characteristics for the AlInP PIN and NIP structures using 442 nm laser illumination. Also shown are the excess noise characteristics for the AlInP PIN and NIP, together with the results from the SAM-APD obtained using 460 nm illumination. The grey lines correspond to the McIntyre noise theory based on the β/α (k) ratio.

The excess noise factor of the mixed injection (460 nm) is higher than the pure electron injection (442 nm) in the 1.0 µm PIN structure. This is due to the contribution of holes in the multiplication process which is detrimental to the noise. The opposite behaviour is seen in the 0.8 µm thick NIP structure where the highest noise is obtained with the use of 442 nm laser excitation with holes initiating the multiplication, compared to the 460 nm. The ionization coefficient ratio, k, should vary from ~0.6 for the thickest structure investigated here to ~1 for the thinner structures, in contrast to the experimental results.

Decreasing the width, w, in the PIN structures, results in the excess noise decreasing to levels corresponding to $k = 0.32$ and $k = 0.11$, in the 0.2 and 0.04 µm structures respectively. The results of the pure injection and mixed injection are quite similar in these thin structures, because the impact ionization coefficients α and β are almost identical when the intrinsic region width is less than 0.5 µm [39]. The excess noise of the SAM-APD is close to $k = 0.3$ as seen in Figure 5.7 and in agreement with the data from the PIN with the 0.2 µm nominal *i* region width.

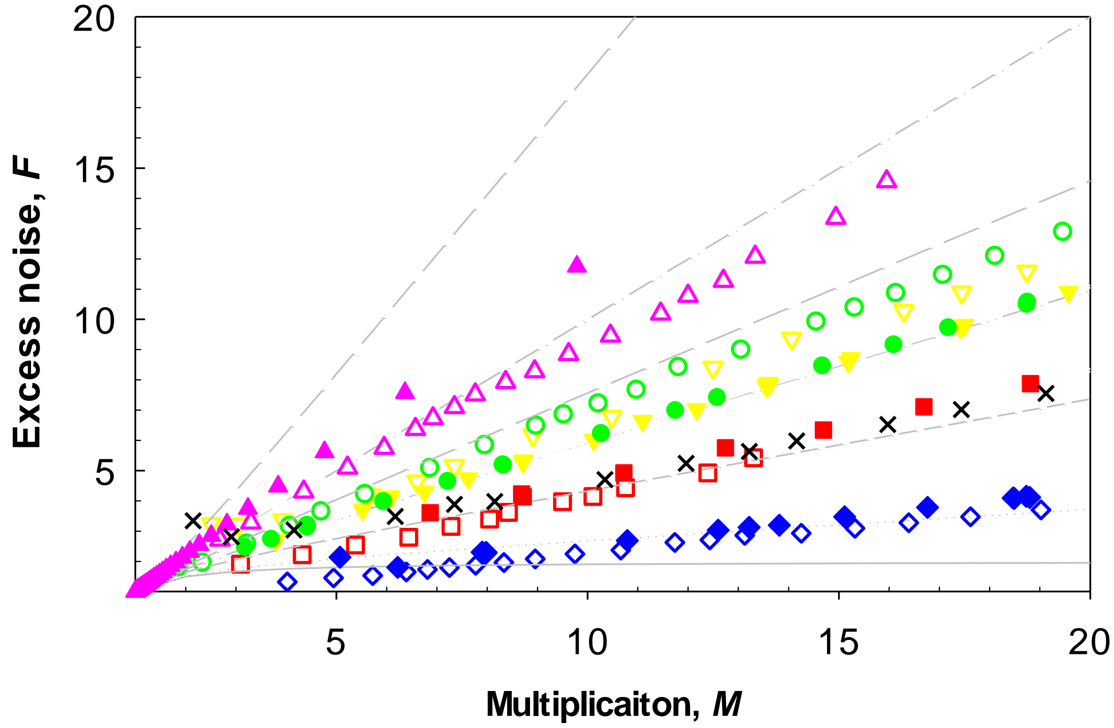

Figure 5.7: Experimental F versus M using 442 nm laser (closed symbols) and 460 nm LED (open symbols) for AlInP PIN diodes with w = 0.04 µm (blue), 0.2 µm (red), 0.5 µm (yellow) and 1.0 µm (green), NIP diodes with w = 0.8 µm (pink) and SAM-APD (×). Grey lines are McIntyre's curves with k = 0, 0.1, 0.3 0.5, 0.7, 1 and 1.2.

5.6 Modelling

5.6.1 Random path length (RPL) model

Simulation of $M(V)$ and $F(M)$ in the presence of a dead-space can be implemented using a method initially proposed by Hayat *et al.*. [103] or the random-path length (RPL) model [100]. The latter was used in this work. To account for the non-uniform electric field profile in these devices, the electron ionization probability density, $h_e(x_0,x)$ which describes the ionizing probability of an electron at x_0 after travelling a distance x can be expressed as [104]

$$h_e(x_0,x)=\begin{cases} 0 & ,x\le d_e(x_0) \\ \alpha^*(x+x_0)\exp\left[-\int_{d_e(x_0)}^{x}\alpha^*(z+x_0)dz\right] & ,x>d_e(x_0) \end{cases} \tag{5.2}$$

In (5.2), $d_e(x_0)$ is the distance of the dead-space, which is derived from the threshold energy, E_{the} and electric field, ξ given by

$$E_{the} = \int_{d_e(x_0)}^{x} \xi(x)dx \tag{5.3}$$

By integrating (5.2), the probability of an electron not ionizing after travelling a distance x from x_0, r is expressed as

$$\ln(r) = -\int_{d_e(x_0)}^{x} \alpha^*(z + x_0)dz \tag{5.4}$$

where $0 < r < 1$ determines the electron (hole) ionizing length. The multiplication can be easily computed after all the carriers exit the depletion width. The expressions for holes are easily obtained by replacing α^*, d_e and E_{the} with β^*, d_h and E_{thh} respectively. The depletion width was discretized into a suitable mesh to calculate d_e (d_h) and $\alpha^*(\beta^*)$. The simulation was repeated until the multiplication value converges.

The excess noise factor, F is given by

$$F = \frac{< M^2 >}{< M >^2} \tag{5.5}$$

So that M and F can be determined from

$$M = \frac{1}{n_T}\sum_{i=1}^{n_T} M_i \tag{5.6}$$

and

$$F = \frac{1}{n_T M^2}\sum_{i=1}^{n_T} M_i^2 \tag{5.7}$$

Where M_i is the multiplication from a trial and n_T is the total number of trials used. In each trial, assume that an electron diffuses into the high field region. The primary carrier creates a secondary e-h pair after traveling a random ionization path length based on (5.4) and terminating within the depletion region. This process is repeated until all carries leave the depletion region. The enabled ionization coefficients $\alpha^*(\beta^*)$, were obtained from the local parameterized ionization coefficients, $\alpha'(\beta')$ using a simple correction $\frac{1}{\alpha^*} = \frac{1}{\alpha'} - 2d_e$ and $\frac{1}{\beta^*} = \frac{1}{\beta'} - 2d_h$ [100], where both $\alpha'(\beta')$ and $d_e(d_h)$ can be found in [104]. This model was developed by Cheong et al. [100], and shows a better fit than the previous model which uses only one dead space. The details of the non-uniform electric field will be discussed in Appendix D [58].

5.6.2 Results

The simulations were completed assuming a pure single carrier initiated multiplication, i.e. 442 nm illumination, using the electric field profile shown in Figure 5.4. There is good agreement between the simulated multiplication and experimentally determined values over a wide dynamic range, even in thinnest devices where the dead space effect is significant, as shown by the solid lines in Figure 5.6. To show this more clearly, d/w in these devices is plotted in Figure 5.8, where the dead-space occupies an increasing fraction of the device width in the thinner devices. Simulations of the excess noise also gave good agreement to the experimental results shown in Figure 5.7(not shown).

To show this more clearly, effective k (as defined by the McIntyre model) is plotted against the nominal i region width, obtained from the experimental measurements and the simulations as illustrated in Figure 5.8. From this figure we can see that the excess noise of the SAM-APD is equivalent to that of a 0.2 µm PIN, despite having a much wider triangular electric field profile as shown in Figure 5.4.

The modelling also shows that in the thinnest PIN structure investigated, the effective k corresponds to 0.15, comparable to a good silicon based APD. A properly designed SAM-APD with a similarly thin avalanching region and a 2 µm thick absorbing region should therefore ensure a device with a high responsivity, low noise and a relatively low operating voltage.

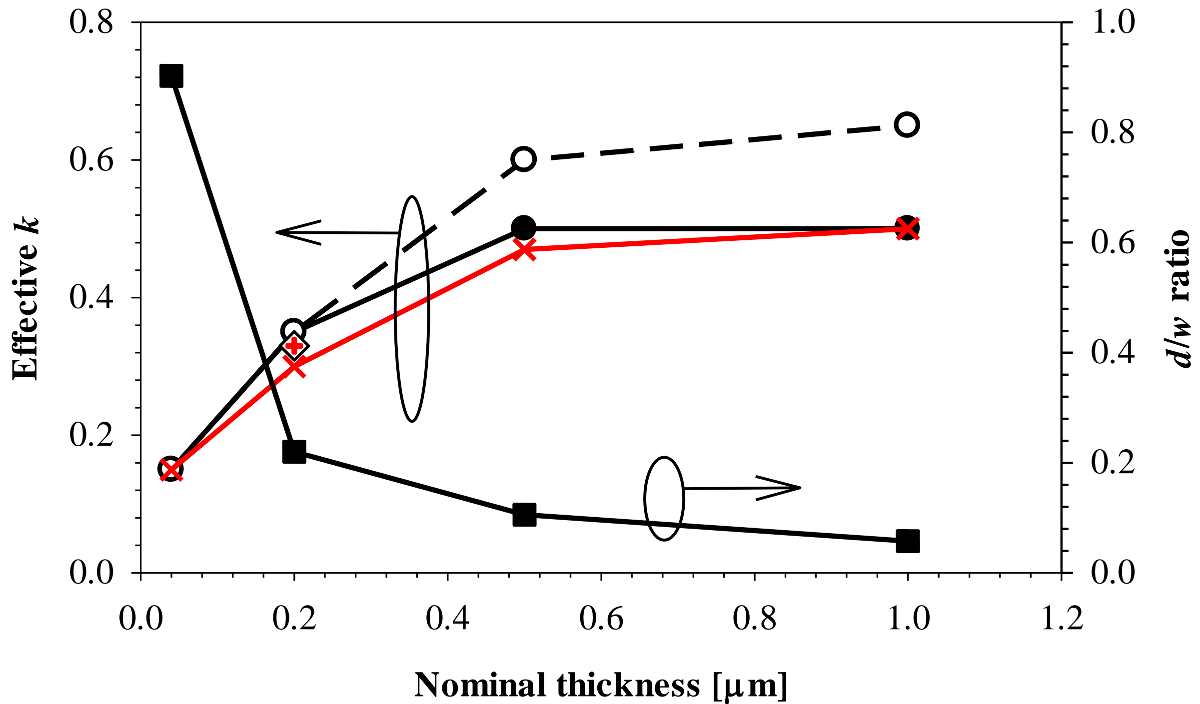

Figure 5.8: k_{eff} versus nominal width using a 442 nm laser (●) and a 460 nm LED (○) for AlInP PIN diodes. The (◊) symbols represent k_{eff} of the SAM-APD by using 460 nm LED. The symbols (× and +) show PIN modelling results by using pure injection and SAM-APD modelling results by using mixed injection respectively. Also shown the calculated *d*/*w* ratio, by taking the highest electric fields attainable in these devices shown in Figure 5.4. Lines are a guide to the eye.

5.7 Summary

The avalanche multiplication and excess noise characteristics of a series of AlInP homo-junction PIN and NIP diodes with *i* region widths ranging from 0.04 µm to 1 µm were investigated using 442 nm laser and 460 nm LED illumination. This work also includes the SAM-APD with a nominal multiplication region width of 0.2 µm which using 460 nm LED. Low dark currents of < 170 nA cm^{-2} at 95% of breakdown voltage were obtained in all the devices because of its wide bandgap and there was no tunnelling dark current present even at high-fields > 1000 kV/cm. The multiplication characteristics measured using 442 nm laser have similar results compared to those using 460 nm LED in both structures.

Very low excess noise in the thinner devices, corresponding to k = 0.32 and k = 0.11, was measured using 442 nm laser and 460 nm LED. These results are quite similar, because the impact ionization coefficients α and β are almost identical over the range of electric fields at high reverse bias in the thin structure. For the thick structure, the excess noise factor of the

mixed injection are higher than the pure electron injection in the PIN structure. The excess noise of the SAM-APD are close to $k = 0.3$ which has a good agreement with the data from the PIN with $w = 0.2$ µm.

The avalanche multiplication and excess noise characteristics were modelled using a RPL model. Good agreement between the simulated multiplication and experimentally determined values, even in thinnest devices where the dead space effect is significant, was obtained. Thinner AlInP structures are expected to give further reductions in excess noise because of the dead space effects. SAM-APD with a thin avalanching region which has a high responsivity, low noise and a relatively low operating voltage has been designed. Such a device with a 0.4 mm diameter (in order to achieve high responsivity) would have a capacitance of ~ 6.2 pF when fully depleted, enabling a RC time constant limited bandwidth of ~ 513 MHz at unity gain, making it suitable for underwater communication applications.

Chapter 6: High temperature performance of AlInP Diodes

6.1 Introduction

APDs are sometimes operated at elevated temperatures for certain applications. The temperature of the environment will affect the gain at high electric fields and the breakdown voltage of the APD, because impact ionisation is temperature dependent. In optical communication systems, the APD is placed at start of the receiver system consequently high temperatures may greatly affect the overall system sensitivity.

The impact ionisation coefficients as a function of temperature can be extracted from the temperature dependence of avalanche multiplication. This is substantially easier if data for pure injection of both carrier types is available, but it is possible with mixed injection and noise data. The excess noise properties are also a function of temperature. The noise is strongly dependent on temperature and is also key factor in determining the sensitivity of the overall system. This information is usually used in the design and optimisation of APDs for operation over a wide range of temperature. Ideally a diode well suited to operation in a wide range of temperatures would have a weak dependence of gain, breakdown voltage and excess noise with temperature.

Ong *et al.* [105] has reported that the temperature dependence of the avalanche multiplication in AlInP from 77 K to 298 K. However, there is limited literature published on the temperature dependence of the excess noise. Kanbe [106] has suggested that the variation of the excess noise in a silicon APD can be neglected. The excess noise of the InGaAs/InP APDs increases from $k = 0.42$ to 0.53 when the temperature varies from 240 K to 360 K [107][108]. Zheng [55] investigated the gain and excess noise of the $Al_xGa_{-x}As$ APD with $x = 0$ to 0.4 and found that there is little variation at temperatures in the range 302 K to 398 K.

In the Chapter 5, AlInP APDs have been shown to provide pure electron multiplication, M_e with very low excess noise factor, F_e at room temperature. There are however no experimental reports of multiplication and excess noise for AlInP at high temperatures (up to 475 K). This chapter presents excess noise and multiplication data obtained from a series of AlInP PIN and NIP diodes with nominal avalanche layer thickness ranging from 0.04 µm to 1.0 µm from

298 K to 475 K and the temperature dependence of the impact ionization coefficients are extracted.

6.2 Layer Details

The structure of the AlInP diodes has been described in section 5.2. There are the three homo-junction PINs and a NIP structure with nominal *i* region widths, *w* of 0.04, 0.5, 1.0, and 0.8 µm, respectively. Details of the AlInP diodes which have been given in Table 5.1 are reiterated in Table 6.1.

Structure	Layer Number	Sample Number	Width (µm)
PIN	MR2827	P2	0.04
PIN	TS5771	P7	0.5
PIN	MR2812	P6	1
PIN	MR2807	N3	0.8

Table 6.1: The structure of the PIN and NIP AlInP diodes .

6.3 IV Measurements

The high temperature IV measurement set-up is similar to the standard IV measurement system except for the hotplate which is used to heat the device up to a maximum temperature of 475 K. The hotplate consists of a 100 W power resistor and high current DC power supply. The diagram of the hotplate is shown in Figure 6.1. The top surface of this resistor was milled flat using a computer numerical control (CNC) milling process and then insulated using thermally conductive PCB. The thermally conductive PCB has three layers, which top and bottom layer are copper plate and middle layer is ceramic powder mix with polymer. The input of the thermometer which is used to measure temperature is connected to the surface of the hotplate. The temperature of the hotplate was control by an analogue DC power supply. Before doing the experiment, there is other infrared thermometer are used to make sure the surface temperature of the hotplate is correct.

The reverse dark IV characteristics measured on the largest size (ϕ = 420 µm) AlInP diodes with w = 0.04, 0.5 and 1 µm at different temperatures from 298 K to 475 K are shown in Figure 6.2, Figure 6.3 and Figure 6.4, respectively. The temperature sensitivity of the dark current in a semiconductor is linked to its bandgap [3]. The dark current of these devices increases with increasing temperature. The dark current in the thinnest device will increase by three orders of

magnitude over the temperature range 298 K to 475 K. For the thickest structure, the dark current increases by four orders of magnitude from room temperature to 475 K. There is no tunnelling current observed even in the thinnest (w = 0.04 µm) device structure at high temperature due to the large band-gap of AlInP.

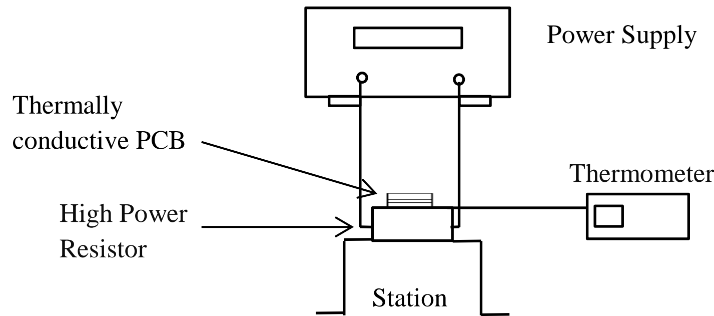

Figure 6.1: The diagram of the hotplate set-up.

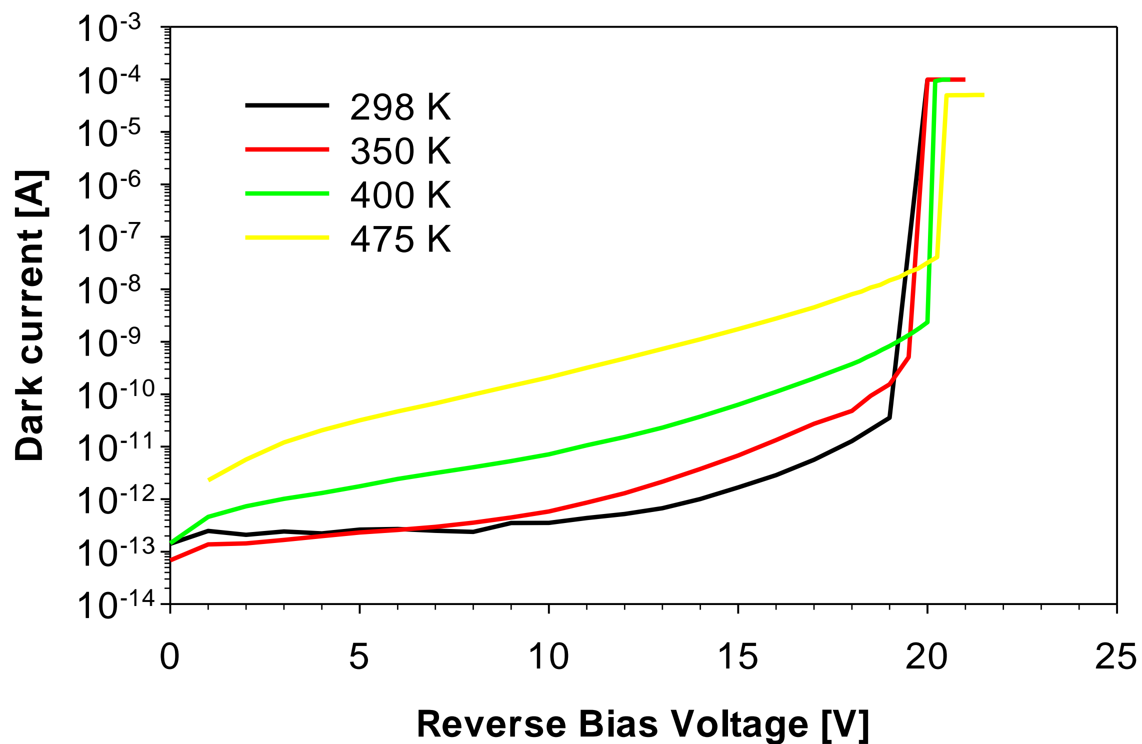

Figure 6.2: Measured reverse dark current characteristics of 200 µm radius PIN diode P2 with i = 0.04 µm and NIP diodes at (black) 298, (red) 350, (green) 400, (yellow) 475 K.

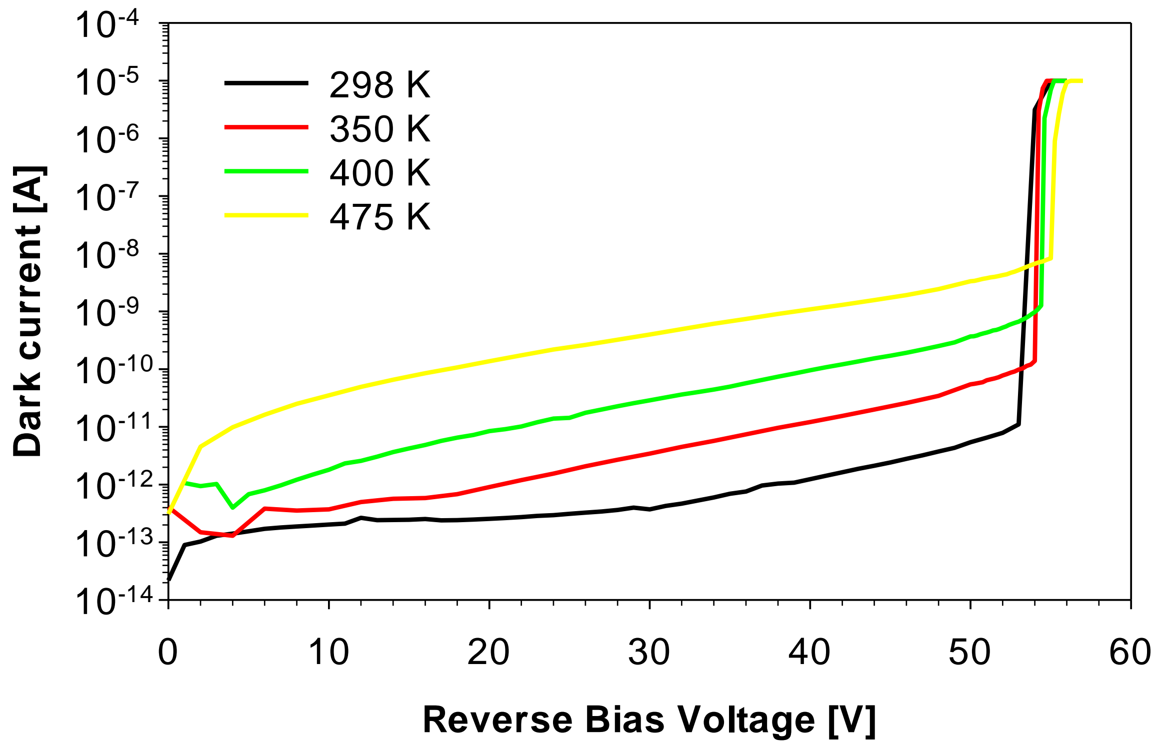

Figure 6.3: Measured reverse dark current characteristics of 200 µm radius PIN diode P7 with i = 0.5 µm and NIP diodes at (black) 298, (red) 350, (green) 400, (yellow) 475 K.

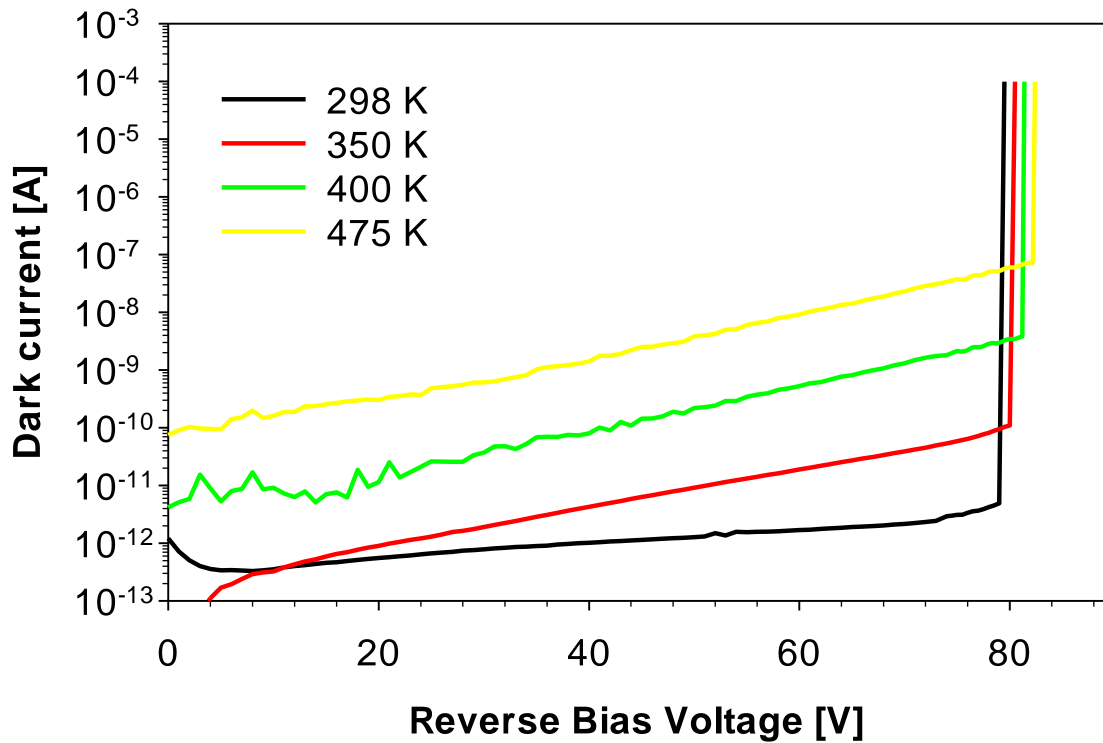

Figure 6.4: Measured reverse dark current characteristics of 200 µm radius PIN diode P6 with i = 1 µm and NIP diodes at (black) 298, (red) 350, (green) 400, (yellow) 475 K.

6.4 CV Measurements

The capacitance-voltage (C-V) measurement was performed on MR2812 at 298 K and 475 K. A comparison of the C-V at 298 K and 475 K is shown in Figure 6.5. The value of capacitance at different temperatures is similar (less than 2 % difference). Therefore, the depletion region, w of the device is a weak function of temperature.

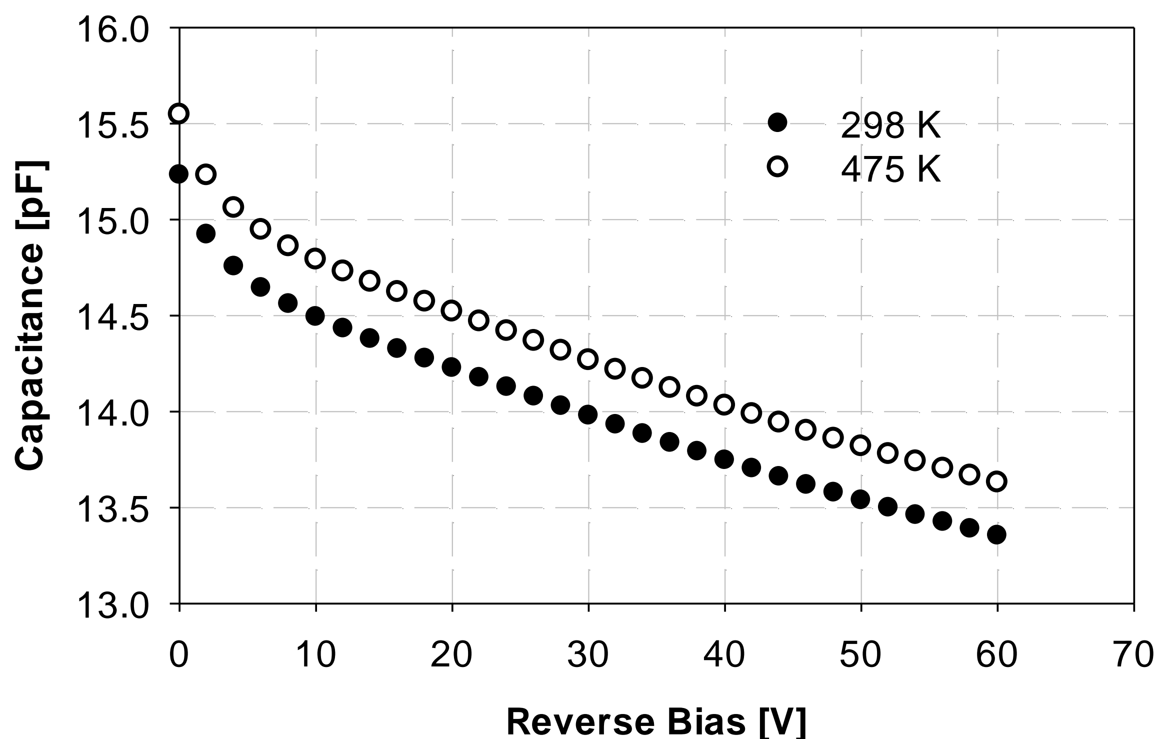

Figure 6.5: Capacitance versus reverse bias of the MR2812 at 298 K (closed symbols) and 475 K (open symbols).

6.5 Photomultiplication Characteristics

Photomultiplication measurements were performed by probing the device on the hotplate which is controlled by the power supply. There are four structures of AlInP diodes, MR2827, TS5771, MR2812 and MR2807 were used in the photomultiplicaiton measurement. The multiplication has been measured as a function of temperature from 298 K to 475 K by using a 442 nm He-Cd laser. Measurements were performed using the phase sensitive detection (PSD) technique in order to differentiate the photocurrent from the dark current at higher electric fields. Measurements have been performed on several different devices to make sure they are reproducible. In order to obtain accurate sample temperature, the experiments were only conducted after the temperature of the device was stabilised at a constant value for at least 5 minutes.

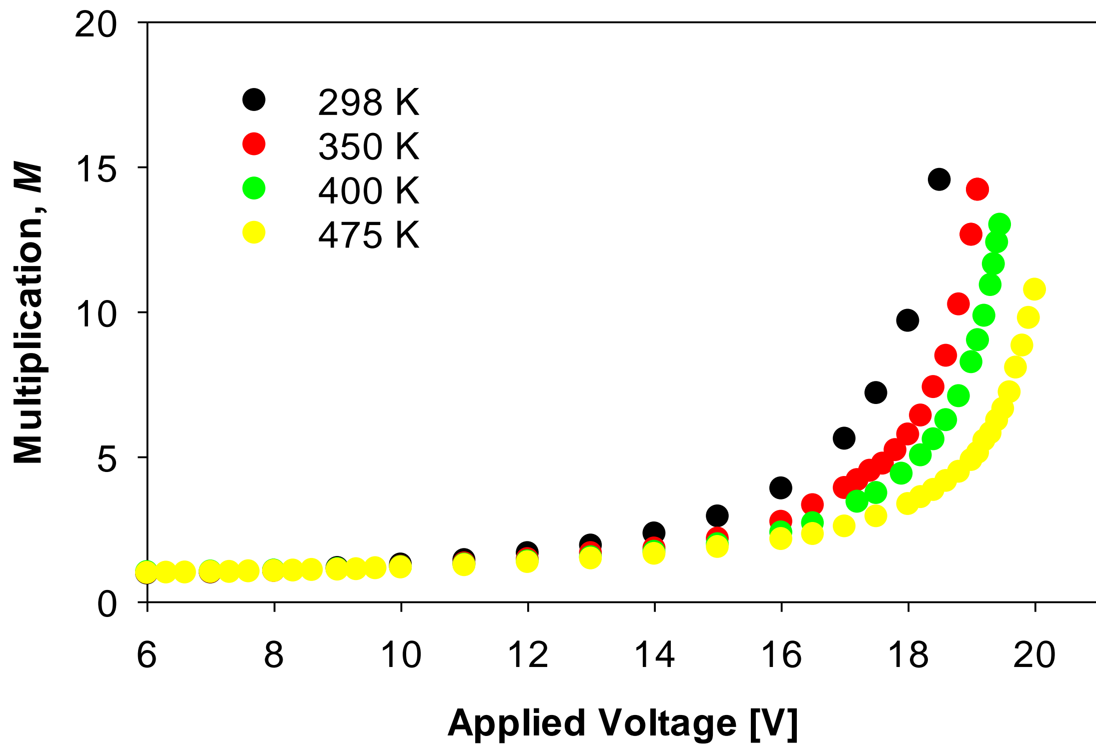

Figure 6.6 (a)

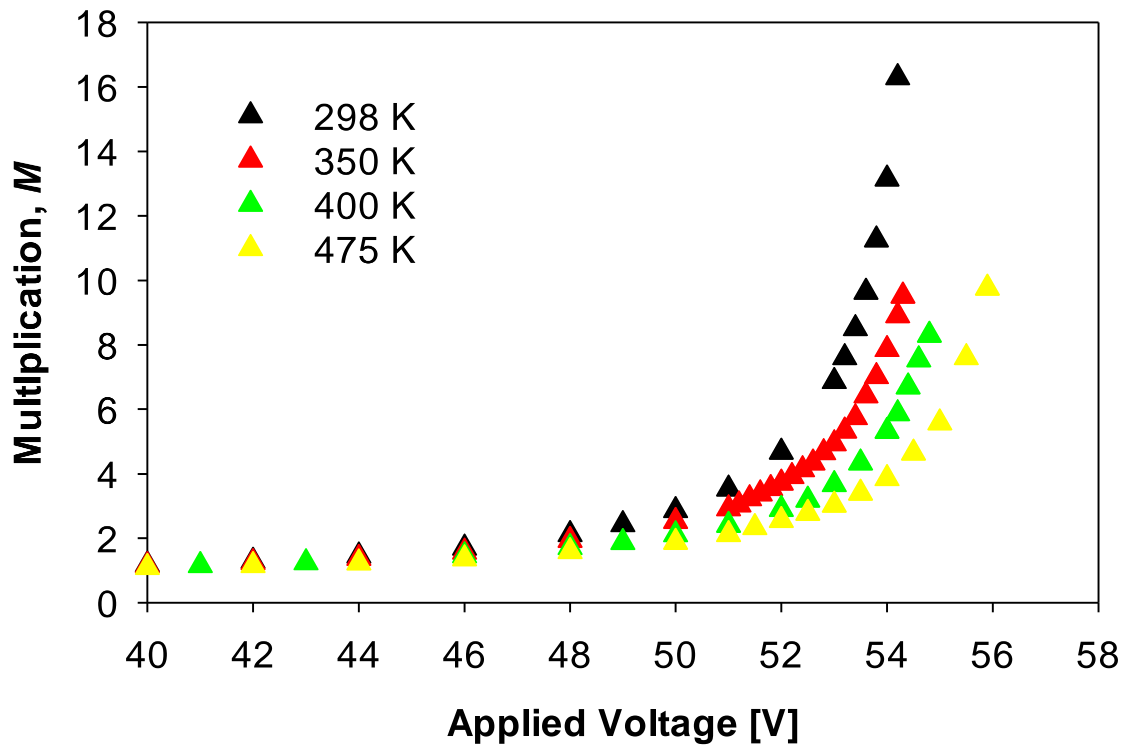

Figure 6.6 (b)

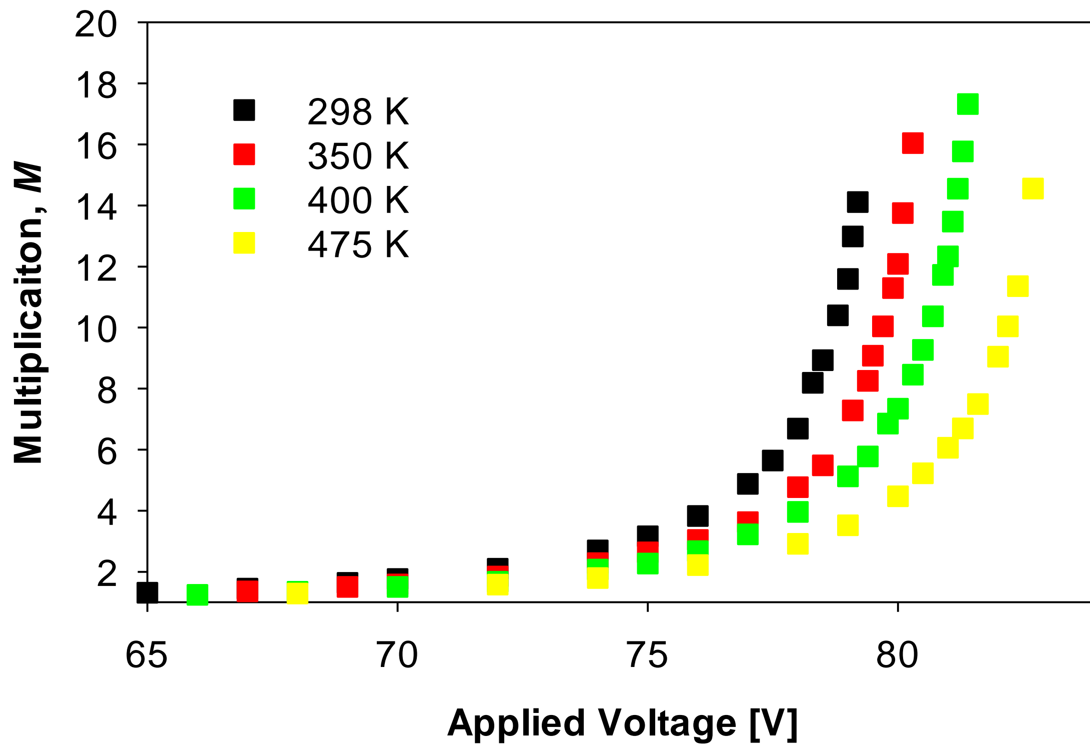

Figure 6.6 (c)

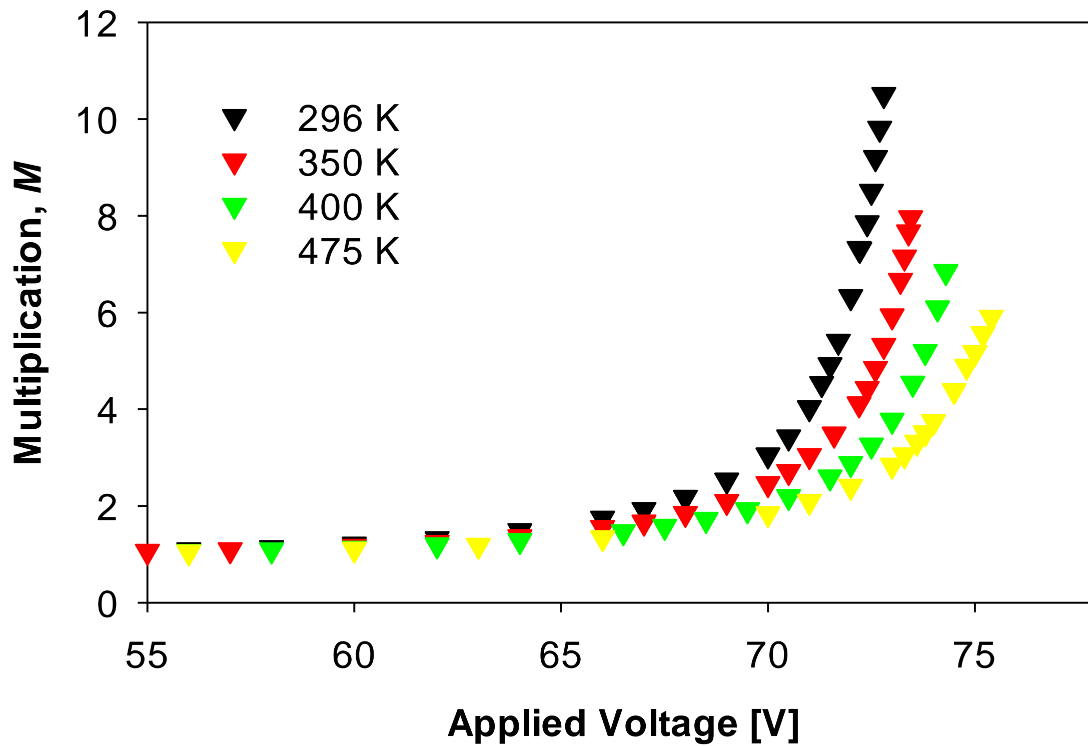

Figure 6.6 (d)

Figure 6.6: Pure electron initiated multiplication of (a) MR2827 (circle), (b) TS5771 (triangle up), (c) MR2812 (square) and (d) MR2807 (triangle down) at (black) 298 K, (red) 350 K, (green) 400 K, (yellow) 475 K using 442 nm laser.

The details of the absorption profile for 442 nm and 480 nm light in AlInP are available in the literature [101]. 442 nm provides pure electron (or hole) initiated multiplication in all of the structures in this chapter. Figure 6.6 shows pure electron initiated multiplication, M_e of all these devices increases for a given applied voltage when the temperature increases from 298 K to 475 K. The reason is when the temperature increased the charge carriers interact more often with the semiconductor crystal lattice. The mean carrier energy decreases, and this reduces the probability of impact ionization events. Therefore somewhat higher bias voltage is required to obtain the same avalanche breakdown condition and impact ionization rate.

6.6 Excess Noise Measurements

6.6.1 High Temperature Excess Noise Set-up

During this work, the excess noise factor of AlInP APDs was measured at high temperatures (up to 475 K). The high temperature excess noise set-up is very similar to the Lau's system [18] which was described in chapter 3. However, the maximum working temperature of the excess noise circuit components is no more than 375 K. Since the front end (TIA) circuit board is used to support the diced wafer the temperature limit of the front end components also limits the APD die temperature. A design of noise measurement system capable of measuring the excess noise factor at higher temperatures was needed. This necessitates removing the front end electronics from its role as mechanical support for the device in order to provide thermal insulation and thereby allow the device temperature to be raised. To accomplish this a "two probe" system is used, because it provides the separation of the hotplate and front-end circuits.

The structure of the measurement system is shown in Figure 6.7. In Figure 6.7, the wire wound aluminium clad power resistor was used to as a hotplate to heat up the device. The hotplate has been described in section 6.3. It is difficult to increase the distance between the device and the transimpediance amplifier (TIA), because the parasitic input capacitance is increased by using second probe and the associated cabling. This limits the excess noise circuit because it effectively increases the input capacitance, meaning a lower range of APD capacitance can be accommodated compared to a room temperature single probe system made from the same front end circuit components. In the case of the two probe system the input capacitance should not exceed 56 pF to avoid front-end oscillation.

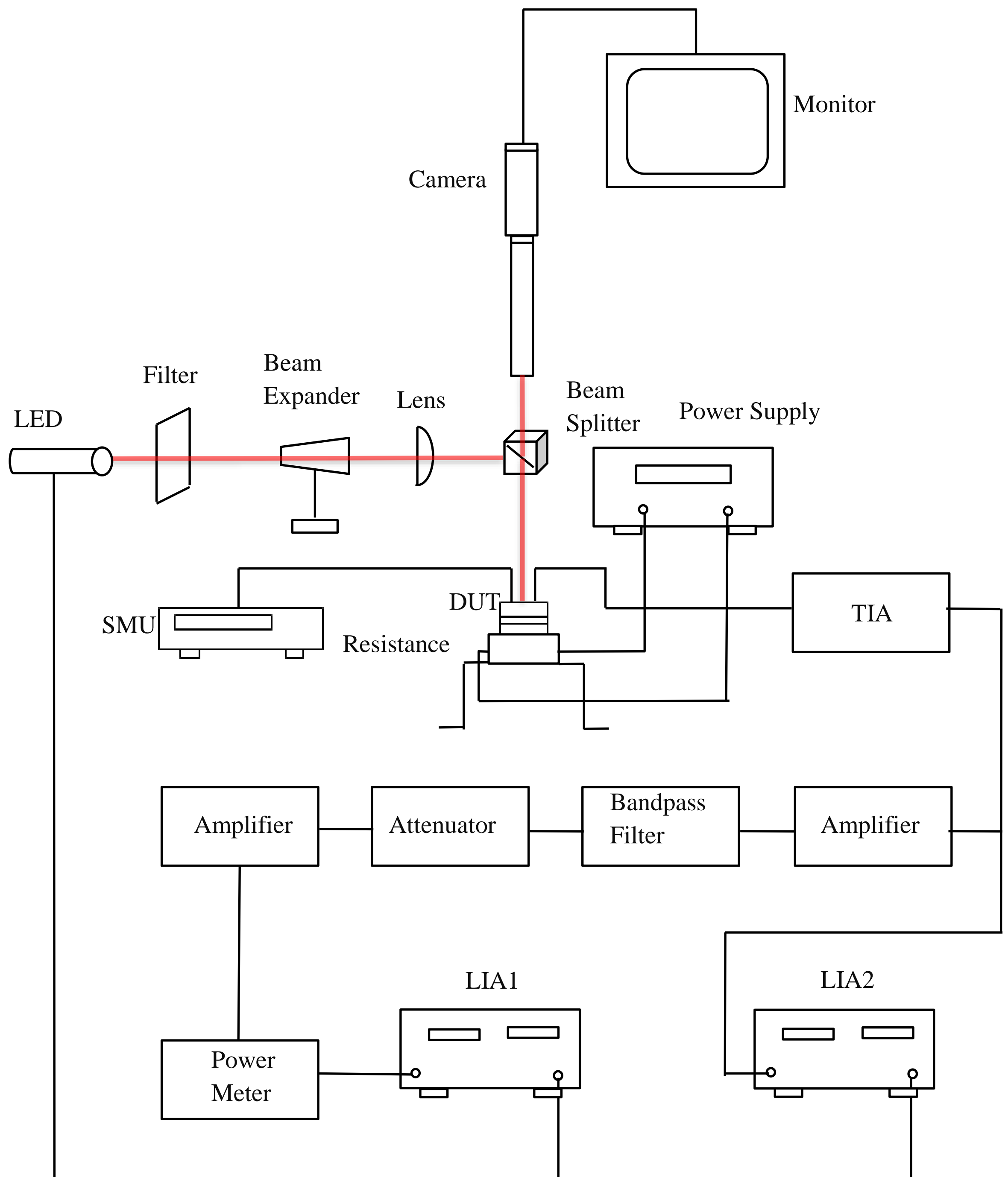

Figure 6.7: A block diagram of the high temperature noise measurement system.

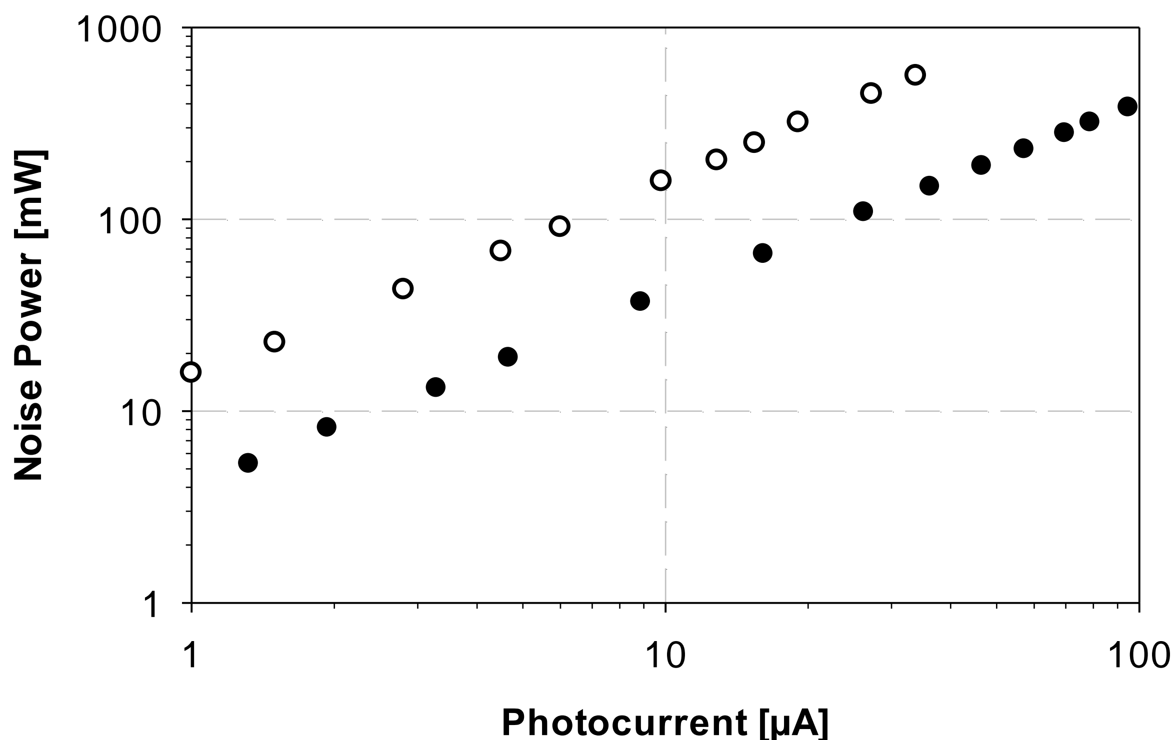

Figure 6.8: Noise power vs Photocurrent on BPX65. Open symbol represents the two probes measurement system and closed symbol shows the single probe measurement system.

The calibration (noise power vs photocurrent) has been measured using a BPX65 silicon device. The value of the a from the (4.12) of the single probe and the two probe measurement are different, because the second probe adds capacitance to the measurement which artificially increases the measurement bandwidth. In Figure 6.8, the gradient (two probes) is equal to 7.67. Therefore the noise measured depends on the probe cable capacitance.

6.6.2 Results

The excess noise factor of MR2827, TS5771, MR2812 and MR2807 were measured from 298 K to 475 K using the excess noise setup which has been described in the last section. Mixed injection was achieved by using a 460 nm LED shone onto the devices. This is the result of a portion of the longer wavelengths emitted by the LED being absorbed within the depletion region.

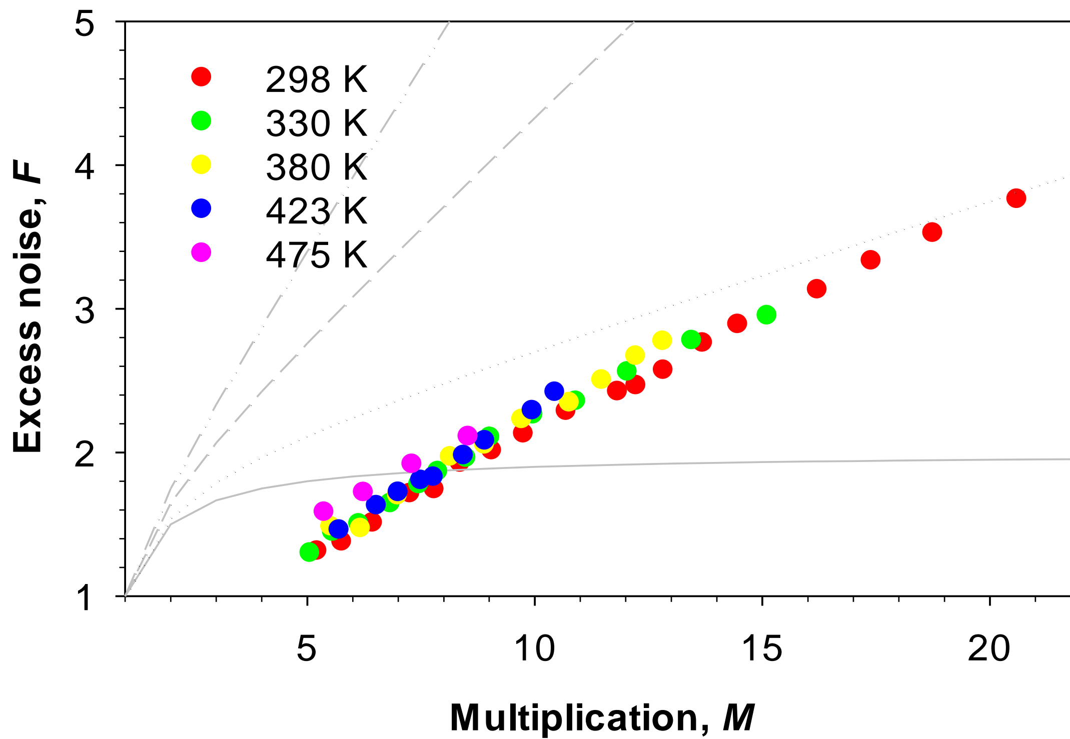

Figure 6.9: Excess noise measured on MR2827 at (red) 298, (green) 330, (yellow) 380, (blue) 423 and (pink) 475 K under 460 nm LED illumination. Grey lines are McIntyre's curves with $k = 0$, 0.1, 0.3 and 0.5.

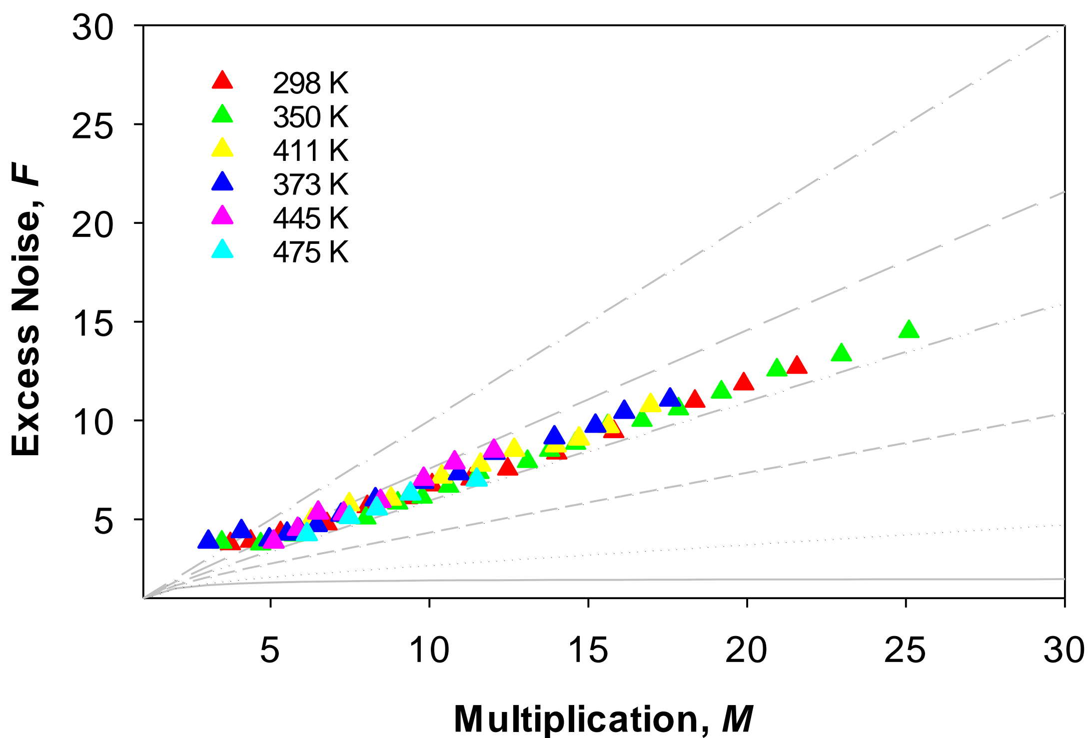

Figure 6.10: Excess noise measured on TS5771 at (red) 298, (green) 350, (blue) 373, (yellow) 411, (pink) 445 and (cyan) 475 K under 460 nm LED illumination. Grey lines are McIntyre's curves with $k = 0$, 0.1, 0.3, 0.5, 0.7 and 1.

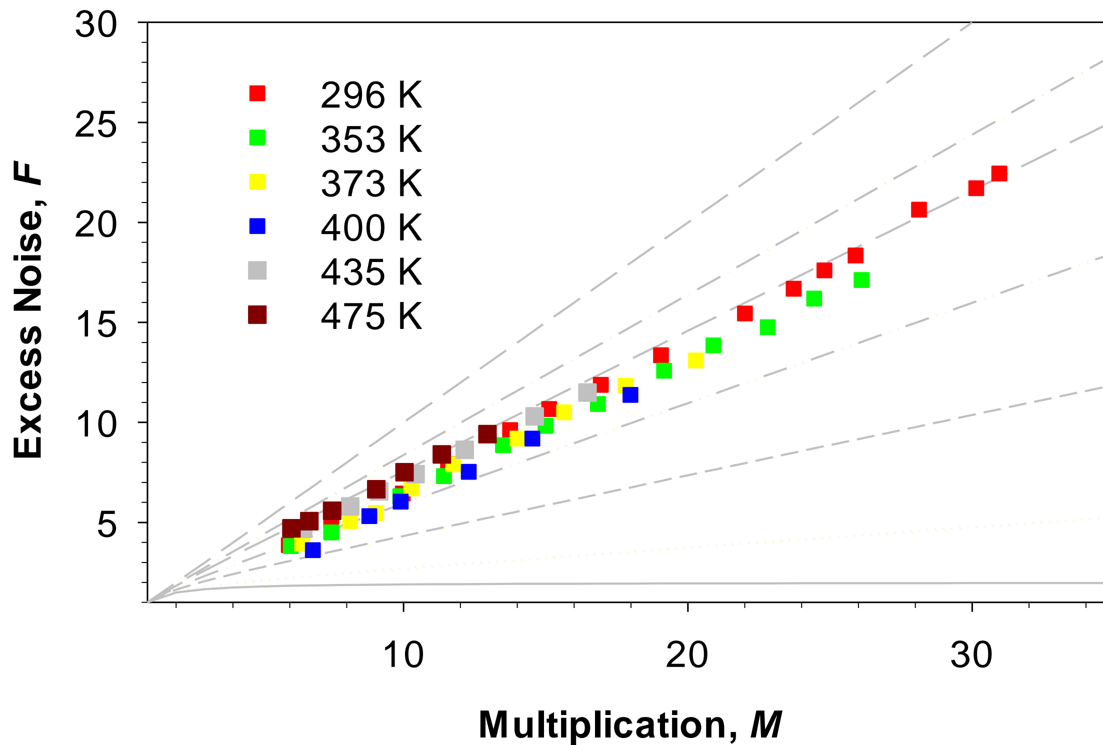

Figure 6.11: Excess noise measured on MR2812 at (red) 298, (green) 353, (yellow) 373, (blue) 400, (pink) 435 and (cyan) 475 K under 460 nm LED illumination. Grey lines are McIntyre's curves with k = 0, 0.1, 0.3, 0.5, 0.7, 0.8 and 1.

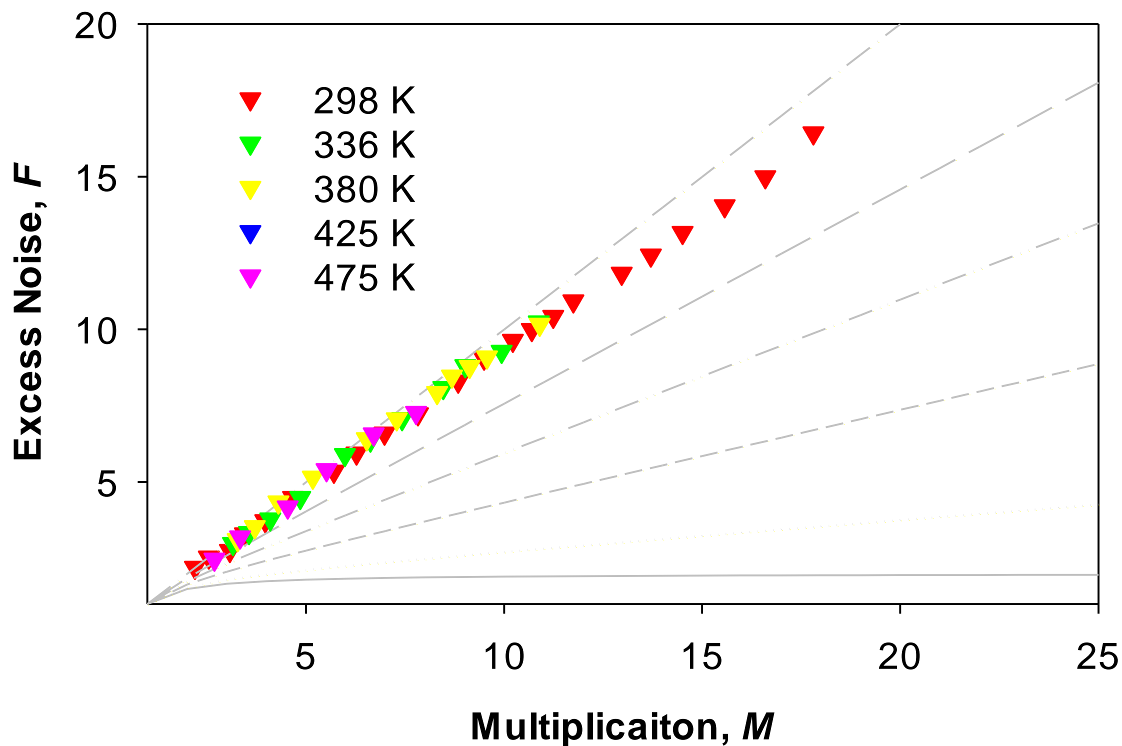

Figure 6.12: Excess noise measured on MR2807 at (red) 298, (green) 336, (yellow) 380, (blue) 425 and (pink) 475 K under 460 nm LED illumination. Grey lines are McIntyre's curves with k = 0, 0.1, 0.3, 0.5, 0.7 and 1.

Figure 6.9, Figure 6.10, Figure 6.11 and Figure 6.12 show the excess noise characteristics for the AlInP PIN and NIP structures using 460 nm LED illumination from 298 K to 475 K. The grey lines correspond to the McIntyre noise theory based on the β/α (k) ratio. The excess noises at room temperature results are similar to those reported in chapter 5.

The excess noise characteristics of all AlInP diodes obtained from 298 K to 475 K were similar, indicating that the high temperature did not significantly affect the excess noise factor. In the thickest PIN structure (1 µm), the excess noise increase to levels corresponding to k = approximaely 0.65. The excess noise decreases with reducing avalanche depletion width, because carrier dead space increases significance [40][42], so the excess noise decrease to levels corresponding to $k = 0.6$ and $k = 0.11$, in the 0.5 µm and 0.04 µm structures respectively. In the very thin device, the excess noise will not follow the McIntyre model, because the dead space becomes important. Li [40] has reported that excess noise of the GaAs with 0.05 µm depletion region shows a similar behaviour. For the NIP thickest structure, the excess noise stays constant which is corresponding to $k = 0.9$ when the temperature varies.

The excess noise of the PINs and a NIP AlInP devices with nominal i region widths, w of 0.04, 0.5, 1, and 0.8 µm from 298 K to 475 K are similar to the excess noise results which has been described in Chapter 5.

It is difficult to get excess noise factor in the high multiplication (more than 15) at high temperatures (approximately 475 K), because the dark current increases to a very high level near to breakdown. As the temperature increases the measurement system and non-photo-generated noise processes in the APD start to swamp the measurement. For instance, in Figure 6.13, the dark current is around 10 µA when the multiplication is less than 12.

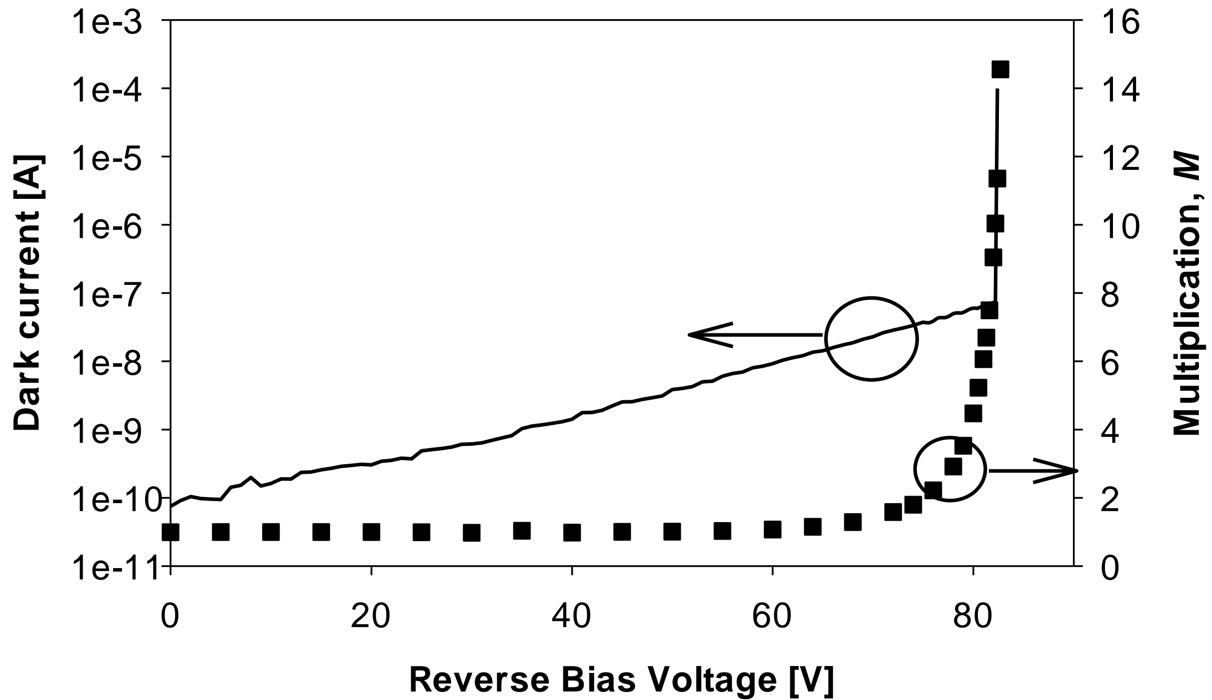

Figure 6.13: The dark current (black line) and multiplication (square) measurement performed on the MR2812 at 475 K.

6.7 Modelling Results

6.7.1 Effective Impact Ionisation Coefficients

The details of absorption profiles for 442 nm and 480 nm wavelength photons in AlInP have been described [101]. 442 nm wavelength can give pure electron (or hole) initiated multiplication. For the 460 nm emission from the LED, this can provide a significant mixed carrier multiplication characteristic. Impact ionization coefficients, α and β can be obtained from measured pure electron multiplication and measured pure hole multiplication using local model when the depletion region can be accurately estimated and dead space effects are ignored. α and β in a given depletion region, w, are insensitive to the measured M_e and M_h in the low multiplication factor.

In this work, α and β were deduced from the measured pure injection multiplication of the MR2812 and MR2807, respectively, because these diodes have thick depletion region and fairly uniform electric field. Therefore, assume the electrical field profile of MR2812 and MR2807 is ideal PIN (NIP) structure. Equation (6.1) and (6.2) which has been described in chapter 2 are solved to eliminate the α and β at room temperature.

$$\alpha = \frac{1}{w_T}\left(\frac{M_e - 1}{M_e - M_h}\right)\ln\left(\frac{M_e}{M_h}\right) \tag{6.1}$$

and

$$\beta = \frac{1}{w_T}\left(\frac{M_h - 1}{M_e - M_h}\right)\ln\left(\frac{M_e}{M_h}\right) \tag{6.2}$$

Since NIP and PIN do not have identical widths, 0.8 μm was used to initially estimate α and β. The α and β obtained in this way was adjusted until a good fit to the 0.8 μm and 1 μm measured multiplication results were obtained. The methods were repeated here for different temperature up to 475 K to obtain impact ionization coefficients as a function of temperature. In order to obtain the impact ionisation coefficients of the AlInP material, the exponential form of α and β are given by,

$$\alpha = A_1 \exp((-\frac{B_1}{\zeta})^{C_1}) \text{ cm}^{-1} \tag{6.3}$$

and

$$\beta = A_2 \exp((-\frac{B_2}{\zeta})^{C_2}) \text{ cm}^{-1} \tag{6.4}$$

Where A_1, B_1, C_1, A_2, B_2 and C_2 are constants. The estimated α and β at different temperature are shown in Figure 6.14. The parameterized ionization coefficient α and β from 298 to 475 K which covering an electric field range from 435 kVcm^{-1} to 990 kVcm^{-1} are given by

$$\alpha = 4.93 \times \exp((-\frac{1.65\times10^6 + 400(T-298)}{\zeta})^{1.78})cm^{-1} \tag{6.5}$$

and

$$\beta = 5.28 \times \exp((-\frac{1.59\times10^6 + 400(T-298)}{\zeta})^{1.98})cm^{-1} \tag{6.6}$$

Where T is the temperature and ζ is the electric field.

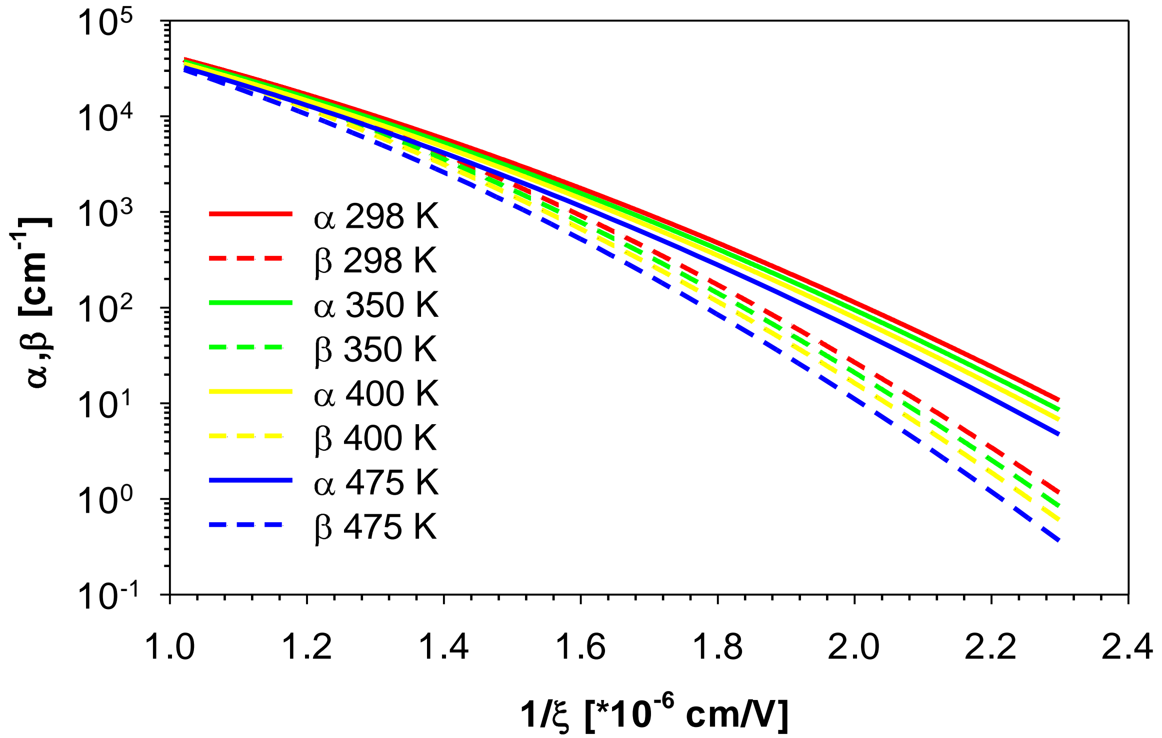

Figure 6.14: Parameterised α (solid lines) and β (dashed lines) of AlInP devices at temperatures from 298 K to 475 K.

The parameterized the temperature dependence of impact ionization coefficients are slightly different from those published earlier because the ionization coefficients were calculated using the random-path length (RPL) model [100] which includes the dead space effect. It is necessary to investigate the multiplication and excess noise characteristics of the AlInP devices in order to utilise the ionization coefficient α and β over the operating temperature range from 298 K to 475 K during designing the APDs. Figure 6.14 shows the value of the ionization coefficients reduce when the temperature increases. Also, the ratio of the β/α did not significantly change with temperature. The excess noise factor (F) was described by McIntyre [17] as

$$F(M) = kM + (2 - \frac{1}{M})(1 - k) \quad (6.7)$$

where $k = \beta/\alpha$ for the case of pure electron initiated multiplication. According to the equation (6.7) the excess noise factor depends on the ratio of the ionization coefficients and the excess noise factors of the AlInP diodes from 298 K to 475 K are similar.

6.7.2 Modelling Multiplication Results

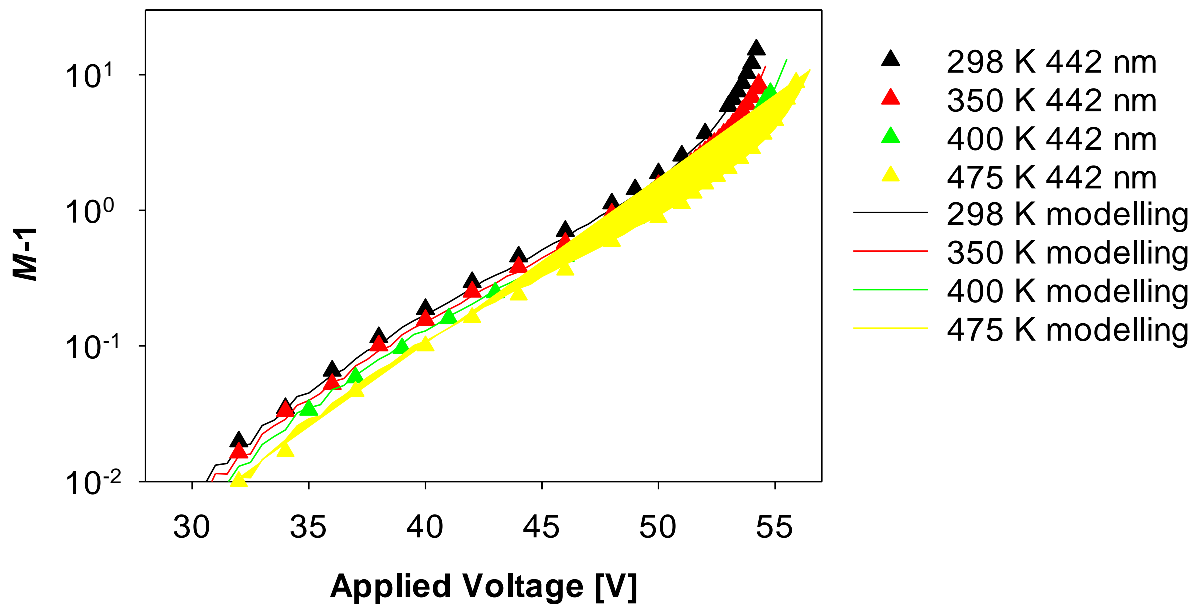

Figure 6.15 (a)

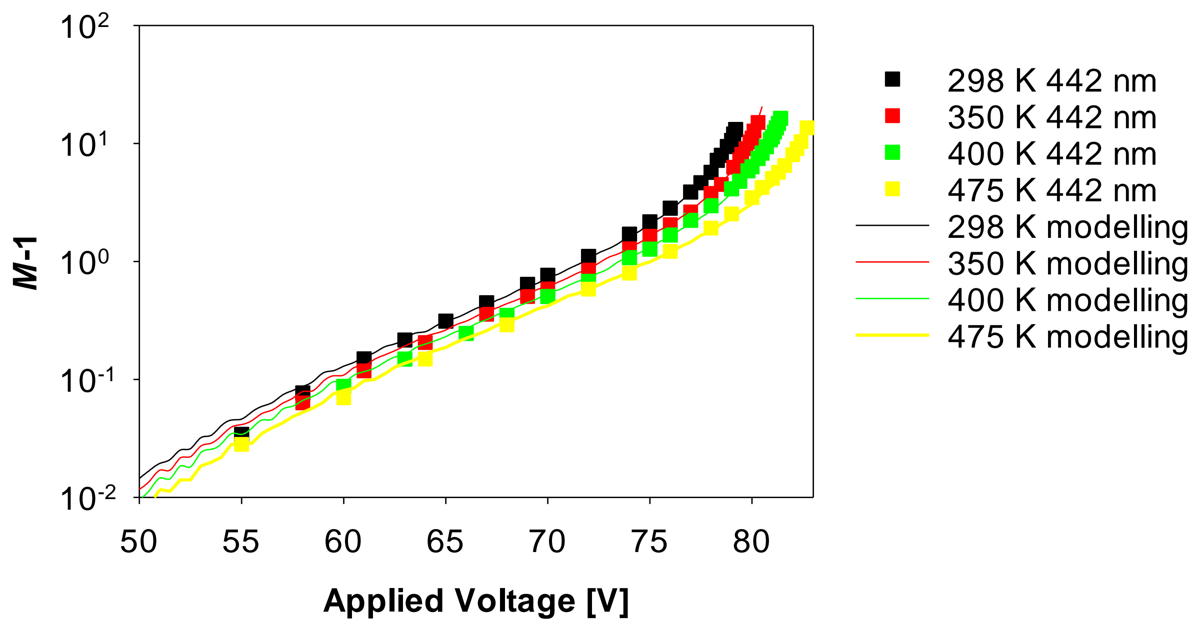

Figure 6.15 (b)

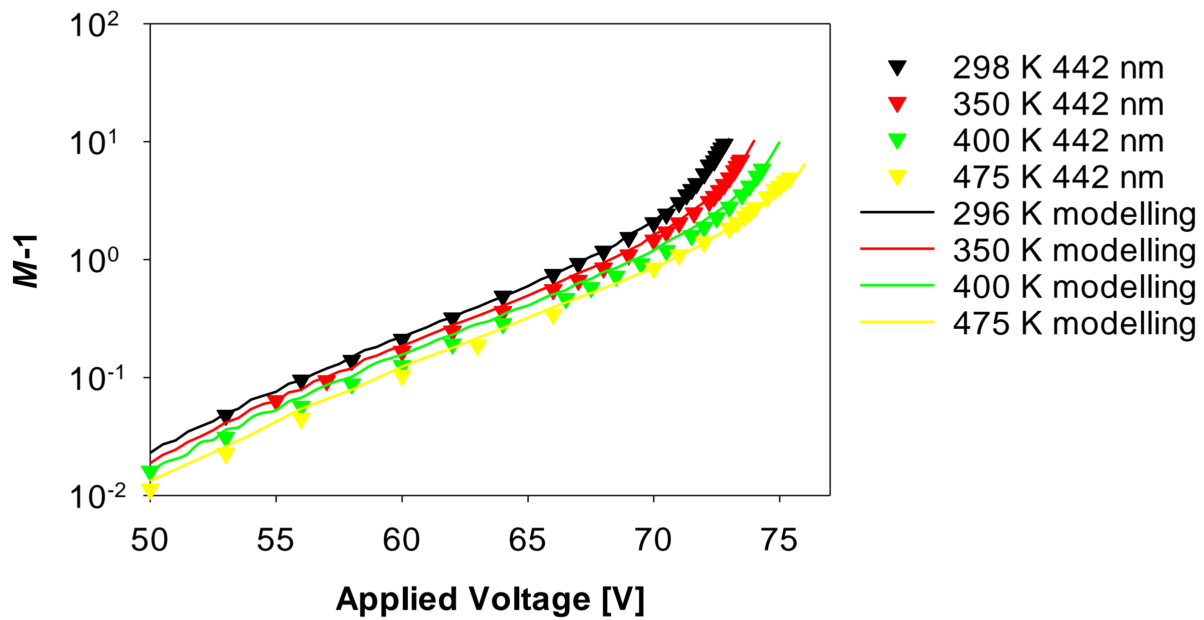

Figure 6.15 (c)

Figure 6.15: Experimental M-1 versus reverse voltage for (a) TS5771 (triangle up, (b) MR2812 (square) and (c) MR2807 (triangle down) at (black) 298, (red) 350, (green) 400, (yellow) 475 K using 442 nm laser. The solid line shows modelled results which was calculated from parameterised α and β of this work.

The measured multiplication results which emphasize the low field multiplication characteristics from 298 K to 475 K are shown in Figure 6.15. The avalanche multiplication with a particular w at a given temperature was calculated using the RPL model which has been described in chapter 5 based on the temperature dependence of parameterized ionization coefficient which is given in (6.5) and (6.6), respectively. The solid lines in Figure 6.15 show that the simulated multiplication has a good agreement with experimentally determined values over a wide dynamic range from 298 K to 475 K.

6.8 Summary

The temperature dependence of the avalanche multiplication and excess noise from 298 K to 475 K have been measured on three AlInP PIN and a NIP with nominal *i* region widths, *w* from 0.04 to 1 µm under 460 nm LED illumination. The impact ionisation coefficients from 298 K to 475 K cover the electric field range from 435 kVcm^{-1} to 990 kVcm^{-1}. Compared to the hole, the electron is the readily ionising carrier type. The excess noise of the AlInP diodes at different temperatures (from 298 K to 475 K) are very similar. For the thin AlInP diode, the low dark currents, low excess noise and low temperature coefficient of impact ionisation shows that it is well suited to production of temperature insensitive APDs.

Chapter 7: Conclusion and proposed further work

7.1 Conclusion

This thesis has provided the multiplication and excess noise characteristics of the $Al_xGa_{1-x}InP$ and AlInP devices at room temperature in chapters 4 and 5. The temperature dependence of the impact ionization coefficient, multiplication and excess noise in AlInP devices has been described in chapter 6. The $Al_xGa_{1-x}InP$ excess noise data has been gathered using a newly designed excess noise measurement system described in chapter 4 and a two probe high temperature measurement system described in chapter 6 was used to measure temperature dependence characteristics in AlInP devices.

This work is successful and the versatile system for measuring multiplication and excess noise has been reported or is in the process of being reported. This system can measure the multiplication and excess noise of APDs even when the primary photocurrent is around 10 nA which is more than one order of magnitude better than Lau's system [18]. Also, the SNR of this system is at least two orders of magnitude higher than the prior published measurement systems. The excess noise factor can be measured using this system on photodiodes with junction capacitance up to approximately 22 pF. This range still covers the capacitance of interest for the majority of APD detectors.

Excess noise measurements have been performed on a series of AlInP homo-junction PIN and NIP diodes with *i* region widths ranging from 0.04 µm to 1 µm. This work also includes the SAM-APD with a nominal multiplication region width of 0.2 µm. The objective of this work represents the first reported excess noise factor in AlInP devices and there was no tunnelling dark current present even at high-fields is more than 1000 kV/cm due to its wide bandgap material. In the thinner devices (w = 0.04 µm and w = 0.2 µm), the excess noise is corresponding to $k = 0.11$ and $k = 0.32$, respectively. The excess noise of the SAM-APD are close to $k = 0.3$ which has a good agreement with the data from the PIN with w = 0.2 µm. The experimental multiplication and excess noise have good agreement with simulated results which using a RPL model even the dead space is significant. Excess noise can be further reduced in the thinner structure because of the dead space effect. A SAM-APD with a thin avalanching region obtains a high responsivity, low noise and a relatively low operating voltage.

This SAM-APD with a 0.4 mm diameter (in order to achieve high responsivity) would have a capacitance of approximately 6.2 pF when fully depleted and it is suitable for underwater communication applications.

This work also reports the temperature dependence of the multiplication and excess noise on a range of AlInP devices. These devices have depletion region, w from 0.04 to 1 µm. The impact ionisation of the electron and hole, α and β have been extracted based on the multiplication data over the temperature range 298 K to 475 K. The experimental data shows the excess noises of the AlInP diodes are very similar at different temperatures. This shows that the AlInP diodes can be designed for the temperature insensitive APDs.

7.1 Proposed further work

1. One objective of this thesis is to develop excess noise measurement system for characterisation of avalanche photodiode diodes. The new excess noise measurement system in chapter 4 is able to measure the noise power with 10 nA input optical power. Chapter 4 reported that it is difficult to obtain shot noise power with 1 nA input current because there is only 2.5 pA_{RMS} noise current relevant to the noise. However, this system can still be improved a little (7 - 9 nA) depending on the design time available and relaxation of cost limitations. The gain of the power amplifier which is after attenuator can increase to the high level. Secondly, need to design a PCB with the low value of the parasitic capacitance (less than 0.05 pF) in order to get higher cut-off frequency of the system. Thirdly, the measurement system may be placed in a low temperature environment to reduce the thermal noise.

2. The multiplication and excess noise of the $Al_xGa_{1-x}InP$ at room temperature has been reported in chapter 4. The impact ionisation coefficients of the $Al_xGA_{1-x}InP$ can be extracted based on the pure injection multiplication experiment results. The impact ionisation coefficients may be used to model the excess noise of the $Al_xGa_{1-x}InP$. The modelling results can describe the multiplication and the excess noise characteristics of the $Al_xGa_{1-x}InP$ diodes and also explain the dominant factor controlling the multiplication and the excess noise if the modelling results have good agreement with experimental data.

3. Chapter 6 shows the temperature dependence characteristics of AlInP. The excess noise of AlInP diodes can be modelled in the range of high temperature in the function

of temperature based on the RPL model. The dominant factor affecting the temperature dependence characteristics in this material can be found if the modelling results can be matched to the experimental data for the multiplication and excess noise.

Reference

[1] B. G. Streetman and S. K. Banerjee, *Solid State Electronic Devices*. New Jersey: Pearson Education Ltd., 2000.

[2] "Electromagnetic Spectrum." [Online]. Available: https://sites.google.com/site/chempendix/em-spectrum.

[3] S. M. Sze, *Physics of Semiconductor Devices*, Second Ed., vol. 10. 1981.

[4] E. Muñoz, E. Monroy, J. a. Garrido, I. Izpura, F. J. Sa, and E. Calleja, "Photoconductor gain mechanisms in GaN ultraviolet detectors," *Appl. Phys. Lett.*, vol. 71, no. 7, pp. 870–872, 1997.

[5] D. Neamen, *Semiconductor Physics and Devices: Basic Principles 4th ed*, Fourth. Elizabeth A. Jones, 2011.

[6] C.-H. Liu, Y.-C. Chang, T. B. Norris, and Z. Zhong, "Graphene photodetectors with ultra-broadband and high responsivity at room temperature," *Nat. Nanotechnol.*, vol. 9, no. 4, pp. 273–278, 2014.

[7] R. L. Petritz, "Theory of photoconductivity in semiconductor films," *Phys. Rev.*, vol. 104, no. 6, pp. 1508–1516, 1956.

[8] Thorlab, "PbS and PbSe Photoconductive Detectors." [Online]. Available: https://www.thorlabs.com/newgrouppage9.cfm?objectgroup_id=9020.

[9] H. Iams and B. Salzberg, "The Secondary Emission Phototube," *Proc. Inst. Radio Eng.*, vol. 23, no. 1, pp. 55–64, 1935.

[10] Hamamatsu, "Photomultiplier Tubes: Basics and Applications." [Online]. Available: http://www.hamamatsu.com/resources/pdf/etd/PMT_handbook_v3aE.pdf.

[11] R. H. Hadfield, "Single-photon detectors for optical quantum information applications," *Nat. Photon.*, vol. 3, no. 12, pp. 696–705, 2009.

[12] K. K. Hamamatsu Photonics, "Photomultiplier Tubes: Basics and Applications," 2007.

[13] Hamamatsu, "Thermoelectric cooled NIR-PMT unit." [Online]. Available:

https://www.hamamatsu.com/resources/pdf/etd/H10330C-25_-45_-75_TPMO1056E.pdf.

[14] G. E. Stillman and C. M. Wolfe, "Avalanche Photodiodes," in *Semiconductors and Semimetals*, R. K. Williardson and A. C. Beer, Ed. New York: Academic Press, 1977, pp. 291–393.

[15] J. C. Campbell *et al.*, "Recent advances in avalanche photodiodes," *IEEE J. Sel. Top. Quantum Electron.*, vol. 10, no. 4, pp. 777–787, 2004.

[16] A. Biber, P. Seitz, and H. Jäckel, "Avalanche photodiode image sensor in standard silicon BiCMOS technology," *Sensors Actuators, A Phys.*, vol. 90, no. 1–2, pp. 82–88, 2001.

[17] R. J. McINTYRE, "Multiplication Noise in Uniform Avalanche Diodes," *IEEE Trans. Electron Devices*, vol. ED-13, no. 1, pp. 164–168, 1966.

[18] K. S. Lau *et al.*, "Excess noise measurement in avalanche photodiodes using a transimpedance amplifier front-end," *Meas. Sci. Technol.*, vol. 17, no. 7, pp. 1941–1946, 2006.

[19] W. Sun, Y. Fu, Z. Lu, and J. Campbell, "Study of bandwidth enhancement and non-linear behavior in avalanche photodiodes under high power condition," *J. Appl. Phys.*, vol. 113, no. 4, 2013.

[20] T. D. D. B. Glenn, S.M. and and W. B. Parker, "Long-term real-time coastal ocean observation networks," *Oceanogr.,* vol. 13, no. 1, pp. 24–34, 2000.

[21] "Underwater Acoustic Sensor Networks (UW-ASN)." [Online]. Available: http://www2.ece.gatech.edu/research/labs/bwn/UWASN/.

[22] I. F. Akyildiz, D. Pompili, and T. Melodia, "Underwater acoustic sensor networks: Research challenges," *Ad Hoc Networks*, vol. 3, no. 3, pp. 257–279, 2005.

[23] E. M. Sozer, M. Stojanovic, and J. G. Proakis, "Underwater acoustic networks," *IEEE J. Ocean. Eng.*, vol. 25, no. 1, pp. 72–83, 2000.

[24] P. Lacovara, "High-Bandwidth Underwater Communications," *Mar. Technol. Soc. J.*, vol. 42, no. 1, pp. 93–102, 2008.

[25] L. Couch, “Intersymbol Interference,” *Digital and Analog Communication Systems*, 2013. [Online]. Available: http://www.princeton.edu/~achaney/tmve/wiki100k/docs/Intersymbol_interference.html.

[26] I. F. Akyildiz, D. Pompili, and T. Melodia, “Challenges for efficient communication in underwater acoustic sensor networks,” *ACM SIGBED Rev.*, vol. 1, no. 2, pp. 3–8, 2004.

[27] L. Lanbo, Z. Shengli, and C. Jun‐Hong, “Prospects and problems of wireless communication for underwater sensor networks,” *Wirel. Commun. …*, pp. 1–24, 2008.

[28] Y. Tsuchida, N. Hama, and M. Takahata, “An optical telemetry system for underwater recording of electromyogram and neuronal activity from non-tethered crayfish,” *J. Neurosci. Methods*, vol. 137, no. 1, pp. 103–109, 2004.

[29] N. G. Jerlov, *Marine Optics*, vol. 14. 1976.

[30] J. Barrett and J. H. Baxendale, “Photolysis of liquid water,” *Trans. Faraday Soc.*, vol. 56, pp. 37–43, 1960.

[31] S. Arnon, “Underwater optical wireless communication network,” *Opt. Eng.*, vol. 49, no. 1, p. 15001, 2010.

[32] N. Agrawal and A. K. Vyas, “Submarine Optical Communication : A research Review,” vol. 1, pp. 370–374, 2012.

[33] Y. F. Fung, M. Dai, and M. F. Ercan, “Underwater short range free space optical communication for a robotic swarm,” *ICARA 2009 - Proc. 4th Int. Conf. Auton. Robot. Agents*, pp. 529–532, 2009.

[34] J. W. Giles and I. N. Bankman, “Underwater optical communications systems. Part 2: basic design considerations,” *MILCOM 2005 - 2005 IEEE Mil. Commun. Conf.*, vol. 3, pp. 1–6, 2005.

[35] D. McIntosh, Q. Zhou, F. J. Lara, J. Landers, and J. C. Campbell, “Flip-chip bonded GaP photodiodes for detection of 400- to 480-nm fluorescence,” *IEEE Photonics Technol. Lett.*, vol. 23, no. 13, pp. 878–880, 2011.

[36] H. Melchior, A. R. Hartman, D. P. Schinke, and T. E. Seidel, “Planar epitaxial silicon avalanche photodiode,” *bell Syst. Tech. J.*, vol. 57, no. 6, pp. 1791–1807, 1978.

[37] Y.-G. Zhang *et al.*, “GaInP–AlInP–GaAs Blue Photovoltaic Detectors With Narrow Response Wavelength Width,” *IEEE Photonics Technol. Lett.*, vol. 22, no. 12, pp. 944–946, 2010.

[38] J. S. Cheong, J. S. L. Ong, J. S. Ng, A. B. Krysa, and J. P. R. David, “$Al_{0.52}In_{0.48}P$ SAM-APD as a Blue-Green Detector.,” *IEEE J. Sel. Top. Quantum Electron.*, vol. 20, no. 6, pp. 142–146, 2014.

[39] J. S. L. Ong, J. S. Ng, A. B. Krysa, and J. P. R. David, “Impact ionization coefficients in $Al_{0.52}In_{0.48}P$,” *IEEE Electron Device Lett.*, vol. 32, no. 11, pp. 1528–1530, 2011.

[40] K. F. Li *et al.*, “Avalanche multiplication noise characteristics in thin GaAs PIN diodes,” *Electron Devices, IEEE Trans.*, vol. 45, no. 10, pp. 2102–2107, 1998.

[41] D. S. Ong, K. F. Li, S. a Plimmer, G. J. Rees, J. P. R. David, and P. N. Robson, “Full band Monte Carlo modeling of impact ionization, avalanche multiplication, and noise in submicron GaAs p(+)-i-n(+) diodes,” *J. Appl. Phys.*, vol. 87, no. 11, pp. 7885–7891, 2000.

[42] C. Hu, K. a. Anselm, B. G. Streetman, and J. C. Campbell, “Noise characteristics of thin multiplication region GaAs avalanche photodiodes,” *Appl. Phys. Lett.*, vol. 69, no. May 2013, p. 3734, 1996.

[43] A. Nikitin and S. Bliven, “Needs of well logging industry in new nuclear detectors,” *IEEE Nucl. Sci. Symp. Conf. Rec.*, pp. 1214–1219, 2010.

[44] R. F. Jurgens, “High-Temperature Electronics Applications Space Exploration,” vol. I, no. 2, pp. 107–111, 1982.

[45] Hamamatsu Photonics, “Multi-Pixel Photon Counters for High Energy Physics Experiments.” [Online]. Available: https://www.hamamatsu.com/sp/hpe/HamamatsuNews/HamaNews_0114.pdf.

[46] S. F. Jackson, S. D. Monk, S. J. Stanley, and K. Lennox, “Sub-aquatic response of a scintillator, fibre optic and silicon photomultiplier based radiation sensor,” *Nucl. Instruments Methods Phys. Res. Sect. A Accel. Spectrometers, Detect. Assoc. Equip.*,

vol. 752, pp. 42–46, 2014.

[47] A. W. Walker, S. Heckelmann, T. Tibbits, D. Lackner, A. W. Bett, and F. Dimroth, "Radiation hardness of AlGaAs n-i-p solar cells with higher bandgap intrinsic region," *Sol. Energy Mater. Sol. Cells*, vol. 168, no. February, pp. 234–240, 2017.

[48] Hamamatsu, "Characteristics and use of Si APD (Avalanche Photodiode)," 2004. [Online]. Available: http://neutron.physics.ucsb.edu/docs/Characteristics_and_use_of_SI_APD.pdf.

[49] X. Guo, A. L. Beck, X. Li, J. C. Campbell, D. Emerson, and J. Sumakeris, "Study of reverse dark current in 4H-SiC avalanche photodiodes," *IEEE J. Quantum Electron.*, vol. 41, no. 4, pp. 562–567, 2005.

[50] D. Zhou *et al.*, "High-temperature single photon detection performance of 4H-SiC avalanche photodiodes," *IEEE Photonics Technol. Lett.*, vol. 26, no. 11, pp. 1136–1138, 2014.

[51] Y. Zhou *et al.*, "Temperature-dependent electrical characteristics of bulk GaN Schottky rectifier," *J. Appl. Phys.*, vol. 101, no. 2, 2007.

[52] S. C. Shen *et al.*, "Performance of deep ultraviolet gan avalanche photodiodes grown by MOCVD," *IEEE Photonics Technol. Lett.*, vol. 19, no. 21, pp. 1744–1746, 2007.

[53] A. P. Kirk, "Proposal for a high voltage AlGaAs/AlGaAs/GaAs triple junction photovoltaic cell," *Sol. Energy Mater. Sol. Cells*, vol. 94, no. 12, pp. 2442–2445, 2010.

[54] J. S. Cheong, A. N. A. P. Baharuddin, J. S. Ng, A. B. Krysa, and J. P. R. David, "Absorption coefficients in AlGaInP lattice-matched to GaAs," *Sol. Energy Mater. Sol. Cells*, vol. 164, no. January, pp. 28–31, 2017.

[55] X. G. Zheng *et al.*, "Temperature Dependence of the Ionization Coefficients of $Al_xGa_{1-x}As$," vol. 36, no. 10, pp. 1168–1173, 2000.

[56] I. Vurgaftman, J. R. Meyer, and L. R. Ram-Mohan, "Band parameters for III-V compound semiconductors and their alloys," *J. Appl. Phys.*, vol. 89, no. 11 I, pp. 5815–5875, 2001.

[57] L. Qiao *et al.*, "Avalanche Noise in $Al_{0.52}In_{0.48}P$ Diodes," *IEEE Photonics Technol.*

Lett., vol. 28, no. 4, pp. 481–484, 2016.

[58] B. K. Ng, "Impact Ionization In Wide Band Gap Semiconductors: $Al_xGa_{1-x}As$ and 4H-SiC," vol. 6, p. 183, 2002.

[59] F. Kocak, A. Kilic, and I. Tapan, "Investigation of Shot Noise in Avalanche Photodiodes," *Acta Phys. Pol. A*, vol. 129, no. 4, pp. 721–723, 2016.

[60] S. Alexander, *Optical Communication Receiver Design*. 1997.

[61] F. Z. Xie, D. Kuhl, E. H. Böttcher, S. Y. Ren, and D. Bimberg, "Wide-band frequency response measurements of photodetectors using low-level photocurrent noise detection," *J. Appl. Phys.*, vol. 73, no. 12, pp. 8641–8646, 1993.

[62] B. Pease, "What's all this transimpedance amplifier stuff, anyhow?"," *Elec- tronic Des.*, vol. 49, p. 139, 2001.

[63] Texas Instrument, "OPA656 Datasheet," 2015. [Online]. Available: http://www.ti.com/lit/ds/symlink/opa656.pdf.

[64] Texas Instruments, "OPA657 Datasheet," 2015. [Online]. Available: http://www.ti.com/lit/ds/symlink/opa657.pdf.

[65] Analog Devices, "AD9631 Datasheet," *Power*, pp. 1–20, 2003.

[66] E. Sackinger, "The transimpedance limit," *IEEE Trans. Circuits Syst. I Regul. Pap.*, vol. 57, no. 8, pp. 1848–1856, 2010.

[67] A. Bhat, "Application note : stabilize your transimpedance amplifier," *Maxim Integr.*, 2012.

[68] R. Paschotta, "Noise in Laser Technology (Part 1)," *Optik & Photonik*, 2009. [Online]. Available: http://doi.wiley.com/10.1002/opph.201190028.

[69] R. Paschotta, "Noise in Laser Technology (Part 3)," *Optik & Photonik*, 2009. [Online]. Available: http://doi.wiley.com/10.1002/opph.201190028.

[70] Thorlab, "HeNe Lasers: Red." [Online]. Available: https://www.thorlabs.com/newgrouppage9.cfm?objectgroup_id=1516.

[71] O. Svelto, *Principles of lasers*. 2010.

[72] Hamamatsu Photonics, “S8664 series datasheet,” pp. 3–5, 2005.

[73] Hamamatsu Photonics, “S2381 series datasheet,” 2005.

[74] “Model 236/237/238 Source Measure Units,” *Quick Reference Guide*. 1990.

[75] C. H. Tan, “Measurements of excess avalanche noise in sub-micron Si and $Al_{0.8}Ga_{0.2}As$ avalanche photodiodes,” *PHD Thesis, Univ. Sheff.*, 2002.

[76] G. ~E. Bulman, “The Experimental Determination of Impact Ionization Coefficients in Gallium-Arsenide and Indium Phosphide.,” *Thesis (PH.D.)--UNIVERSITY OF ILLINOIS AT URBANA -CHAMPAIGN,* 1983.

[77] H. Ando and H. Kanbe, “Ionization coefficient measurement in GaAs by using multiplication noise characteristics,” *Solid State Electron.*, vol. 24, no. 7, pp. 629–634, 1981.

[78] J. E. Green, J. P. R. David, and R. C. Tozer, “A transimpedance amplifier for excess noise measurements of high junction capacitance avalanche photodiodes,” *Meas. Sci. Technol.*, vol. 23, no. 12, p. 125901, 2012.

[79] L. Yin, Q. Chen, S. Kou, and J. Qin, “Research on avalanche photodiode-based photon imaging system,” *2009 Symp. Photonics Optoelectron. SOPO 2009*, 2009.

[80] R. G. Smith and S. D. Personick, “Receiver Design for Optical Fiber Systems,” *Proc. IEEE*, vol. 65, no. 12, pp. 1670–1678, 1977.

[81] C. E. Talley, G. A. Cooksey, and R. C. Dunn, “High resolution fluorescence imaging with cantilevered near-field fiber optic probes,” *Appl. Phys. Lett.*, vol. 69, no. 25, pp. 3809–3811, 1996.

[82] S. Wang *et al.*, “Low-noise impact-ionization-engineered avalanche photodiodes grown on InP substrates,” *IEEE Photonics Technol. Lett.*, vol. 14, no. 12, pp. 1722–1724, 2002.

[83] X. Li, X. Zheng, S. Wang, F. Ma, and J. C. Campbell, “Calculation of gain and noise with dead space for GaAs and $Al_{(x)}Ga_{(1-x)}As$ avalanche photodiode,” *IEEE Trans. Electron Devices*, vol. 49, no. 7, pp. 1112–1117, 2002.

[84] M. E. Woodson, M. Ren, S. J. Maddox, Y. Chen, S. R. Bank, and J. C. Campbell,

"Low-noise AlInAsSb avalanche photodiode," *Appl. Phys. Lett.*, vol. 108, no. 8, 2016.

[85] T. Deliyannis, "High-Q factor circuit with reduced sensitivity," *Electron. Lett.*, vol. 4, pp. 577–579, 1968.

[86] R. H. Hamstra and P. Wendland, "Noise and frequency response of silicon photodiode operational amplifier combination.," *Appl. Opt.*, vol. 11, no. 7, pp. 1539–47, 1972.

[87] F. N. Hooge, "1/F Noise Sources," *IEEE Trans. Electron Devices*, vol. 41, no. 11, pp. 1926–1935, 1994.

[88] J. A. Ringo and P. O. Lauritzen, "1/f noise in uniform avalanche diodes," *Solid State Electron.*, vol. 16, pp. 327–328, 1973.

[89] X. Zhao, M. J. Deen, and L. E. Tarof, "Low frequency noise in separate absorption, grading, charge and multiplication (SAGCM) avalanche photodiodes," *Electron. Lett.*, vol. 32, no. 3, pp. 250–252, 1996.

[90] Texas Instruments, "OPA604 Datasheet." [Online]. Available: http://www.ti.com.cn/cn/lit/ds/symlink/opa604.pdf.

[91] Maxim, "Max4100 Datesheet." [Online]. Available: https://datasheets.maximintegrated.com/en/ds/MAX4100-MAX4101.pdf.

[92] S. Ong, "Impact Ionisation in AlInP Photodiodes," no. November, 2012.

[93] K. A. Bertness, S. R. Kurtz, S. E. Asher, and R. C. Reedy Jr., "AlInP benchmarks for growth of AlGaInP compounds by organometallic vapor-phase epitaxy," *J. Cryst. Growth*, vol. 196, no. 1, pp. 13–22, 1999.

[94] Thorlabs, "LED with Ball Lens, 430 nm," 2016. [Online]. Available: https://www.thorlabs.com/drawings/ccb9ec68457c3e95-A68127EE-F2C7-8A89-9D978193CBDB9FB7/LED430L-SpecSheet.pdf.

[95] Thorlabs, "LED470L Datasheet," 2011. [Online]. Available: https://www.thorlabs.com/drawings/ccb9ec68457c3e95-A68127EE-F2C7-8A89-9D978193CBDB9FB7/LED470L-SpecSheet.pdf.

[96] Thorlabs, "MCPCB-Mounted LED, 505 nm," 2015. [Online]. Available: https://www.thorlabs.com/drawings/ccb9ec68457c3e95-A68127EE-F2C7-8A89-

9D978193CBDB9FB7/M505D2-SpecSheet.pdf.

[97] Thorlabs, “LED with Ball Lens, 525 nm,” 2016. [Online]. Available: https://www.thorlabs.com/drawings/ccb9ec68457c3e95-A68127EE-F2C7-8A89-9D978193CBDB9FB7/LED525L-SpecSheet.pdf.

[98] Thorlabs, “MCPCB-Mounted LED, 530 nm,” 2015. [Online]. Available: https://www.thorlabs.com/drawings/ccb9ec68457c3e95-A68127EE-F2C7-8A89-9D978193CBDB9FB7/M530D2-SpecSheet.pdf.

[99] Thorlabs, “MCPCB-Mounted LED, 590 nm,” 2015. [Online]. Available: https://www.thorlabs.com/drawings/ccb9ec68457c3e95-A68127EE-F2C7-8A89-9D978193CBDB9FB7/M590D2-SpecSheet.pdf.

[100] D. S. Ong, K. F. Li, G. J. Rees, J. P. R. David, and P. N. Robson, “A simple model to determine multiplication and noise in avalanche photodiodes,” *J. Appl. Phys.*, vol. 83, no. 6, pp. 3426–3428, 1998.

[101] J. S. Cheong, J. S. Ng, A. B. Krysa, J. S. L. Ong, and J. P. R. David, “Determination of absorption coefficients in AlInP lattice matched to GaAs,” *J. Phys. D. Appl. Phys.*, vol. 48, no. 40, p. 405101, 2015.

[102] A. L. Beck, B. Yang, X. Guo, and J. C. Campbell, “Edge Breakdown in 4H-SiC Avalanche Photodiodes,” *IEEE J. Quantum Electron.*, vol. 40, no. 3, pp. 321–324, 2004.

[103] M. M. Hayat, B. E. a. Saleh, and M. C. Teich, “Effect of dead space on gain and noise of double-carrier-multiplication avalanche photodiodes,” *IEEE Trans. Electron Devices*, vol. 39, no. 3, pp. 546–552, 1992.

[104] D. A. Ramirez, M. M. Hayat, A. S. Huntington, and G. M. Williams, “Non-local model for the spatial distribution of impact ionization events in avalanche photodiodes,” *IEEE Photonics Technol. Lett.*, vol. 26, no. 1, pp. 25–28, 2014.

[105] J. S. L. Ong and and J. P. R. D. , Jo S. Ng, Andrey B. Krysa, “Temperature dependence of avalanche multiplication and breakdown voltage in $Al_{0.52}In_{0.48}P$, ,” *J. Appl. Phys.*, vol. 64507, pp. 0–6, 2014.

[106] H.Knobe, “Temperture Dependence of Multplicaton Noise in Silicon Avalanche

Photodiodes," *Electron. Lett.*, pp. 539–541, 1978.

[107] J. Yu, L. E. Tarof, R. Bruce, D. G. Knight, K. Visvanatha, and T. Baird, "Noise performance of separate absorption, grading, charge and multiplication InP/InGaAs avalanche photodiodes," *IEEE Photonics Technol. Lett.*, vol. 6, pp. 632–634, 1994.

[108] Y. G. Xiao and M. J. Deen, "Temperature dependent studies of InP/InGaAs avalanche photodiodes\nbased on time domain modeling," *IEEE Trans. Electron Devices*, vol. 48, no. 4, pp. 661–670, 2001.

[109] J. S. L. Ong, J. S. Ng, A. B. Krysa, and J. P. R. David, "Impact ionization in $Al_{0.52}In_{0.48}P$ photodiodes," *PhD Thesis.*, 2012.

Appendix

Appendix A: Electric Field Profile Modelling

This section derives the expressions used to model the electric field profile of the device. The doping in the p^+, p^-, p, p^- and n region are N_1, N_2, N_3, N_4 and N_5, respectively. w_1, w_2, w_3, w_4 and w_5 are the thickness of each region and x_1, x_2, x_3, x_4 and x_5 are the thickness of the depletion region. Electric field at E_1, E_2, E_3 and E_4 are given by,

$$E_1 = \frac{qN_1x_1}{\varepsilon_1} \qquad E_2 = E_1 + \frac{qN_2x_2}{\varepsilon_2} \tag{A.1}$$

$$E_3 = E_2 + \frac{qN_3x_3}{\varepsilon_3} \qquad E_4 = E_3 + \frac{qN_4x_4}{\varepsilon_4} = -\frac{qN_5x_5}{\varepsilon_5}$$

where $\mathcal{E}_1$, $\mathcal{E}_2$, $\mathcal{E}_3$, $\mathcal{E}_4$ and $\mathcal{E}_5$ show the dielectric constant in the each region and q is the electron charge. Equation (A.1) can be rearranged

$$x_5 = \frac{-\varepsilon_5}{N_5}\left(\frac{N_1x_1}{\varepsilon_1} + \frac{N_2x_2}{\varepsilon_2} + \frac{N_3x_3}{\varepsilon_3} + \frac{N_4x_4}{\varepsilon_4}\right) \tag{A.2}$$

The area under electric field is corresponding to the total voltage, V_T across the diode. It is

$$V_T = \frac{1}{2}\left(x_1E_1 + x_2(E_1+E_2) + x_3(E_2+E_3) + x_4(E_3+E_4) + x_5E_4\right) \tag{A.3}$$

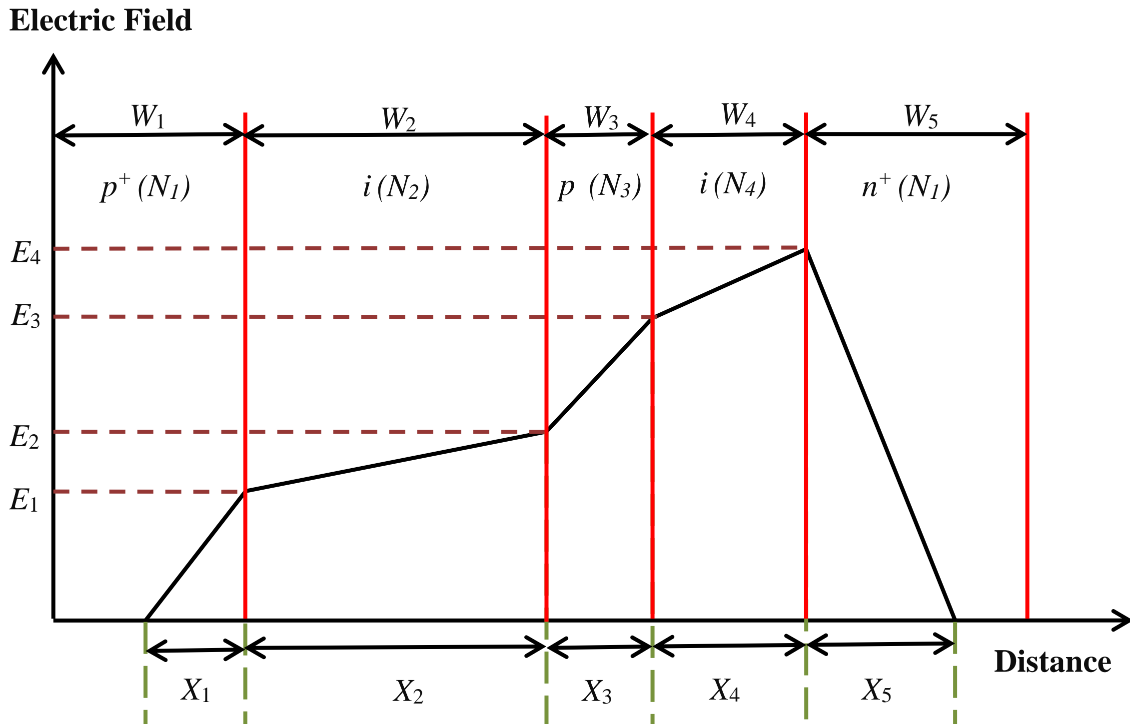

Figure A.1: Electric field profile in the p⁺p⁻p p⁻n structure diode.

Substitute (A.1), (A.2) and (A.3), it gives

$$V_T = \frac{1}{2}\left(\begin{array}{l} x_1 \frac{qN_1x_1}{\varepsilon_1} + x_2\left(\frac{2qN_1x_1}{\varepsilon_1} + \frac{qN_2x_2}{\varepsilon_2}\right) + x_3\left(\frac{2qN_1x_1}{\varepsilon_1} + \frac{2qN_2x_2}{\varepsilon_2} + \frac{qN_3x_3}{\varepsilon_3}\right) \\ + x_4\left(\frac{2qN_1x_1}{\varepsilon_1} + \frac{2qN_2x_2}{\varepsilon_2} + \frac{2qN_3x_3}{\varepsilon_3} + \frac{qN_4x_4}{\varepsilon_4}\right) + \\ \frac{-\varepsilon_5}{N_5}\left(\frac{N_1x_1}{\varepsilon_1} + \frac{N_2x_2}{\varepsilon_2} + \frac{N_3x_3}{\varepsilon_3} + \frac{N_4x_4}{\varepsilon_4}\right)\left(\frac{qN_1x_1}{\varepsilon_1} + \frac{qN_2x_2}{\varepsilon_2} + \frac{qN_3x_3}{\varepsilon_3} + \frac{qN_4x_4}{\varepsilon_4}\right) \end{array} \right) \quad (A.4)$$

Equation (A.4) can be simplify to $ax_1^2+bx_1+c = 0$, the expression for a, b and c is given by,

$$a = \frac{N_1}{\varepsilon_1}\left[1 + \frac{-\varepsilon_5}{N_5}\left(\frac{N_1}{\varepsilon_1}\right)\right] \quad (A.5)$$

$$b = 2N_1\left[\frac{-\varepsilon_5}{N_5}\left(\frac{N_2x_2}{\varepsilon_1\varepsilon_2} + \frac{N_3x_3}{\varepsilon_1\varepsilon_3} + \frac{N_4x_4}{\varepsilon_1\varepsilon_4}\right) + \frac{x_2}{\varepsilon_1} + \frac{x_3}{\varepsilon_1} + \frac{x_4}{\varepsilon_1}\right] \quad (A.6)$$

$$c = \frac{-\varepsilon_5}{N_5}\left(\begin{array}{l} \frac{N_2^2x_2^2}{\varepsilon_2^2} + \frac{N_3^2x_3^2}{\varepsilon_3^2} + \frac{N_4^2x_4^2}{\varepsilon_4^2} + \frac{2N_2x_2N_4x_4}{\varepsilon_2\varepsilon_4} + \frac{2N_2x_2N_3x_3}{\varepsilon_2\varepsilon_3} \\ + \frac{2N_3x_3N_4x_4}{\varepsilon_3\varepsilon_4} \end{array} \right)$$

$$+\left(\frac{N_2x_2^2}{\varepsilon_2} + \frac{2N_2x_2x_3}{\varepsilon_2} + \frac{N_3x_3^2}{\varepsilon_3}\right) + \frac{2N_2x_2x_4}{\varepsilon_2} + \frac{2N_3x_3x_4}{\varepsilon_3} + \frac{N_4x_4^2}{\varepsilon_4} - \frac{2V_T}{q} \quad (A.7)$$

Since V_T is fully deplete ($x_2=w_2$, $x_3=w_3$ and $x_4=w_4$), x_1 can be computed by

$$x_1 = \frac{-b \pm \sqrt{b^2 - 4ac}}{2a} \quad (A.8)$$

The analysis can be extended to a 4 region structure and it simplifies (A.1) to

$$V_T = \frac{1}{2}\left(\begin{array}{l} x_2 \frac{qN_2x_2}{\varepsilon_2} + x_3\left(\frac{2qN_2x_2}{\varepsilon_2} + \frac{qN_3x_3}{\varepsilon_3}\right) + x_4\left(\frac{2qN_2x_2}{\varepsilon_2} + \frac{2qN_3x_3}{\varepsilon_3} + \frac{qN_4x_4}{\varepsilon_4}\right) \\ + \frac{-\varepsilon_5}{N_5}\left(\frac{N_2x_2}{\varepsilon_2} + \frac{N_3x_3}{\varepsilon_3} + \frac{N_4x_4}{\varepsilon_4}\right)\left(\frac{qN_2x_2}{\varepsilon_2} + \frac{qN_3x_3}{\varepsilon_3} + \frac{qN_4x_4}{\varepsilon_4}\right) \end{array} \right) \quad (A.9)$$

Equation (A.9) can be simplify to $ax_2^2+bx_2+c = 0.$

$$a = \frac{N_2}{\varepsilon_2}\left[1 + \frac{-\varepsilon_5}{N_5}\left(\frac{N_2}{\varepsilon_2}\right)\right] \quad (A.10)$$

$$b = 2N_2\left[\frac{-\varepsilon_5}{N_5}\left(\frac{N_3x_3}{\varepsilon_2\varepsilon_3}+\frac{N_4x_4}{\varepsilon_2\varepsilon_4}\right)+\frac{x_3}{\varepsilon_2}+\frac{x_4}{\varepsilon_2}\right] \quad \text{(A.11)}$$

$$c = \frac{-\varepsilon_5}{N_5}\left(\frac{N_3^2x_3^2}{\varepsilon_3^2}+\frac{N_4^2x_4^2}{\varepsilon_4^2}++\frac{2N_3x_3N_4x_4}{\varepsilon_3\varepsilon_4}\right)+\left(\frac{N_3x_3^2}{\varepsilon_3}+\frac{2N_3x_3x_4}{\varepsilon_3}+\frac{N_4x_4^2}{\varepsilon_4}\right)-\frac{2V_T}{q} \quad \text{(A.12)}$$

Since V_T is fully deplete (x_1=0, x_3=w_3 and x_4=w_4), x_1 can be computed by

$$x_5 = \frac{-\varepsilon_5}{N_5}\left(\frac{N_2x_2}{\varepsilon_2}+\frac{N_3x_3}{\varepsilon_3}+\frac{N_4x_4}{\varepsilon_4}\right) \quad \text{(A.13)}$$

For a 3 region structure such as in a *PIN* if $x_1 = x_2 = 0$ and it simplifies (A.1) to

$$V_T = \frac{1}{2}\left(\begin{array}{l} x_3\left(\frac{qN_3x_3}{\varepsilon_3}\right)+x_4\left(\frac{2qN_3x_3}{\varepsilon_3}+\frac{qN_4x_4}{\varepsilon_4}\right) \\ +\frac{-\varepsilon_5}{N_5}\left(\frac{N_3x_3}{\varepsilon_3}+\frac{N_4x_4}{\varepsilon_4}\right)\left(\frac{qN_3x_3}{\varepsilon_3}+\frac{qN_4x_4}{\varepsilon_4}\right)\end{array}\right) \quad \text{(A.14)}$$

Equation (A.14) can be simplify to $ax_3^2+bx_3+c = 0$.

$$a = \frac{N_3}{\varepsilon_3}\left[1+\frac{-\varepsilon_5}{N_5}\left(\frac{N_3}{\varepsilon_3}\right)\right] \quad \text{(A.15)}$$

$$b = 2N_3\left[\frac{-\varepsilon_5}{N_5}\left(\frac{N_4x_4}{\varepsilon_3\varepsilon_4}\right)+\frac{x_3}{\varepsilon_2}\right] \quad \text{(A.16)}$$

$$c = \frac{-\varepsilon_5}{N_5}\left(\frac{N_4^2x_4^2}{\varepsilon_4^2}\right)+\frac{N_4x_4^2}{\varepsilon_4}-\frac{2V_T}{q} \quad \text{(A.17)}$$

Where x_4 is equal to w_4. So the x_5 can be obtained by,

$$x_5 = \frac{-\varepsilon_5}{N_5}\left(\frac{N_3x_3}{\varepsilon_3}+\frac{N_4x_4}{\varepsilon_4}\right) \quad \text{(A.18)}$$

Appendix B: Derivation of the transimpedance amplifier (TIA) transfer function V_o/I_{ph}

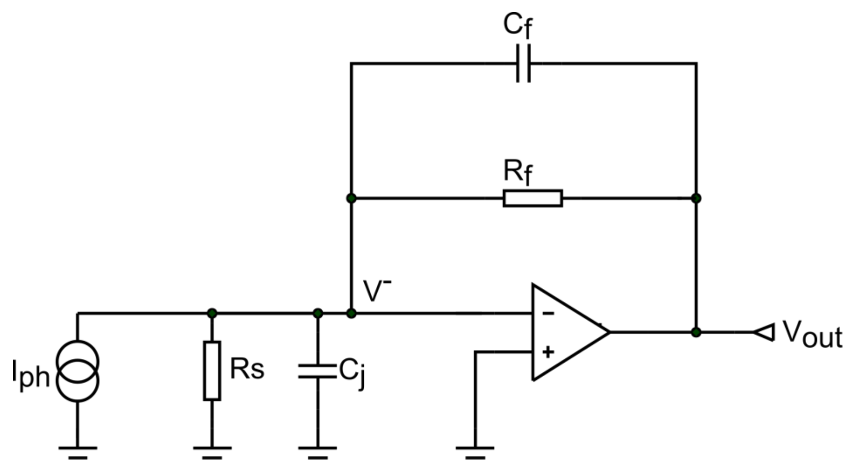

Figure B.1: Transimpedance amplifier circuit.

Summing currents at the v^- node:

$$-\frac{V^-}{R_s}+i_{ph}-\frac{V^- - V_o}{Z_f}=0 \tag{C.1}$$

Where $Z_f = R_f / (1+sR_fC_f)$. v^- could cancel using the op-amp transfer function $V_o = -A_f v^-$,

$$\frac{V_o}{I_{ph}}=-\frac{1}{\frac{1}{Z_sA_f}+\frac{1}{Z_fA_f}+\frac{1}{Z_f}} \tag{C.2}$$

Assume the open loop gain of the op-amp is:

$$A_f=\frac{A_o}{1+s\tau_o} \tag{C.3}$$

Where A_o is the open loop gain and τ_o is the open loop time constant. Substituting (C.3) into (C.1)

$$\frac{V_o}{I_{ph}}=-\frac{1}{\frac{(1+sC_jR_s)(1+s\tau_o)}{A_oR_s}+\frac{(1+sC_fR_f)(1+s\tau_o)}{A_oR_f}+\frac{1+sC_fR_f}{R_f}} \tag{C.4}$$

or

$$\frac{V_o}{I_{ph}}=-\frac{A_oR_sR_f}{(1+s\tau_o)\left[R_f+R_s+s(C_jR_sR_f+C_fR_sR_f)\right]+A_oR_s+sR_sR_fC_fA_o} \tag{C.5}$$

or

$$\frac{V_o}{I_{ph}} = -\frac{A_o R_s R_f}{s^2 \tau_o k + s\left[k + \tau_o R_f + \tau_o R_s + R_s R_f C_f A_o\right] + A_o R_s + R_f + R_s} \quad \text{(C.6)}$$

Where $k = C_j R_s R_f + C_f R_f R_s$

Appendix C: Derivation of the transimpedance amplifier (TIA) output noise voltage

In this section, the noise sources, i_n, v_{nf} and v_n will be discussed individually and the circuit diagram is shown in figure C.1.

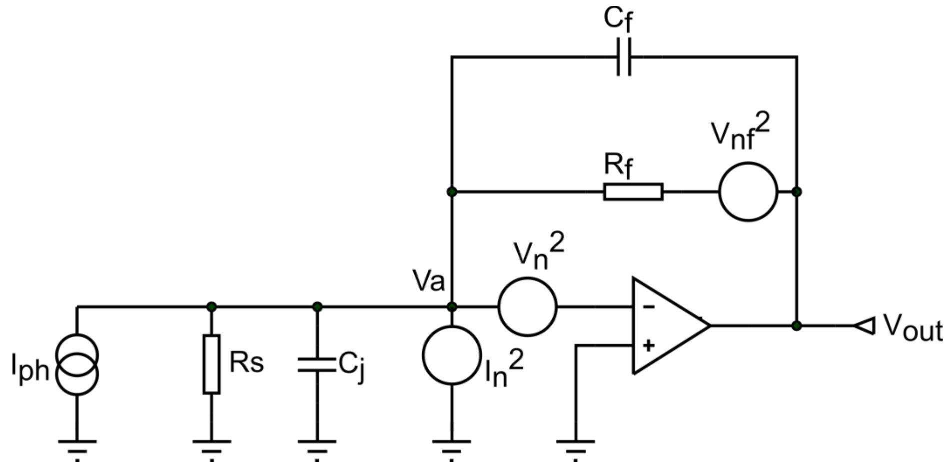

Figure C.1: Noise model of the transimpedance amplifier shows feedback resistance thermal noise voltage, v_{nf} and input op-amp input current (i_n) and input voltage (v_n) noise equivalent source. I_{ph}, R_s and C_j represent the equivlent circuit of the APD.

C1 Input noise voltage transfer function V_o/v_n

This section will only introduce the input voltage noise, v_n. Therefore, the other voltage source will be considered to the short circuit and current sources will be considered to the open circuit.

Summing currents at the v_a node:

$$\frac{v^- - v_n}{Z_s} = \frac{V_o - v^- + v_n}{Z_f} \tag{C.1}$$

Where $Z_s = R_s / (1+sR_sC_j)$ and $Z_f = R_f / (1+sR_fC_f)$. v^- could cancel using the op-amp transfer function $V_o = -A_f v^-$.

$$\frac{-\frac{V_o}{A_f} - v_n}{Z_s} = \frac{V_o + \frac{V_o}{A_f} + v_n}{Z_f} \tag{C.2}$$

or

$$\frac{V_o}{v_n} = -\frac{A_f\left(Z_s + Z_f\right)}{A_f Z_s + Z_s + Z_f} \tag{C.3}$$

or

$$\frac{V_o}{v_n} = -\frac{A_f\left(\frac{R_s}{1+sR_sC_j} + \frac{R_f}{1+sR_fC_f}\right)}{A_f\frac{R_s}{1+sR_sC_j} + \frac{R_s}{1+sR_sC_j} + \frac{R_f}{1+sR_fC_f}} \tag{C.4}$$

or

$$\frac{V_o}{v_n} = -\frac{\frac{A_f\left[R_s\left(1+sR_fC_f\right)+R_f\left(1+sR_sC_j\right)\right]}{\left(1+sR_sC_j\right)\left(1+sR_fC_f\right)}}{\frac{A_fR_s\left(1+sR_fC_f\right)+R_s\left(1+sR_fC_f\right)+R_f\left(1+sR_sC_j\right)}{\left(1+sR_sC_j\right)\left(1+sR_fC_f\right)}} \tag{C.5}$$

or

$$\frac{V_o}{v_n} = -\frac{A_f\left(R_s + sR_sR_fC_f + R_f + sR_sR_fC_j\right)}{sR_sR_f\left(C_fA_f + C_f + C_j\right) + A_fR_s + R_s + R_f} \tag{C.6}$$

Assume the open loop gain of the op-amp is:

$$A_f = \frac{A_o}{1+s\tau_o} \tag{C.7}$$

Where A_o is the open loop gain and τ_o is the open loop time constant. Substituting (C.7) into (C.6)

$$\frac{V_o}{v_n} = -\frac{A_o\left(R_s + R_f\right) + skA_o}{s^2\tau_ok + s\left(k + A_oR_sR_fC_f + \tau_oR_s + \tau_oR_f\right) + A_oR_s + R_s + R_f} \tag{C.8}$$

Where $k = C_jR_sR_f + C_fR_fR_s$

The mean suare output of the noise voltage from the input noise voltage from the op-amp, is given by:

$$\frac{\overline{V_o^2}}{\overline{v_n^2}} = \frac{A_o(r_d + R_f)^2 + \left(\omega kA_o\right)^2}{\left[R_f + R_s\left(1+A_o\right) - \omega^2\tau_ok\right]^2 + \omega^2\left[k + \tau_o\left(R_s + R_f\right) + A_oC_fR_fR_s\right]^2} \tag{C.9}$$

C2 Feedback resistance noise voltage transfer function V_o/v_{nf}

This section will only introduce the feedback resistor voltage noise, v_{nf}. Therefore, the other voltage source will be considered to the short circuit and current sources will be considered to the open circuit.

Summing currents at the v_a node:

$$-\frac{v^-}{Z_s}-\frac{v^- - V_o}{Z_f}-\frac{V_{nf}}{R_f}=0 \tag{C.10}$$

Where $Z_s = R_s / (1+sR_sC_j)$ and $Z_f = R_f / (1+sR_fC_f)$. v^- could cancel using the op-amp transfer function $V_o = -A_f v^-$.

$$\frac{V_o}{V_{nf}}=\frac{1}{R_f\left(\frac{1}{A_fZ_s}+\frac{1}{A_fZ_f}+\frac{1}{Z_f}\right)} \tag{C.11}$$

Assume the open loop gain of the op-amp is:

$$A_f=\frac{A_o}{1+s\tau_o} \tag{C.12}$$

Where A_o is the open loop gain and τ_o is the open loop time constant. Substituting (C.12) into (C.11)

$$\frac{V_o}{V_{nf}}=\frac{1}{R_f\left[\frac{(1+s\tau_o)(1+sR_sC_j)}{A_oR_s}+\frac{(1+s\tau_o)(1+sR_fC_f)}{A_oR_f}+\frac{1+sR_fC_f}{R_f}\right]} \tag{C.13}$$

or

$$\frac{V_o}{V_{nf}}=\frac{A_oR_s}{(1+s\tau_o)(R_f+sR_sC_jR_f+R_s+sR_sR_fC_f)+(1+sR_fC_f)A_oR_s} \tag{C.14}$$

or

$$\frac{V_o}{V_{nf}}=\frac{A_oR_s}{[R_f+R_s(1+A_o)]+s[k+A_oR_sR_fC_f+\tau_o(R_f+R_s)]+s^2\tau_ok} \tag{C.15}$$

Where $k = C_jR_sR_f + C_fR_fR_s$

The mean square of the output noise voltage due to the thermal noise of the feedback resistance is,

$$\frac{\overline{V_o^2}}{\overline{v_{nf}^2}}=\frac{(A_oR_s)^2}{[R_f+R_s(1+A_o)-\omega^2\tau_ok]^2+\omega^2[k+\tau_o(R_s+R_f)+A_oC_fR_fR_s]^2} \tag{C.16}$$

C3 Input noise current transfer function V_o/i_n

As can be seen in Figure C1, the input noise current source, i_n is parallel with the phtocurrent current source, I_{ph}. Therefore, it shows the transfer function V_o/i_n and transfer function V_o/I_{ph} which has been described in Appendix B are same. The mean square of the output noise voltage from the input noise current from the op-amp, is given by:

$$\frac{\overline{V_o^2}}{\overline{i_n^2}} = \frac{\left(A_o R_s R_f\right)^2}{\left[R_f + R_s(1+A_o) - \omega^2 \tau_o k\right]^2 + \omega^2\left[k + \tau_o\left(R_s + R_f\right) + A_o C_f R_f R_s\right]^2} \tag{C.17}$$

C4 Total Output noise voltage transfer function

The total noise voltage at the output from the input noise current, I_n ,the input voltage noise, V_n and feedback thermal noise, V_{nf} is the sum of equation (C9), (C16) and (C17). It is

$$\begin{aligned}\overline{V_o^2} = \overline{v_n^2}\,&\frac{A_o(r_d + R_f)^2 + (\omega k A_o)^2}{\left[R_f + R_s(1+A_o) - \omega^2 \tau_o k\right]^2 + \omega^2\left[k + \tau_o\left(R_s + R_f\right) + A_o C_f R_f R_s\right]^2} \\ + \overline{v_{nf}^2}\,&\frac{\left(A_o R_s\right)^2}{\left[R_f + R_s(1+A_o) - \omega^2 \tau_o k\right]^2 + \omega^2\left[k + \tau_o\left(R_s + R_f\right) + A_o C_f R_f R_s\right]^2} \\ + \overline{i_n^2}\,&\frac{\left(A_o R_s R_f\right)^2}{\left[R_f + R_s(1+A_o) - \omega^2 \tau_o k\right]^2 + \omega^2\left[k + \tau_o\left(R_s + R_f\right) + A_o C_f R_f R_s\right]^2}\end{aligned} \tag{C.18}$$

or

$$\overline{V_o^2} == \frac{\overline{v_n^2}\left[A_o(r_d + R_f)^2 + (\omega k A_o)^2\right] + \overline{v_{nf}^2}\left(A_o R_s\right)^2 + \overline{i_n^2}\left(A_o R_s R_f\right)^2}{\left[R_f + R_s(1+A_o) - \omega^2 \tau_o k\right]^2 + \omega^2\left[k + \tau_o\left(R_s + R_f\right) + A_o C_f R_f R_s\right]^2} \tag{C.19}$$

Appendix D: Extended Random Path Length(RPL) Model

The PDF of the ionization path length of a carrier which start from x_0 in the non-uniform electric field is [ref]

$$\mathrm{h(x)} = \begin{cases} 0, & \mathrm{x \leq d} \\ \alpha^* exp\left[-\int_{x_0}^{x} \alpha^*(x') \, dx'\right], & \mathrm{x > d} \end{cases} \tag{D.1}$$

Where α^* is the position dependent ionization coefficient of the carrier. The probability that the carrier has not ionized by x can be written as:

$$\mathrm{P(x)} = 1 - \int_{x_0}^{x} h(z) dz$$
$$\mathrm{P(x)} = 1 - \int_{x_0}^{x} \alpha^*(z) exp\left[-\int_{x_0}^{x} \alpha^*(x') \, dx'\right] dz \tag{D.2}$$
$$\mathrm{P(x)} = exp\left[-\int_{x_0}^{x} \alpha^*(x') \, dx'\right]$$

A randon ionization path lengrh can be determined by equating P(x) to a random number, r, such that

$$\mathrm{P(x) = r}$$
$$exp\left[-\int_{x_0}^{x} \alpha^*(x') \, dx'\right] = r \tag{D.3}$$
$$\int_{x_0}^{x} \alpha^*(x') \, dx' = -In(r)$$

Equation (D.3) can be discretized in order to get

$$\sum_{x_0}^{x} \alpha^*(x') \, \Delta x' = -In(r) \tag{D.3}$$

Where $\Delta x'$ is the spatial resolution of the electric field mesh.